UNIVERSIDAD DE CHILE
FACULTAD DE CIENCIAS FÍSICAS Y MATEMÁTICAS
DEPARTAMENTO DE ASTRONOMÍA

STUDYING THE ROLE OF GALACTIC ROTATION ON STAR FORMATION: NUMERICAL EXPERIMENTS

TESIS PARA OPTAR AL GRADO DE
MAGÍSTER EN CIENCIAS, MENCIÓN ASTRONOMÍA

JOSÉ UTRERAS CONTRERAS

PROFESOR GUÍA:
DR .ANDRÉS ESCALA ASTORQUIZA

MIEMBROS DE LA COMISIÓN:
DRA. PATRICIA TISSERA MARENGO
DR. GUILLERMO BLANC MENDIBERRI
DR. CÉSAR FUENTES GONZÁLEZ

SANTIAGO DE CHILE
2016

Resumen

Estudiamos la formación estelar y el rol de la rotación a escalas galácticas mediante simulaciones numéricas, utilizando el código de grillas adaptativas Enzo. Parte de este trabajo se centra en estudiar tres leyes de formación estelar encontradas en la literatura: las leyes de Kennicutt-Schmidt y Silk-Elmegreen, y la ecuación dimensionalmente homogénea propuesta por Escala (2015), las que relacionan la formación estelar proyectada con propiedades galácticas. Durante la última década, estudios con un mayor número de observaciones y mayor resolución espacial han puesto en duda que tan fidedignas son las leyes de Kennicutt-Schmidt y Silk-Elmegreen. Para la primera, estudios sugieren la existencia de dos regímenes formación estelar con diferente amplitud y otros proponen un único régimen modificando la forma funcional de la ley de Kennicutt-Schmidt original. Para la ley de Silk-Elmegreen grandes modificaciones no han sido requeridas, sin embargo estudios recientes del momento angular en galaxias han mostrado comportamientos contrarios a esta ley. Estos problemas han motivado el estudio del origen físico de estas relaciones y sus formulaciones matemáticas. Entre estos, Escala (2015) encuentra una función que es capaz de explicar varios observables (de observaciones y simulaciones), dependiendo de los procesos físicos que dominan la dinámica galáctica. En este trabajo estudiamos como las galaxias evolucionan comparándolas con estas leyes, mediante cambios en parámetros físicos, específicamente la rotación galáctica.

Realizamos simulaciones de galaxias espirales y discos nucleares de galaxias de formación violenta, constituidas por gas, estrellas y materia oscura. Durante la evolución de estas galaxias el gas puede enfriarse, fragmentarse y formar estrellas que interactúan con el medio interestelar mediante explosiones de supernova. Como condiciones iniciales, mantenemos fija la masa en gas y su distribución radial para cada tipo de galaxia mientras el perfil de rotación es variado. Esto nos permite aislar medianamente el efecto producido por la rotación en la evolución de las galaxias. Los parámetros deformación estelar son elegidos para obtener la bimodalidad observada en la ley de Kennicutt-Schmidt. La naturaleza bi-dimensional de esta ley nos motiva a estudiar las leyes mencionadas desde distintas líneas de visión, permitiéndonos probar como estas capturan la naturaleza tridimensional de la formación estelar. Nuestras simulaciones muestran ser bien representadas por las leyes de Kennicutt-Schmidt y Silk-Elmegreen globalmente. Sin embargo, encontramos una anti-correlación entre la eficiencia de formación estelar y la velocidad angular Ω, que no es considerada en estas leyes. Incluyendo los efectos de la inclinación respecto al observador, las simulaciones muestran menores tiempos de consumo de gas en la relación de Kennicutt-Schmidt y tiempos similares en la ley de Silk-Elmegreen, atribuido a efectos geométricos. La ecuación propuesta por Escala (2015) describe la evolución de las simulaciones con menor dispersión que las relaciones anteriores. Bajo esta formulación, diferentes inclinaciones muestran eficiencias similares, debido a que considera la concentración de gas en la línea de visión. Sin embargo, esta relación aún muestra la anti-correlación ya mencionada. Estudiamos esta anti-correlación y encontramos que la eficiencia de formación estelar decrece exponencialmente con la velocidad angular en ambos tipos de galaxia. Requiriendo que la eficiencia sea función de cantidades adimensionales, introducimos el parámetro de tiempo de caída libre inicial $t_{\rm ff}^{\rm ini}$, encontrando que la eficiencia puede ser descrita por una función exponencial decreciente de $\Omega t_{\rm ff}^{\rm ini}$. Este resultado nos entrega una formación estelar que toma en cuenta la concentración de gas en la línea de visión y variaciones en la velocidad angular.

Abstract

We study the star formation process at galactic scales and the role of rotation through numerical simulations using the Adaptive Mesh Refinement code Enzo. Most part of this work is focused on the study of three integrated star formation laws found in the literature: the Kennicutt-Schmidt and Silk-Elmegreen laws, and the dimensionally homogeneous equation proposed by Escala (2015), relations that link the projected star formation rates with galactic properties. Over the last decade, studies with a growing number of observations and reaching smaller physical scales have started to cast doubts on how reliable are the Kennicutt-Schmidt and the Silk-Elmegreen laws. In the case of the former, studies have suggested the existence of two different regimes of star formation obeying the same functional form while other groups propose a unique regime by modifying the original Kennicutt-Schmidt law. In the case of the Silk-Elmegreen law, although it has not shown the need of a major modification, recent works studying the angular momentum of galaxies have shown behaviours which go against this law. This problem has motivated the study of the correct physical origins of the observed relations and their underlying mathematical formulations. Among this studies, Escala (2015) found a relation which is able to explain several observed behaviours (in observations and simulations), depending on the physics dominating the dynamics of galaxies. We try to go further by studying how galaxies behave compared to these relations, through changes on physical parameters, specifically the amount of rotation.

We perform simulations of spiral galaxies, constituted by gas, stars and dark matter, and the nuclear disks of starburst galaxies composed by gas and stars only. During the evolution of these galaxies the gas is allowed to cool, fragment and form stars that interact with the interstellar medium via supernova explosions. For the initial conditions, we fix the gas mass and its radial distribution for each type of galaxy while changing the rotational profiles. This allow us to nearly isolate the effects on the evolution of galactic disks produced by rotation. We set the parameters of star formation in order to obtain the observed bi-modality in the Kennicutt-Schmidt relation. In addition, motivated by the two dimensional nature of the Kennicutt-Schmidt law, we study these relations from different lines of sight, permitting us to test how well they capture the three-dimensional nature of the star formation process. Our simulations show a global agreement with the Kennicutt-Schmidt and Silk-Elmegreen laws. However, we find an anti-correlation between the star formation efficiency and the angular velocity, Ω, which is not accounted by these laws. By introducing the effects of the inclination respect to the line of sight the simulations show a consistent shift toward lower depletion timescales in the Kennicutt-Schmidt relation while keeping nearly constant in the Silk-Elmegreen, attributable to geometrical effects. The equation proposed by Escala (2015) describes the evolution of the simulations with a smaller scatter than the previous relations. Under this prescription, different inclinations show similar observed efficiencies, due to the consideration of the concentration of gas along the line of sight. However, this formulation still shows the anti-correlation previously mentioned. We study this anti-correlation and we find that the efficiency of star formation decreases exponentially with the angular velocity of the disks in both types of galaxies. By requiring the efficiency to be a function of dimensionless quantities only, we introduce the initial free-fall time parameter $t_{\rm ff}^{\rm ini}$ and find that the efficiency can be described as an exponential decaying function of $\Omega t_{\rm ff}^{\rm ini}$ for the entire set of simulations. This finding lead us to a unique star formation law which accounts for the concentration along the line-of-sight of the observer and the variations in angular velocity.

Contents

List of Figures

List of tables

Chapter 1

Introduction

1.1 Star Formation

Stars are one of the main constituents of the Universe. During their lifetimes, stars form heavy elements and enrich galaxies with them. This process is necessary for the formation of more complex structures, such as rocky planets. Additionally, stars interact with their surroundings on galactic scales by irradiating the interstellar medium, losing mass through stellar winds or exploding as supernovae for the most massive and brightest stars. Then, knowing how efficiently stars are formed in galaxies is fundamental to understand the evolution of our universe.

Unfortunately, star formation involves a wide range of spatial and temporal scales. This is combined with a large number of physical processes, which are usually dynamically coupled and in the non-linear regime. Thus, a comprehensive understanding of how stars form has remained elusive to astronomers. The typical picture for star formation consists on dense molecular clouds collapsing due their own gravity, while this collapse is resisted by thermal pressure, turbulence, rotational shear, magnetic fields, among others (e.g. Martin & Kennicutt 2001; Seigar 2005; McKee & Ostriker 2007; Padoan et al. 2014). Recent studies agree that stars are most likely created from molecular clouds on scales of a few parsecs, and that feedback produced by their subsequent explosion as supernovae can impact its surroundings up to scales of a few kiloparsecs (Ceverino & Klypin 2009). The influence that stellar feedback has on galactic scales naturally leads to the assumption that star formation might be somewhat related to galactic properties. This large space of parameters has required the formulation of recipes for smaller-scale physics (e.g. at the scales of molecular clouds) when simulating the formation and evolution of galaxies at cosmological scales, due to limited computational power. Usually, these prescriptions are based on empirical relations which relate star formation with galactic properties, what we call star formation laws. In the following subsections we revisit the literature about these star formation laws and what more recent works, which have studied the birth of stars with higher resolutions, tell us about these laws.

1.1.1 The Kennicutt-Schmidt and Silk-Elmegreen laws

One of the first attempts to find a relation between the rate of star formation and galactic properties was performed by Schmidt (1959), who suggested a power-law relation between the star formation rate (SFR) and the density of interstellar gas, usually expressed as

$$\rho_{\rm SFR} \propto \rho_{\rm gas}^{n} \tag{1.1}$$

where $\rho_{\rm SFR}$ is the volumetric density of SFR and n ranges between 1 and 3 according to observations of the Milky Way. In the case of external galaxies the observables correspond to the projected surface densities of gas ($\Sigma_{\rm gas}$) and SFR ($\Sigma_{\rm SFR}$), and the relation reads

$$\Sigma_{\rm SFR} \propto \Sigma_{\rm gas}^{N} \tag{1.2}$$

For disks of constant thickness $N \simeq n$. In order to test this relation over a wide range of surface densities, Kennicutt (1998) performed observations of H_α, HI and CO for spiral galaxies and used far-infrared and CO measurements for starburst galaxies. Kennicutt (1998) derived total molecular masses from the CO emission, considering a constant conversion factor $X_{\rm CO} = 2.8 \times 10^{20} {\rm cm}^{-2} ({\rm K\ km\ s}^{-1})^{-1}$. However, this conversion is expected to vary with the metal content of the environment (Bolatto et al. 2013) and with the interstellar radiation field (Szucs et al. 2016). With a dynamical range of five orders of magnitude in gas surface density and six over star formation rate per unit area, as seen in the left panel of Figure 1.1, Kennicutt (1998) found the equation

$$\Sigma_{\rm SFR} = (2.5 \pm 0.7) \times 10^{-4} \left(\frac{\Sigma_{\rm gas}}{{\rm M}_\odot {\rm pc}^{-2}} \right)^{1.4 \pm 0.15} {\rm M}_\odot\ {\rm yr}^{-1}\ {\rm kpc}^{-2} \tag{1.3}$$

to be the best fit for this dataset. This power-law with a 1.4 index is known as the Kennicutt-Schmidt law. It is important to highlight that this equation was derived from average values of $\Sigma_{\rm gas}$ and $\Sigma_{\rm SFR}$ over the entire galaxies. From this relation it follows that the gas depletion time $t_{\rm SF} \equiv \Sigma_{\rm gas}/\Sigma_{\rm SFR}$ can be parametrized by $t_{\rm SF} \equiv \Sigma_{\rm gas}/\Sigma_{\rm SFR} \propto \Sigma_{\rm gas}^{-0.4}$. One of the theoretical scenarios explaining this relation consists on self-gravitating perturbations growing at a rate given by their local free-fall times, $t_{\rm ff}$, which are proportional to the inverse square root of the density, $t_{\rm ff} \propto \rho_{\rm gas}^{-0.5}$(Madore 1977, Leroy et al. 2008). Then in a certain volume, the SFR is given by gas collapsing in a free-fall time, leading to the relation

$$\rho_{\rm SFR} \propto \frac{\rho_{\rm gas}}{t_{\rm ff}} \propto \rho_{\rm gas}^{1.5} \tag{1.4}$$

Assuming a constant thickness for galactic disks we obtain the same power-law for the projected surface quantities. Other formulation of the star formation law which involves $\Sigma_{\rm gas}$ and a time-scale was suggested by Silk (1997) and Elmegreen (1997), where this characteristic time-scale is taken to be the dynamical time, in this case the orbital time at the galactic radius, $t_{\rm orb}$, which might be valid for star formation triggered by spiral arms or due to cloud-cloud collisions (Tan 2000). The mathematical formulation of the relation is

$$\Sigma_{\rm SFR} \propto \frac{\Sigma_{\rm gas}}{t_{\rm orb}} \propto \Sigma_{\rm gas} \Omega \tag{1.5}$$

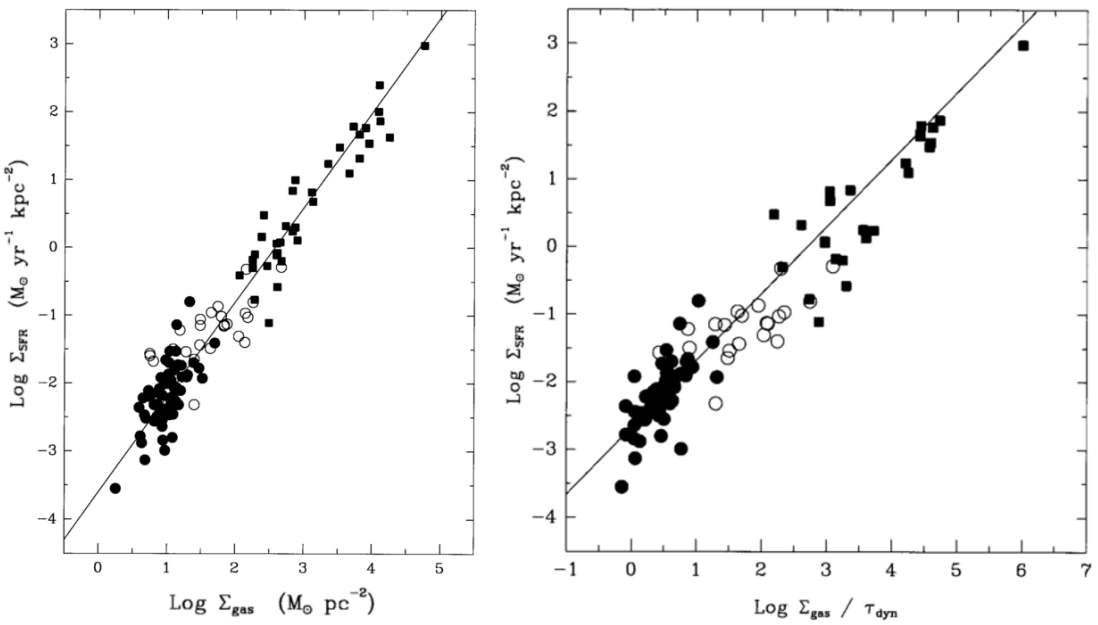

Figure 1.1: Star formation rate relations from Kennicutt (1998). *Left:* Kennicutt-Schmidt relation. *Right:* Silk-Elmegreen Relation.

where Ω is the angular velocity and $\Omega = 2\pi/t_{\rm orb}$. We will refer to this equation as the Silk-Elmegreen law hereafter. Kennicutt (1998) studied this alternative formulation with the same set of galaxies and found that it provided a good of estimation of the projected star formation rates, as shown in the right panel of Figure 1.1. Until this point is not clear whether is $t_{\rm orb}$ or $t_{\rm ff}$ the time-scale related with the rate of star formation due to the similar values of both parameters at galactic scales.

1.1.2 Other formulations

The Kennicutt-Schmidt and Silk-Elmegreen laws are not the only efforts that have been performed in this area. As seen in subsection 1.1.1, assuming that equation (1.4) is the intrinsic star formation law, the projected relation results in

$$\Sigma_{\rm SFR} = \epsilon_{\rm ff} \frac{\Sigma_{\rm gas}}{t_{\rm ff}} \tag{1.6}$$

where several authors have proposed models for the characteristic free-fall time in galaxies. Among these works, Krumholz et al. (2012) proposed analytical approximations for the free-fall time in two different regimes: star formation in giant molecular clouds and gas-rich disks. Applying their formulation to Milky-Way molecular clouds, Local-Group galaxies, and unresolved disks and starburst galaxies they found the SFR to be consistent with equation (1.6). Additionally, they showed that the Silk-Elmegreen law fails predicting the SFRs in Milky-Way molecular clouds and Local-Group galaxies. Both results are shown in Figure 1.2.

Other works have focused in the star formation rates inside molecular clouds, where star formation is thought to be decoupled from galactic properties (Bigiel et al. 2008). Padoan

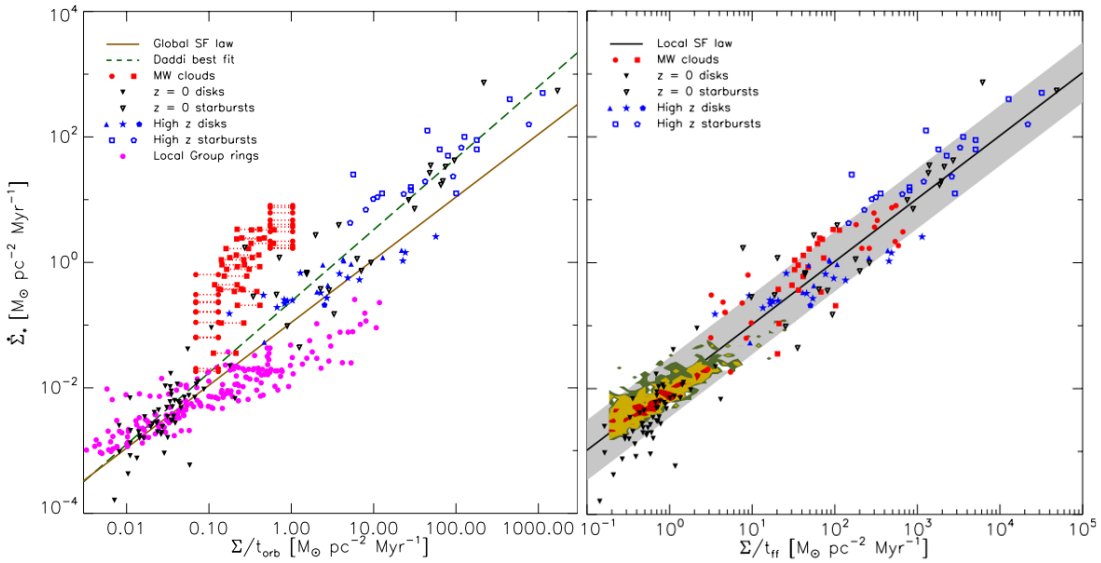

Figure 1.2: Comparison between $t_{\rm orb}$ and $t_{\rm ff}$ as depletion time-scales for the star formation law. *Left:*Silk-Elmegreen law for measurements considered in Krumholz et al. (2012). *Right:* Star formation law proposed by Krumholz et al. (2012) based on $t_{\rm ff}$.

et al. (2012) studied the star formation efficiency, $\epsilon_{\rm ff}$, performing simulations of molecular clouds subject to supersonic MHD turbulence. As shown in the left panel of Figure 1.3, they found that $\epsilon_{\rm ff}$ decreases exponentially with $t_{\rm ff}/t_{\rm dyn}$ as

$$\epsilon_{\rm ff} \propto \exp(-1.6 t_{\rm ff}/t_{\rm dyn}) \tag{1.7}$$

where $t_{\rm ff} = \sqrt{3\pi/32G\rho_0}$ is the mean free-fall time, ρ_0 is the mean density, $t_{\rm dyn} = L/2\sigma_{v,3\rm D}$, L is the size of the simulation box and $\sigma_{v,3\rm D}$ is the 3-dimensional dispersion velocity. The right panel of Figure 1.3 shows in blue the $\Sigma_{\rm SFR}$ obtained in a simulation of a Milky-Way size galaxy performed by Semenov et al. (2015), using the efficiency defined by equation (1.7). They found that the model predicts a wide variation is the star formation efficiency which is consistent with observations, which are shown in the right panel of Figure 1.3 by the orange contour and green diamonds.

In order to build a function able to describe a physical process, it is desirable some knowledge of the parameters involved in the process and how they would be related in an equation beforehand. In the case of the simulations of Padoan et al. (2012) the main processes regulating star formation are turbulence and self-gravity, where their combined effect is parametrized by $t_{\rm ff}/t_{\rm dyn}$. In the case of Krumholz et al. (2012) the main parameter is how fast star-forming clouds collapse due to self-gravity. Additionally, these two prescriptions have something in common: they are dimensionally homogeneous. According to dimensional analysis any physically meaningful equation must be dimensionally homogeneous: only commensurable quantities (quantities with the same dimensions) may be compared, equated, added, or subtracted. Therefore if we want to find a law for $\Sigma_{\rm SFR}$ and its fundamental dimensions (G, $\Sigma_{\rm gas}$, Ω, R, etc.) dimensionally homogeneity needs to be fulfilled.

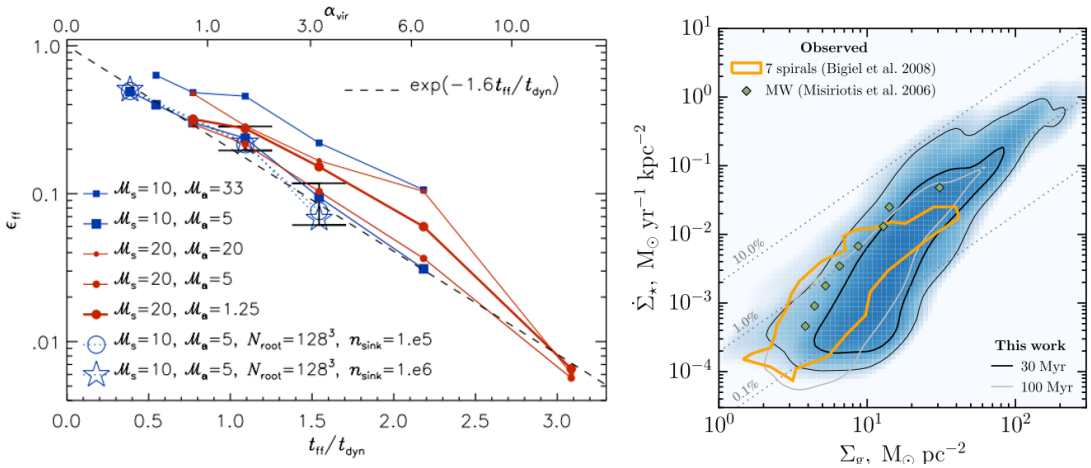

Figure 1.3: Star formation efficiency for molecular clouds. *Left:* Efficiency in simulations of molecular clouds subjected to turbulent forcing, performed by Padoan et al. (2012). *Right:* Simulations of Semenov et al. (2015) applying the star formation efficiency found by Padoan et al. (2012) and comparing with observations.

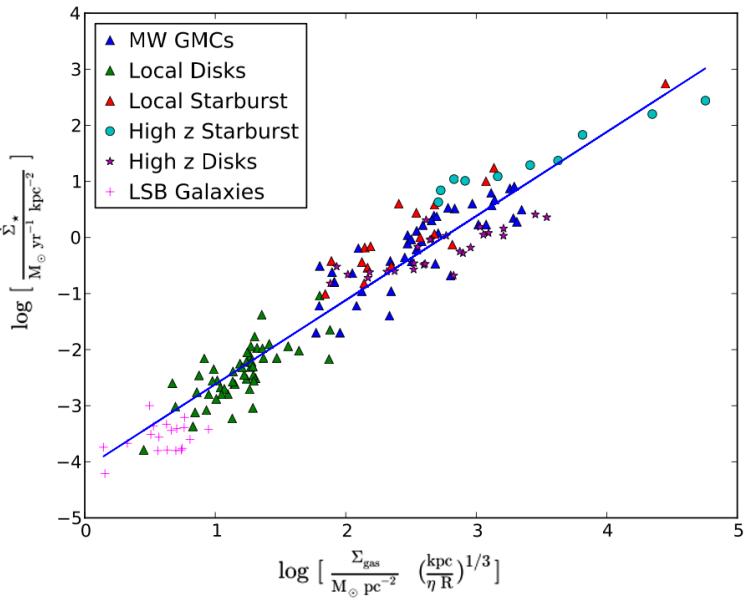

Figure 1.4: Star formation relation proposed by Escala (2015).

An important theorem to find such equations is the Buckingham Π theorem of dimensional analysis which was applied by Escala (2015). Starting from the Kennicutt-Schmidt law and by the effects of self-gravity, Escala (2015) considered the terms $\Sigma_{\rm SFR}$, $\Sigma_{\rm gas}$ and the gravitational constant G. Additionally, Escala (2015) includes a characteristic length L that would take into account different geometries. The combination of $\Sigma_{\rm gas}$, G and L resulted in a unique equation for $\Sigma_{\rm SFR}$, given by

$$\Sigma_{\rm SFR} = \epsilon \sqrt{\frac{G}{L}} \Sigma_{\rm gas}^{3/2} \tag{1.8}$$

Escala (2015) tested two characteristic scales for a disk system; the radial and vertical length scales in cylindrical coordinates, showing that the later results in a unique law that represents the star formation rate for different types of galaxies, shown in Figure 1.4. Furthermore, Escala (2015) showed that depending on the physics involved in the parameter L, such as the characteristic size of the instabilities, equation (1.8) recovers different star formation laws found in the literature, e.g. replacing L by the largest scale not stabilized by rotation (Escala & Larson 2008) derives in the Silk-Elmegreen law. In addition, the efficiency must depend on dimensionless parameters given by the physics at smaller scales, such as turbulence, magnetic fields, thermal pressure among others, which is consistent with the results of Padoan et al. (2012).

1.1.3 Deviations from the Kennicutt-Schmidt and Silk-Elmegreen laws

Although the Kennicutt-Schmidt relation is probably the most studied star formation law, more recent studies of resolved galaxies have started to put the law into doubt. For instance, studying the Kennicutt-Schmidt law at sup-kpc scale for a sample of nearby galaxies, Bigiel et al. 2008 found that in the H_2-dominated centres of these galaxies the star formation rate is linearly related with the surface density of molecular hydrogen instead of atomic hydrogen, i.e. N $\sim$ 1.0. Figure 1.5 shows the $\Sigma_{\rm SFR}$ against the surfaces densities of atomic ($\Sigma_{\rm HI}$), molec-

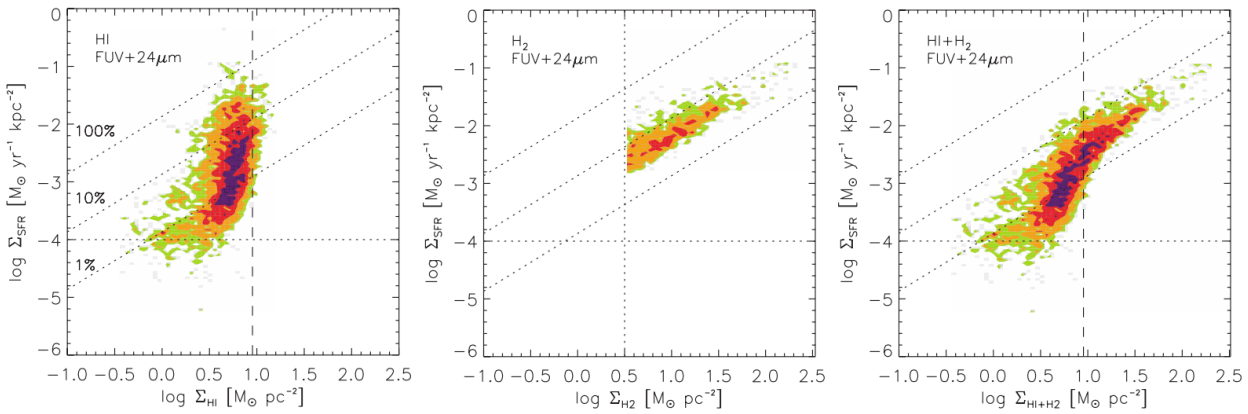

Figure 1.5: Kennicutt-Schmidt relations from Bigiel et al. (2008). *Left:* Atomic hydrogen. *Middle:* Molecular hydrogen. *Right:* Total hydrogen content.

ular ($\Sigma_{\rm H_2}$) and total hydrogen ($\Sigma_{\rm HI+H_2}$) from the work of Biegel et al. (2008). They found that $\Sigma_{\rm HI}$ saturates at a surface density $\sim 9 {\rm M}_\odot {\rm pc}^{-2}$. For higher surface densities, hydrogen is mainly in it molecular form and linearly traces the $\Sigma_{\rm SFR}$. Combining atomic and molecular hydrogen they did not find a clear universal relation. However, by studying the HI dominated regions of spatially resolved nearby galaxies, Roychowdhury et al. (2015) found a power-law relation between $\Sigma_{\rm HI}$ and $\Sigma_{\rm SFR}$ with a slope similar to 1.5. Figure 1.6 shows the best fits, in coloured lines, for the different samples of galaxies used by Roychowdhury et al. (2015) and the brown contour shows the results found by Bigiel et al. (2008).

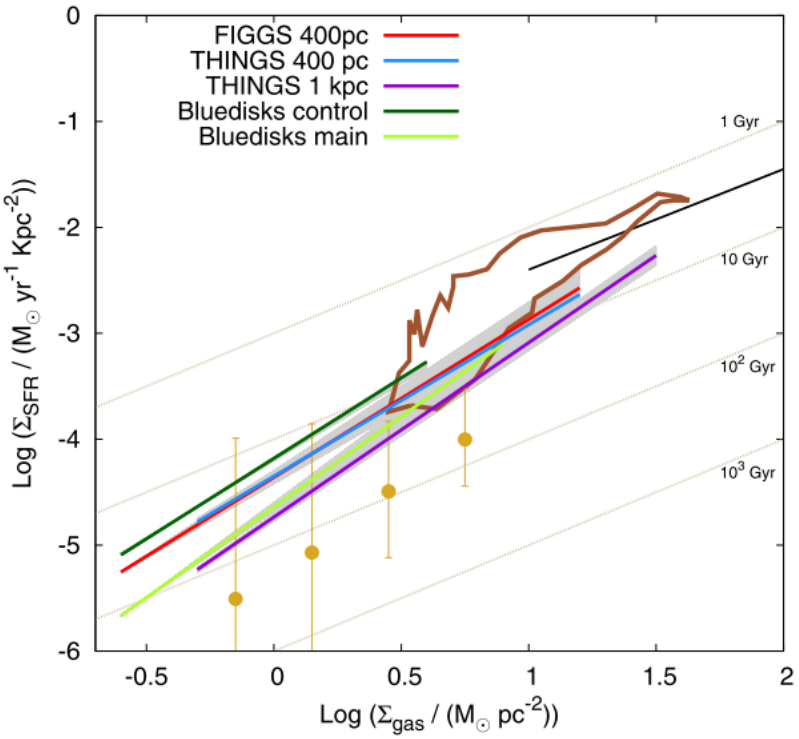

Figure 1.6: Kennicutt-Schmidt relation for HI dominated regions from Roychowdhury et al. (2015).

Although these results might seem contradictory, they are not incompatible. Lada et al. 2010 investigated the star formation activity in nearby molecular clouds and found that above a density threshold $\sim 116 M_{\odot} pc^{-2}$ the SFR grows linearly with the mass of molecular clouds. We can interpret all these results in the following way: when the atomic and more diffuse gas becomes gravitationally unstable it starts to collapse and cool, forming molecular clouds in a free-fall time. After the molecular clouds are formed its evolution is decoupled from galactic properties and starts to form stars at similar time-scales. Different fractions of molecular gas would naturally lead to changes in the slope of the law. Also, under this interpretation, comparing $\Sigma_{\rm HI}$ with $\Sigma_{\rm SFR}$ in regions dominated by molecular hydrogen does not have a clear meaning.

Another issue concerns the uniqueness of the Kennicutt-Schmidt law. Daddi et al. (2010) investigated the consequences of the lower conversion factor $X_{\rm CO}$ shown by luminous infra-red galaxies (LIRGs)(Downes & Solomon 1998), in the star formation law. They showed that normal spiral galaxies appear to create stars from their gas reservoirs over larger time-scales than starburst disks at the same surface density, suggesting the existence of two different regimes for star formation. The left panel of Figure 1.7 shows the sample of galaxies used in this work displaying these two sequences. Interestingly, when studying the Silk-Elmegreen law they do not find two modes of star formation (right panel Figure 1.7), suggesting the existence of a universal star formation law. Although, it is known that LIRGs have lower $X_{\rm CO}$ factors than local spirals, the methodology in this work has been put into question. Daddi et al. (2010) used discrete values of the conversion factor for different types galaxies:

$X_{CO} = 3.6M_{\odot}(\mathrm{K\ km\ s^{-1}pc^2})^{-1}$ for high z normal galaxies, $4.6M_{\odot}(\mathrm{K\ km\ s^{-1}pc^2})^{-1}$ for local spirals and $0.8M_{\odot}(\mathrm{K\ km\ s^{-1}pc^2})^{-1}$ for local LIRGs and distant submillimeter galaxies. Using discrete values for a parameter might produce spurious bi-modalities. Furthermore, using numerical models to study variations in X_{CO}, Narayanan et al. (2013) found that the data was better represented by a single power-law with a slope of ~ 1.95.

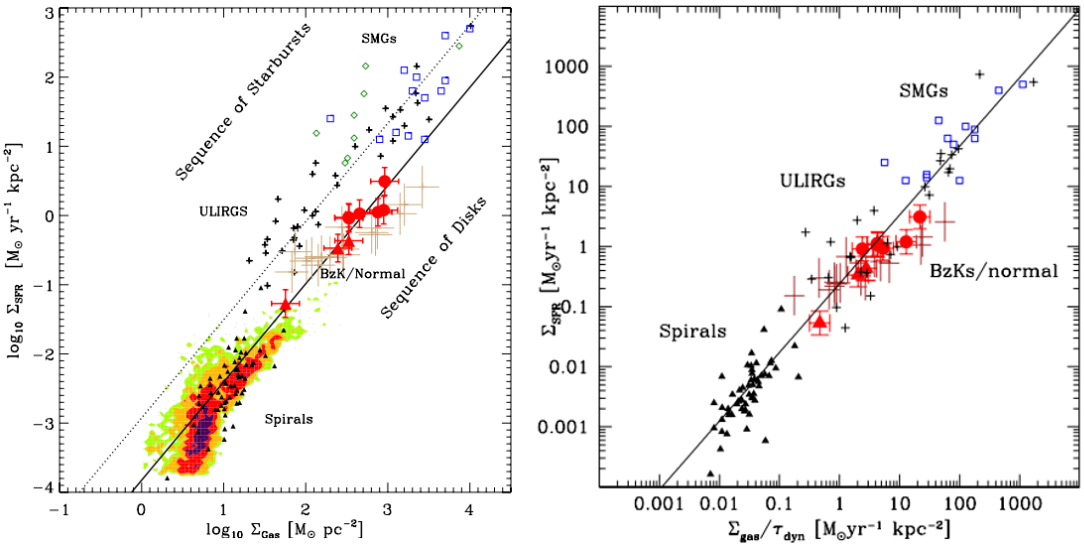

Figure 1.7: Star formation laws from observations in Daddi et al. (2010). *Left:* Kennicutt-Schmidt law showing two different regimes for star formation. *Right:* Silk-Elmegreen law showing a single regime for star formation.

1.1.4 Galactic rotation

Even though the work of Daddi et al. (2010) seems to put the Silk-Elmegreen law in best position, recent works also question the validity of this law. For instance, investigating the star formation efficiency in the early-type galaxies of the ATLAS^{3D} sample, Davis et al. (2014) found that by using local free-fall times instead of t_{orb} (Ω) they obtain a universal relation with less scatter.

Particularly, the role of galactic rotation in the star formation process is not completely understood due to conflicting results. Tan (2000) studied star formation triggered by cloud-cloud collisions in the two-dimensional plane. For this mechanism of star formation, Tan (2000) found that Σ_{SFR} was proportional to $\Sigma_{\mathrm{gas}}\Omega(1-0.7\beta)$, where β parametrizes the shear of disks. Despite that simulations show that cloud-collisions are frequent in disk galaxies (Tasker & Tan 2009), recent hydrodynamics simulations of Dobbs et al. (2015) showed that collisions occur along the minor axis of the clouds, as shown in Figure 1.8, due to their alignment with spiral arms. They also found that collisions produce little or no variation in the structure of clouds. This findings suggest that collisions produce little differences in the total SFRs in galaxies. Berta et al. (2008) found that the spin of dark matter halos is anti-correlated with stellar mass, using 53.000 disk galaxies from the SDSS spectroscopic

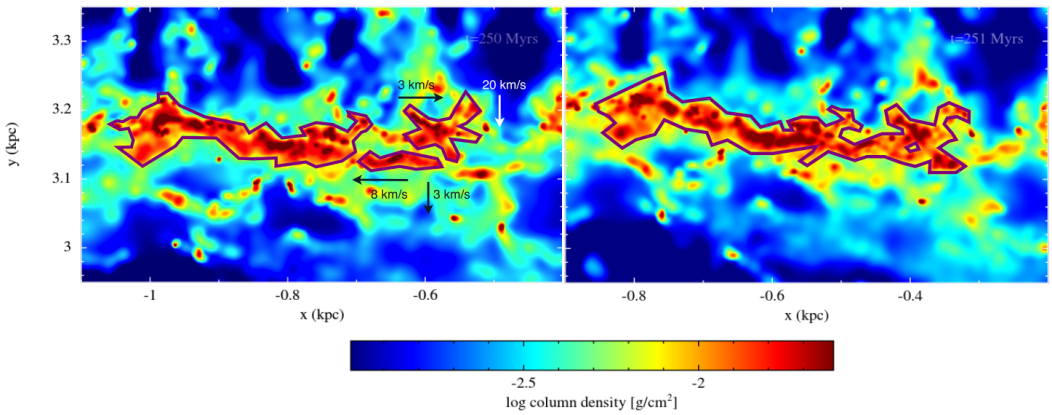

Figure 1.8: Collision of molecular clouds from simulations of Dobbs et al. (2015). The collision occurs along the minor axes of the clouds.

sample. Additionally, they found that galaxies with higher spin present more recent star formation. An interpretation is that SFR is anti-correlated with spin: galaxies with lower spins form stars faster and at earlier times, while galaxies with higher spins form stars over longer time-scales. This is consistent with recent findings of Obreschkow et al. (2015).

The simplest picture which is consistent with star formation laws shown in section 1.1.2 and the findings mentioned here is gravitational instability. In the context of gravitational stability of gaseous disk, the most known criterion is the Toomre parameter (Toomre 1964) for axisymmetric perturbations on razor-thin disks, expressed as

$$Q \equiv \frac{\kappa c_s}{\pi G \Sigma} \tag{1.9}$$

with κ being the epicyclic frequency, c_s the sound speed and Σ the surface density of disks. According to this criterion, instability arises when $Q < 1$. The rotation of galactic disks Ω is related with the epicyclic frequency by

$$\kappa^2 = 4\Omega^2(1 + \frac{1}{2}\frac{d\ln\Omega}{d\ln R}) \tag{1.10}$$

where R is the cylindrical radius. From the extreme cases of Keplerian and rigid body motion it follows that the epicyclic frequency lies between $\Omega \lesssim \kappa \lesssim 2\Omega$.

From equation (1.9) we see that, for a given sound speed and distribution of gas, galactic rotation stabilizes the disk against gravitational collapse. This effect might explain what is seen in observations (Berta et al. 2008, Dobbs et al. 2015, Obreschkow et al. 2015). Then, in the context of a star formation law we also expect to observe the effects of galactic rotation, since it establishes which regions of a galaxy are allowed to collapse and form stars. However, there have not been many studies focused to test this hypothesis.

It is worth mentioning that from the parameters which control the stability of a rotating disk, rotation is the simplest to analyse: turbulence, shocks and stellar feedback produce large variations in the sound speed, while variations on the thickness of disks and the evolution

itself produce variations in the strength of self-gravity, accounted by the term $G\Sigma$. On the other hand, galactic rotation is less affected by such processes since it is more related with the density distribution at larger scales.

1.2 Objectives

In this paper we study the role of galactic rotation on star formation by performing three-dimensional hydrodynamic simulations of spiral and starburts galaxies which allow us to span a wide range of $\Sigma_{\rm gas}$. Part of this work is focused on comparing and testing different star formation laws found in the literature against simulations in order to elucidate their applicability and limitations. We test how these relations behave when the inclination of the galaxies with respect to the line-of-sight is varied.

Our principal aim is to elucidate the role of galactic rotation on global star formation studying disk galaxies with different angular momentum and different sizes which allow us to span a wide range of $\Sigma_{\rm gas}$. Additionally, we investigate the effects of projection on the star formation laws. In this context, numerical simulations are a helpful tool to isolate and characterize the effects of each time-scale and parameter on the star formation problem. Varying one parameter at a time allows us to construct a relation that considers each independent feature and to disentangle the role of coupled variables.

We performed this study using numerical simulations of two spiral disk galaxies and four nuclear disks of starburst galaxies in order to compare with the different regimes found by Daddi et al. (2010). These simulations were carried out using the hydro-code Enzo (Bryan et al. 2014) which uses the Adaptive Mesh Refinement (AMR) technique and includes radiative cooling, star formation and stellar feedback to accurately model the galaxy evolution. The initial parameters are set in order to increase the effects of rotation respect to other physical parameters.

1.3 Thesis structure

This thesis is organized as follows: In section 2 we present the astrophysical code Enzo with its detailed structure and the different algorithms that model radiative cooling, star formation, stellar feedback and N-body dynamics. In section 3 we describe the models and how we choose their characteristic parameters in order to focus our study on galactic rotation and the star formation laws. In section 4 we analyse the evolution of the simulated galaxies, their resulting star formation laws and the observed impact of galactic rotation on the star formation efficiency. Finally, we present our conclusions and outlook in section 5.

Chapter 2

The Code

The growth of structures in the universe, e.g. stars and galaxies, involves large dynamical ranges and several astrophysical processes in the non-linear regime. This has lead to the development of numerical techniques which reach a high accuracy and the needed dynamic ranges in order to compare with observations. In this sense, numerical simulations are the main theoretical tool to study the dynamics of self-gravitating structures. In astrophysics, the most simulations are based on two methods: Smoothed Particle Hydrodynamics (SPH; Lucy 1977; Gingold & Monaghan 1977) which follow the fluid elements (Lagrangian method), or grid-based methods (Eulerian method), which can be either static mesh (Stone & Norman 1992), or use adaptive mesh refinement (AMR; Berger & Colella 1989) methods, that increase the spatial and temporal resolution where needed. Both of these techniques has advantages and disadvantages. In SPH simulations, the resolution is not limited to grid spacing Δx, and its solutions are Galilean invariant. However, SPH simulations present problems modelling turbulence and the evolution of shocks, and tend to suppress fluid instabilities (Agertz et al. 2007, Creasey et al. 2011). Grid-based methods on the other hand represent fluids as a continuum, where their hydrodynamic solvers are based on conservation laws and are able to capture shocks within 1-2 cells. Nevertheless, Grid-based codes are not Galilean invariant and do not accurately integrate the trajectories of point particles.

We focus our study on the fluid dynamics of gas in disk galaxies. This gas is subjected to stellar feedback through supernova explosions which produces shocks and increases the turbulent energy in the system. The appropriate technique for this problem corresponds to grid-based simulations. For this work we use the AMR code ENZO (Bryan et al. 2014)

2.1 ENZO

Enzo is an Eulerian technique based on the structured AMR algorithm developed by Berger and Colella (1989). It was initially developed for cosmological simulations and extended to been used on a wide variety of problems, becoming a general tool for studying astrophysical hydrodynamics. The main algorithms included in the code correspond to a gravity solver, hydrodynamic solvers with different accuracies, an N-body solver for the evolution of stars, black holes and sink particles, and different routines for the thermodynamics in each cell, such as species solver, heating, cooling, star formation and feedback, and radiative transfer.

2.2 AMR

The AMR technique utilizes an adaptive hierarchy of grid patches with different levels of resolution as shown in Figure 2.1. This capability of Enzo allows it to increase the accuracy, and the spatial and temporal resolution in the regions of interest, distributing efficiently the limited computational resources.

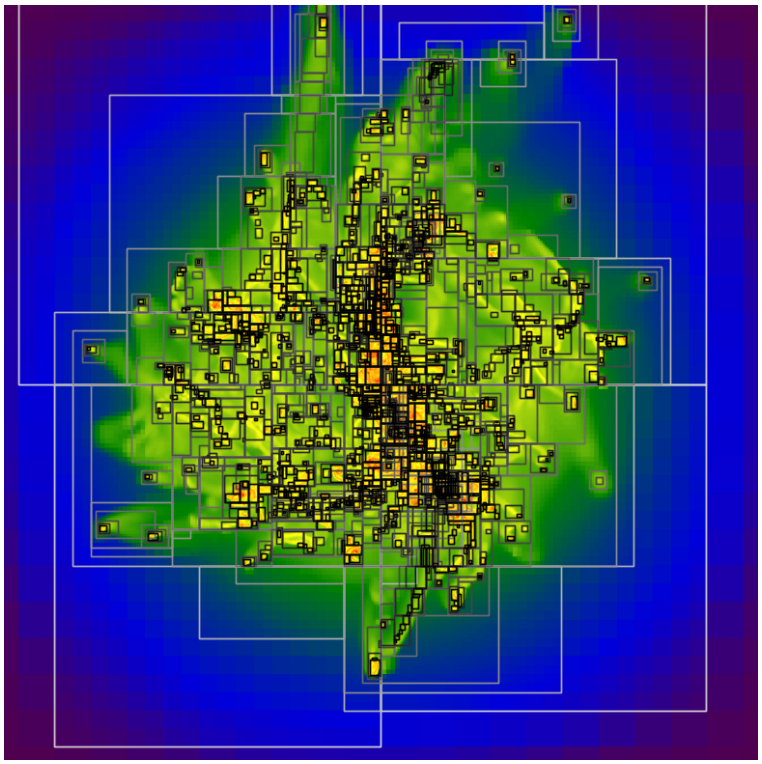

Figure 2.1: Illustration of grids in a simulation.

2.2.1 Grids

The grid hierarchy starts with the root grid, labelled level zero, which covers the entire domain characterized by a uniform Cartesian grid. The root grid is discretized into several rectangular grid patches ("grid") when a higher resolution is required. A level correspond to all the grids with the same cell size (not having necessarily the same parent). The subgrids are restricted to a number of conditions:

i. The ratio r between the cell sizes, or refinement factor, is restricted to be an integer, typically 2 or 4.

ii. Each subgrid must begin and end on the boundary or the parent cell.

iii. Each subgrid must be completely contained by its parent cell.

We adopt $r = 2$ which shows to provide the best performance (Bryan et al. 2014). The structure consist on a hierarchical tree represented in Figure 2.2, where each rectangular grid can itself become the parent grid to an even more highly resolved child grid.

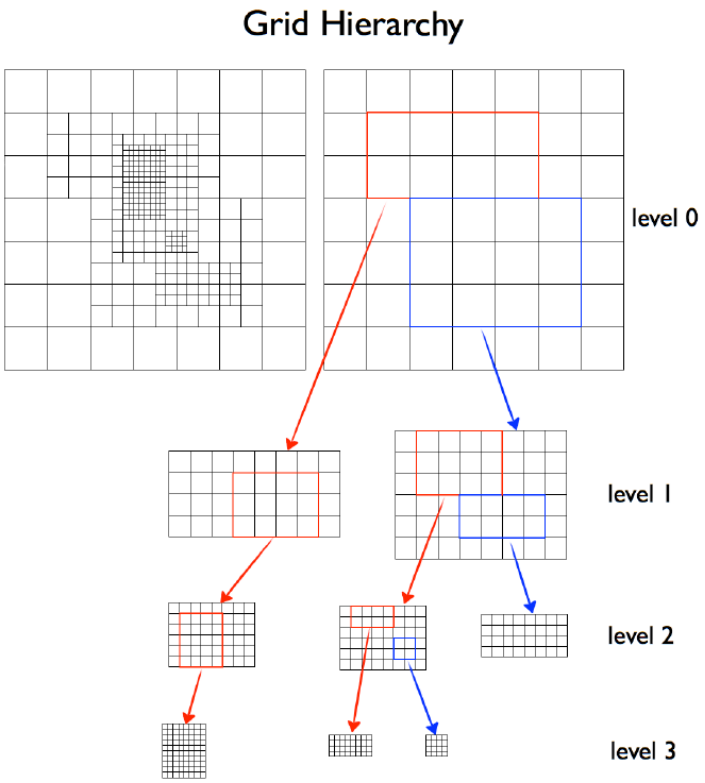

Figure 2.2: Illustration of grid hierarchy

A patch grid is considered as an individual object that contains field variables, such as density, and particle data. These grids are hierarchically organized into a core of active zones and a surrounding ghost zone, as shown in Figure 2.3. The active zones contain the field values while the ghost zones are used to store values obtained from neighbouring grids or from a parent grid. This technique is necessary for the implementation of the hydrodynamic solvers, which need to interpolate values of fluxes at the grid boundaries, and the gravity solver. The hydrodynamic solver used in this work (ZEUS) requires three layers of ghost zones, while the gravity solver requires six.

At some given time t, we advance the solution in a time-step determined on each level. Then time is hierarchically advanced in the manner of a W-cycle in a multigrid solver as shown in Figure 2.4. First, the algorithm determines the maximum time-step allowed for the coarsest level, l, and then all the girds on that level are advanced one time-step. Then in the next level, $l + 1$, all the grids are advance on the maximum allowed time-step on that level. If there are more levels, this procedure is repeated until the finest grids of the hierarchy has been reached. Once there, the grids are advanced until they synch their coarser parent grids, which then take one more time-step. This procedure is repeated until all grids have been advanced by the desire time interval.

This hierarchy must adapt itself since grids with higher resolution may move. After one time-step is taken on a level, each grid must update its ghost zones based on the new information of their neighbouring grids and/or interpolating from their parent grids. Moreover,

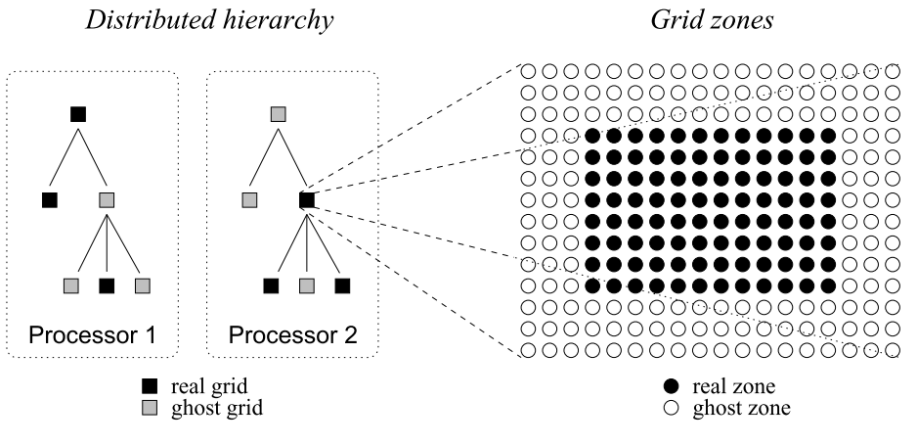

Figure 2.3: Example of a distributed grid hierarchy showing real and ghost grids.

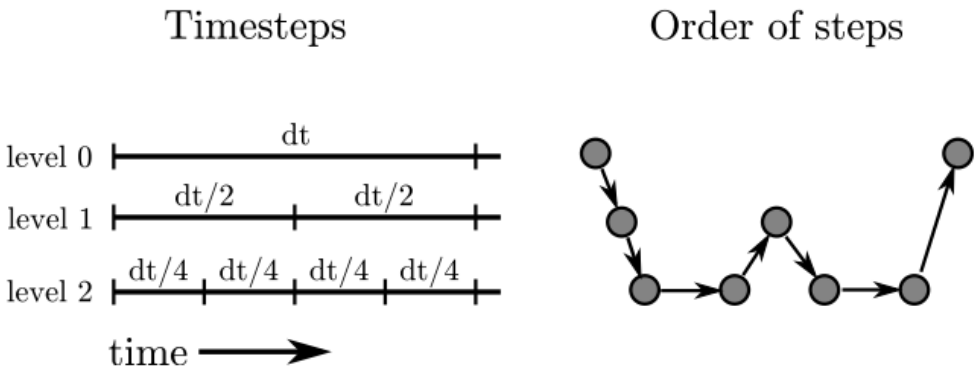

Figure 2.4: Example of the W-cycle in a two-level hierarchy. Enzo does not the timesteps to be a factor 2^n smaller.

each cell is examined to see if further refinement is needed, rebuilding the hierarchy from that level to the finest level. This algorithm is summarized in the pseudo-code shown in Figure 2.5. Beginning from the level 0, each level its advance by its corresponding time-step and the hierarchy is rebuilt.

2.2.2 Boundary values

As shown in Figure 2.5, to solve the hydrodynamic equations for a given level it is mandatory to specify the boundary values for the grids on that level. There are two kinds of boundaries. The first kind corresponds to the boundaries of the computational domain. The second possibility is that the grid boundaries are within the computational domain, being the most common.

For the first kind of boundaries, Enzo allows four types of boundary conditions: (i) reflecting, (ii) outflow, (ii) inflow and (iv) periodic. For the simulations presented here we

```
InitializeHierarchy
While (Time < StopTime):
   dt = ComputeTimeStep(0)
   EvolveLevel(0, dt)
   Time = Time + dt
   CheckForOutput(Time)

EvolveLevel(level):
   SetBoundaryValues
   while (Time < ParentTime):
      dt = ComputeTimeStep(level)
      SolveHydroEquations(dt)
      SolveOtherEquations(dt)
      Time = Time + dt
      SetBoundaryValues
      EvolveLevel(level+1, dt)
      FluxCorrection
      Projection
      RebuildHierarchy(level+1)
```

Figure 2.5: Pseudo-code of the hierarchy construction algorithm.

use periodic boundary conditions. As previously mentioned, for the boundaries within the domain, the boundary values must be interpolated from the parent grids or copied from neighbouring cells wherever possible. The interpolations must be conservative, i.e. the mean value of the interpolated quantity is equal to the cell value. These functions are restricted to be monotonic between the centers of two grids to avoid the introduction of new extrema which would produce spurious fluxes cell interfaces.

2.2.3 Grid corrections

Each refined region in the domain is represented by different grids at different levels of resolution, producing multiple solutions for the same region. For consistency the coarse grids quantities are updated from the contained high resolution grids, using a volume-weighted average of the conserved quantities:

$$q^{\text{coarse}} = r^{-2} \sum q^{\text{finer}}_{i,j,k} \tag{2.1}$$

where r is the refinement factor and the sum covers the cells, in level l, contained in the coarse cell, in the level $l-1$. The exponent d refers to the weighting of the average. For cell-centered quantities, $d$is the dimensionality of the problem, for face-centered is the dimensionality minus one and for edge-centered quantities $d = 1$.

Another problem arising in refined cells is that alter the flux-conservative capabilities of the hydrodynamical methods, since at the boundary of a region, the coarse and fine cells have different values for the flux across the same boundary. In order to restore the conservation the quantities of the coarse cells are corrected with the difference between the fluxes of the

coarse and fine cells at a given boundary:

$$q^{\text{coarse}} = \tilde{q}^{\text{coarse}} - \Delta t \left(F^{\text{coarse}} - \sum_{j,k} F^{\text{fine}}_{j,k} \right) \tag{2.2}$$

where F is the flux of the quantity q in the i-axis across the cell interface. The quantity $\tilde{q}^{\text{coarse}}$ refers to the uncorrected value of the coarse cell, and the sum considers the contained fine cell over the shared interface.

2.2.4 Refinement criteria

For the hierarchical construction of the grid cells, the conditions for the adaptive refinement must be specified. Many different criteria can be applied simultaneously in a given simulation. The different criteria built in Enzo are based on: slope, baryon mass, shocks, particle mass, Jeans length, cooling time, particles, shear, optical depth, resistive length, metallicity, static regions and second derivative of a field. In this work we applied refinement criteria based on baryon mass and Jeans length:

1. *Baryon mass.* This refinement criterion refines a cell if the baryonic mass ($M_g = \rho(\Delta x)^d$) is larger than a specific value:

$$M_g > \rho_{\text{flag}} (\Delta x_{\text{root}})^d r^{\alpha l} \tag{2.3}$$

   where ρ_{flag} is the equivalent density on the root grid required for refinement (defined by the simulator), Δx_{root} is the cell size of the root grid, r is the refinement factor, l is the level and α is the parameter that defines changes the mass resolution in each level. For $\alpha = 0$ this method gives a fixed upper limit to the mass resolution, which mimics a Lagrangian method (fixed mass resolution). If $\alpha < 0$ (> 0) the refinement is more (less) aggressive, which is called super-Lagrangian (sub-Lagrangian) refinement.

2. *Jeans length.* In order to prevent artificial fragmentation, the code can be forced to refine the Jeans length by a given number of cells (Truelove et al. 1998). This is translated into the following criterion:

$$\Delta x < \left(\frac{\pi \; k_B \; T}{N_J^2 \; G \; \rho \; m_H} \right)^{1/2} \tag{2.4}$$

   where N_J is the required number of cells per Jeans length. In this work we have used $N_J = 4$ following Truelove et al. (1997).

2.2.5 Time-step

As shown in the pseudo-code in Fig. 2.5, each time the hierarchy is built, the code calculates the time-step Δt for a given level l. These time-step are based on a set of criteria which guarantees accuracy and stability on the temporal integration. The time step criteria used in this work are given by the following expressions (showing the one-dimensional case for clarity):

$$\Delta t_{\text{hydro}} = \min \left(\kappa_{\text{hydro}} \frac{a \Delta x}{c_s + |v_x|} \right)_L \tag{2.5a}$$

$$\Delta t_{\rm par} = \min\left(\kappa_{\rm part}\frac{a\Delta x}{|v_{{\rm part},x}|}\right)_L \tag{2.5b}$$

$$\Delta t_{\rm accel} = \min\left(\sqrt{\frac{\delta x}{\|\mathbf{g}\|}}\right)_L \tag{2.5c}$$

$$\Delta t_{\rm exp} = f_{\rm exp}\left(\frac{a}{\dot{a}}\right) \tag{2.5d}$$

Here $\kappa_{\rm hydro}$ is a factor which ensures that the Courant-Freidrichs-Levy condition, for the discretization of the Euler conditions, is always met. Analogous to $\kappa_{\rm hydro}$, $\kappa_{\rm part}$ ensures that no particle travels more than one cell width. The factors $\kappa_{\rm hydro}$ and $\kappa_{\rm part}$ take values between 0 and 1. Finally, the factor $f_{\rm exp}$ constraint the expansion of the simulated universe to a fraction of its original value. This is necessary to ensure the stability of the hydrodynamical solvers in comoving coordinates.

2.3 Physical equations

In this section we introduce the physical equations used and solved in our simulations.

2.3.1 Equations of motion

The Eulerian equations for a self-gravitating fluid, in a coordinate system comoving with the cosmological expansion are given by

$$\frac{\partial\rho}{\partial t} + \frac{1}{a}\nabla\cdot(\rho\mathbf{v}) = \mathbf{0} \tag{2.6}$$

$$\frac{\partial\rho\mathbf{v}}{\partial t} + \frac{1}{a}\nabla\cdot(\rho\mathbf{v}\mathbf{v} + \mathbf{I}P) = -\frac{\dot{a}}{a}\rho\mathbf{v} - \frac{1}{a}\rho\nabla\phi \tag{2.7}$$

$$\frac{\partial E}{\partial t} + \frac{1}{a}\nabla\cdot[(E+P)\mathbf{v}] = -2\frac{\dot{a}}{a}E - \frac{\rho}{a}\mathbf{v}\cdot\nabla\phi - \Lambda + \Gamma \tag{2.8}$$

corresponding to mass conservation, momentum conservation and energy conservation. In these equations, ρ, $\mathbf{v}$ and E are the comoving gas density, peculiar velocity and the comoving total fluid energy density. The matrix $\mathbf{I}$ is the identity matrix, and a is the cosmological scale factor. In the energy equation the terms Λ and Γ represent the radiative cooling and heating. The comoving total fluid energy density E is given by

$$E = e + \frac{1}{2}\rho v^2 \tag{2.9}$$

where e is the comoving thermal energy density (internal energy of a cell). The closure of the fluid equations is given by an equation of state for an ideal gas

$$e = \frac{p}{\gamma - 1} \tag{2.10}$$

where γ is the ratio of the specific heats. The gravitational potential ϕ is computed by the Poisson's equation, using the total density contrast

$$\nabla^2 = \frac{4\pi G}{a}(\rho_{\rm total} - \rho_0) \tag{2.11}$$

where $\rho_{\rm total} = \rho_{\rm gas} + \rho_{\rm dark} + \rho_{\rm stars}$ and ρ_0 is the mean density. The cosmological scale factor $a \equiv 1/(1+z)$ follows the evolution of an homogeneous and isotropic universe, given by the Friedmann equation

$$\frac{\ddot{a}}{a} = -\frac{4\pi G}{3a^3}(\rho_0 + \frac{3}{c^2}P_0) + \Lambda_{de}\frac{c^2}{3} \tag{2.12}$$

where ρ is the mean value of the comoving matter density, P_0 is the comoving pressure contribution, and Λ_{de} is the cosmological constant associated with the dark energy. The whole set of equations is limited to the non-relativistic regime and assumes that curvature effects are negligible.

The collisionless components of the system (e.g. stars, dark matter, black holes) are modeled by N-body particles following the Newton's equations of motion in comoving coordinates:

$$\frac{d\mathbf{x}}{dt} = \frac{1}{a}\mathbf{v} \tag{2.13}$$

$$\frac{d\mathbf{v}}{dt} = -\frac{\dot{a}}{a}\mathbf{v} - \frac{1}{a}\nabla\phi \tag{2.14}$$

In order to consider the interaction between particles and gas, the mass of the particles is distributed over the nearest cells, contributing to the total density in the Poisson's equation (2.11).

2.3.2 Radiative Cooling

Radiative cooling is added in equation (2.8), which correspond to energy conservation. An accurate treatment of the cooling produced by the metal content requires taking into account several transitions and chemical reactions, which translates in a higher consumption of computational resources. For this reason, most metal cooling methods rely on assumptions on the subgrid physics in order balance accuracy and speed. For this reason we employ the simplest cooling method available in Enzo which consist ins using the analytic cooling function of Sarazin & White (1987), which assumes a fully ionized gas with a constant metallicity of $0.5Z_\odot$. This allow the gas to radiative cool down to 10^4 K. We add the cooling curves defined in Rosen & Bregman (1995) to cool the gas down to 300 K, which assumes a fully ionized gas of solar metallicity.

2.3.3 Star Formation & Stellar Feedback

In Enzo includes a number of star formation models due to the different scales at which the problem can be approached and to the lack of understanding of the problem itself. These method follow a similar scheme: at a given time in the simulation, the code examines all the gas cells at the highest local level of refinement to check if they meet a set of criteria

defined by a model. If these criteria are met, some gas of the cell is taken to create a star particle, which has the same velocity as the gas cell. This star particle actually represents and ensemble of stars, which is allowed to inject mass, momentum and thermal energy among others, to its local environment.

Star Formation

We use the star formation model described in Kim et al. (2011) which represents the formation of *molecular cloud* particles. This method is modified version of the Cen & Ostriker (1992) algorithm, which assumes that stars form in overdense, converging and gravitationally unstable regions of gas. In order to create a star particle from a gas cell, the following criteria must be fulfilled: (i) the proton number density n exceeds a density threshold $n_{\rm thres}$, (ii) the velocity flow is converging (collapse), (iii) the time it takes the gas to cool has to be less that the time it takes to collapse and (iv) the resulting particle has at least a mass $m_{\rm min}$. This criteria are numerically given by:

$$n_{\rm cell} > n_{\rm thres} \tag{2.15a}$$

$$\vec{\nabla} \cdot \vec{v} < 0 \tag{2.15b}$$

$$t_{\rm cool} < t_{\rm dyn} \equiv \sqrt{\frac{3\pi}{32 G \rho_{tot}}} \tag{2.15c}$$

$$m_{\rm star} > m_{\rm min} \tag{2.15d}$$

Once the criteria are met, a new star particle is instantly created, which initial mass depend on the fixed formation efficiency ϵ_{SF}, the gas density ($\rho_{\rm gas}$), and the cell volume:

$$m_{\rm star} = \epsilon \rho_{\rm gas} \Delta x^3 \tag{2.16}$$

Stellar Feedback

After the star particles are formed a fraction $f_{\rm ej}$ of the gas content is returned slowly to the cell within $12 t_{\rm dyn}$, such that the mass of the particle as a function of time is given by

$$m_{\rm star}(t) = m_{\rm star}(0)[1 - f_{\rm ej} + f_{\rm ej}(1+\tau_0)e^{-\tau_0}] \tag{2.17}$$

where $\tau_0 = (t - t_{\rm ct})/t_{\rm dyn}$ and $t_{\rm ct}$ is the creation time of the star particle. Enzo also allows the implementation of stellar feedback due to supernovae explosions that inject energy to the surrounding gas. Although stars particle are instantly formed the simulation, these particles actually represent a group of several stars, hence the feedback energy is computed as if this group, within a single star particle, were created over a longer period of time. Quantitatively, the mass of stars formed in a cell at a time t with time step Δt is assumed to be given by

$$\Delta m_{\rm stars}(t) = m_\star \int_{\tau_0}^{\tau_1} \tau e^{-\tau} d\tau$$

$$\Delta m_{\rm stars}(t) = 0.6 m_\star [(1+\tau_0)e^{-\tau_0} - (1+\tau_1)e^{-\tau_1}] \tag{2.18}$$

where $\tau_1 = (t + \Delta t - t_{\rm ct})/t_{\rm dyn}$. Finally a fraction of the rest energy $f_{\rm SN} \Delta m_{\rm stars} c^2$, that corresponds to the massive star population within the "star particle", is injected to the

surrounding medium.

2.4 Hydrodynamic solver

For AMR techniques, each cell is solved as an independent computational fluid problem. In Enzo four different (magneto)-hydrodynamic methods are implemented: (i) the hydrodynamic-only piecewise parabolic method (PPM) developed by Colella & Woodward (1984) and extended to cosmology by Bryan et al. (1995); (ii) the MUSCL-like Godunov scheme (van Leer 1977b) with or without magnetic fields and Dedner-based divergence cleaning, described in more detail in Wang et al. (2008) and Wang & Abel (2009a); (iii) a constrained transport staggered MHD scheme (Collins et al. 2010), and (iv) the second-order finite difference hydrodynamics method described in ZEUS (Stone & Norman 1992).

For our simulations we use the ZEUS method which is less computationally demanding, allowing us to perform several realizations.

2.4.1 ZEUS

The ZEUS method is a three-dimensional hydrodynamical solver which uses Cartesian grids such that velocities are face-centered, while density and internal energy are cell-centered. The fluid transport is solved using the upwind, monotonic advection scheme of van Leer (1977b). This method is formally second-order accurate in space but first-order accurate in time.

The first terms on the right-hand side of equations (2.7) and (2.8), correspond to expansion terms arising from the comoving reference frame. These terms are split from the rest of the terms and solved using an time-centered method. These terms do not constitute a major source of error. Then, the method splits the remainder of the terms into two steps. The first is the source step (right-hand side of equations (2.6), (2.7) and (2.8)), in which the momentum and energy values are updated to reflect the pressure and gravity forces, including an artificial viscosity required for stability. The second step, known as the transport step, accounts for the advection of conserved quantities (mass, momentum, and energy) across the grid given by the terms in the left-hand side of the Euler equations .

The ZEUS method includes a von Neumann-Richtmyer artificial viscosity in order to smooth shock discontinuities that may appear in fluid flows and can cause a breakdown of the finite difference equations. The artificial viscosity term is added in the source terms as:

$$\rho\frac{\partial \mathbf{v}}{\partial t} = -\nabla P - \rho\nabla\phi - \nabla\cdot\mathbf{Q} \tag{2.19}$$

$$\frac{\partial e}{\partial t} = -P\nabla\cdot\mathbf{v} - \mathbf{Q}:\nabla\mathbf{v} \tag{2.20}$$

where $\mathbf{Q}$ is the artificial viscosity diagonal stress tensor with terms given by $l^2\rho(\partial/\partial x)^2$. The length scale l determines the width of the shocks and is typically a few times the cell size.

The source terms are added in three steps. First the velocities in the interfaces, $v_{j-1/2}$

,are corrected by pressure and gravity:

$$v_{j-1/2}^{n+a} = v_{j-1/2}^{n} - \frac{\Delta t}{\Delta x_j}\frac{P_j^n - P_{j-1}^n}{(\rho_j^n + \rho_{j-1}^n)/2} - \frac{\Delta t}{\Delta x_j}(\phi_j^n - \phi_{j-1}^n) \tag{2.21}$$

This equation correspond to the partial temporal update of $v_{j-1/2}$ (partial updates are denoted by $n+a$, $n+b$, $n+c$) in one dimension j. In the second step the velocity and internal energy is corrected by the artificial viscosity:

$$v_{j-1/2}^{n+b} = v_{j-1/2}^{n+a} - \frac{\Delta t}{\Delta x_j}\frac{q_j^{n+a} - q_{j-1}^{n+a}}{(\rho_j^n + \rho_{j-1}^n)/2} \tag{2.22}$$

$$e_j^{n+b} = e_j^n - \frac{\Delta t}{x_j} q_j^{n+a}(v_{j+1/2}^{n+a} - v_{j-1/2}^{n+a}) \tag{2.23}$$

The artificial viscosity coefficient q_j is given by:

$$q_j = \begin{cases} Q_{\mathrm{AV}}\rho_j(v_{j+1/2} - v_{j-1/2})^2 & \text{if } (v_{j+1/2} - v_{j-1/2}) < 0 \\ 0 & \text{otherwise} \end{cases} \tag{2.24}$$

where Q_{AV} is a constant which corresponds to the number of cells and has a typical value of 2. The ZEUS method also includes the option of adding linear artificial viscosity (which is not used in our simulations), given by

$$q_{\mathrm{lin},j} = Q_{\mathrm{LIN}}\rho c_j(v_{j+1/2} - v_{j-1/2}) \tag{2.25}$$

where $c_j^2 = \gamma P/\rho$ is the adiabatic sound speed. The third step corresponds to the compression term, given by

$$e_j^{n+c} = e_j^{n+b}\left(\frac{1 - (\Delta t/2)(\gamma-1)(\nabla\cdot\mathbf{v})_j}{1 + (\Delta t/2)(\gamma-1)(\nabla\cdot\mathbf{v})_j}\right) \tag{2.26}$$

Finally the transport step for fluid advection is applied. This is done by solving finite-difference approximations to the integral equations

$$\frac{d}{dt}\int_V \rho dV = -\int_{\delta V}\rho\mathbf{v}\cdot\mathbf{dS} \tag{2.27}$$

$$\frac{d}{dt}\int_V \rho\mathbf{v} dV = -\int_{\delta V}(\rho\mathbf{v})\mathbf{v}\cdot\mathbf{dS} \tag{2.28}$$

$$\frac{d}{dt}\int_V e dV = -\int_{\delta V} e\mathbf{v}\cdot\mathbf{dS} \tag{2.29}$$

The transport step is done in one direction at a time, in the order x, y and z. In the case of the equation (2.27) the solution is:

$$\rho_j^{n+d} = \rho_j^n - \frac{\Delta t}{\Delta x}(v_{j+1/2}^{n+c}\rho_{j+1/2} - v_{j+1/2}^{n+c}\rho_{j+1/2}) \tag{2.30}$$

corresponding to the evolution for the cell-centered value of ρ given by the flux $\rho\mathbf{v}$ at cell boundary, guaranteeing mass conservation, This requires the interpolation of each cell-centered quantity (in this case density) across the cell faces. In the Enzo implementation of

ZEUS, this is done by using the second order van Leer (1977) scheme, which uses piecewise linear functions. The upwinded interpolated value for the density is

$$\rho_{j+1/2} = \begin{cases} \rho_j + (\Delta x_j - v_{j+1/2}\Delta t)(d\rho_j/2) & \text{if } v_{j+1/2} > 0 \\ \rho_{j+1} - (\Delta x_{j+1} + v_{j+1/2}\Delta t)(d\rho_{j+1}/2) & \text{if } v_{j+1/2} < 0 \end{cases} \tag{2.31}$$

where Δq_j are the monotonized, van Leer slopes computed from the harmonic average

$$dq_j = \begin{cases} \frac{2(\Delta q_{j-1/2}\Delta q_{j+1/2})}{\Delta q_{j-1/2}+\Delta q_{j+1/2}} & \text{if } \Delta q_{j-1/2}\Delta q_{j+1/2} > 0 \\ 0 & \text{otherwise} \end{cases} \tag{2.32}$$

where $\Delta q_{j+1/2} = (q_{i+j} - q_j)/\Delta x_j$. The van Leer method offers less diffusion combined with speed.

2.5 Gravity and N-body

In this section we show the different algorithms used in Enzo to compute the accelerations in gas cells and particles.

2.5.1 Self-Gravity

To compute the acceleration produced by gas cells and particles, Enzo solves the Poisson's equation (2.11) in three steps: (i) computing the total gravitating mass, (ii) solving the gravitational potential field with defined boundary conditions and (iii) computing the gradient of the gravitational potential to get the accelerations in the gas cells and interpolating the solution for the particles. First, the mass of particles is distributed onto the neighbouring grids, in order to form a local density field, using the second-order cloud-in-cell (CIC) interpolation technique (Hockney & Eastwood 1988). We use the default number of 8 grids to be used in this scheme. For the CIC interpolation, particles are advanced by $0.5v^n\Delta t$, i.e. a half time-step, and then the mass is distributed in the following way: an imaginary cube is built centered on the particle, as shown in Figure 2.6, and then the fraction of mass distributed on each cell corresponds to the fraction of the volume shared by the imaginary cube and the cells.

To add the densities corresponding to the grids, the baryonic cells are treated as virtual CIC particles which are also advanced by $0.5v^n\Delta t$ in order to time center the resulting acceleration. This procedure results in a total gravitating density field $\rho_{\text{total}}^{n+1/2}$. To compute the potential field on the root grid, Enzo uses a fast Fourier transform. The procedure depends on the boundary conditions. For periodic boundary conditions, Greens function of the Fourier spaced are used (Hockney & Eastwood 1988):

$$G(\mathbf{k}) = -\frac{\Delta x}{2(\sin(k_x\Delta x/2)^2 + \sin(k_y\Delta y/2)^2 + \sin(k_z\Delta z/2)^2)} \tag{2.33}$$

where $k^2 = k_x^2 + k_y^2 + k_z^2$ is the wave-number in Fourier space. Then the gravitational potential is computed in Fourier space

$$\tilde{\phi}(\mathbf{k}) = G(\mathbf{k})\tilde{\rho}(\mathbf{k}) \tag{2.34}$$

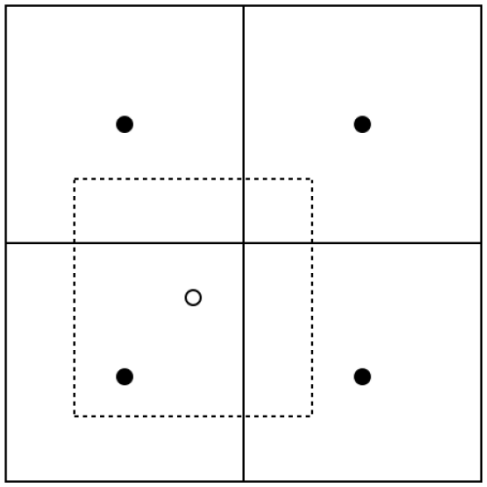

Figure 2.6: Illustration of the Cloud-in-Cell algorithm for the particle's mass distribution.

For isolated boundary conditions Enzo uses the method defined by James (1977), where the Greens function is generated in real space to correct the zero-padding properties (adding empty boxes around the simulation box) and then it is transformed into the Fourier space. Then the potential in equation (2.34) is transformed into the real domain to get the potential at the center of the cells and differenced to obtain the accelerations at the cell-faces. For particles, the accelerations are obtained form a linear CIC interpolation from the grid.

For the subgrids the generation of the total gravitating density field is done by the CIC technique. To compute the potential on subgrids, Enzo uses the standard seven-point second-order finite difference approximation to Poisson's equation. The potential equation on each subgrid is then solved with the given Dirichlet boundary conditions, interpolated form the parent grids, with a multigrid relaxation technique. To prevent oscillations with the neighbouring parent grids six ghost zones are added. The effective resolution of the gravitational forces is approximately twice as coarse as the grid spacing at a given level of resolution.

2.5.2 External Gravity

Enzo allows the simulator to define a potential field in the initialization of the problem. This can be done by adding an analytic external potential or the corresponding acceleration field. In this fashion there is no need to solve the Poisson's equation for a given component. In our simulations we use this scheme to add acceleration fields corresponding to smooth distributions of dark matter and stars.

2.5.3 N-body

Enzo uses a particle-mesh N-body method to calculate the trajectories of the collisionless particles. As mentioned in 2.5.1 the gravitational potential is computed by solving the Poisson's equation and it is differenced to obtain the accelerations, which are interpolated back to particles. The density used in the Poisson's equation corresponds to the time centered density field, $\rho_{\text{total}}^{n+1/2}$, and so we have time centered accelerations for each particle, $\mathbf{g}^{n+1/2}$.

These accelerations are used to update the position $\mathbf{x}^n$ and velocity $\mathbf{v}$ performing the standard drift-kick-drift technique:

$$\mathbf{x}^{n+1/2} = \mathbf{x}^n + \frac{\Delta t}{2a^2}\mathbf{v}^n \tag{2.35a}$$

$$\mathbf{v}^{n+1} = \mathbf{v}^n \left(1 - \frac{\dot{a}^{n+1/2}}{a^{n+1/2}}\right) + \frac{\Delta t}{a^{n+1/2}}\mathbf{g}^{n+1/2} \tag{2.35b}$$

$$\mathbf{x}^{n+1} = \mathbf{x}^{n+1/2} + \frac{\Delta t}{2a^{n+1}}\mathbf{v}^{n+1} \tag{2.35c}$$

Chapter 3

Simulations

For this work we have performed two different sets of simulations, spiral and starburst galaxies, which allow us to probe different time, length and density scales, while reaching different resolutions. The disk galaxies have a few tens of kiloparsecs in diameter while the starburst nuclear regions have around six hundred parsecs of size. The simulations are evolved in comoving coordinates in a ΛCDM universe from a redshift $z = 0.2$, where we have adopted the values $\Omega_{\rm m} = 0.3$, $\Omega_\Lambda = 0.7$, and $H_0 = 67 {\rm kms}^{-1}{\rm Mpc}^{-1}$, which effects are only noticeable in the spiral galaxies. The criteria used for refinement is of two kinds and both of them have to be fulfilled: refinement by baryon mass if the density of the cell is δ times the average density, and refinement by Jeans length to ensure that it is at least resolved by 4 cells to prevent artificial fragmentation (Truelove et al. 1997). We choose $\delta = 4$ for spiral galaxies and $\delta = 100$ for starburst. For spiral galaxy simulations we choose a time interval between simulation $\Delta t \sim 40$ Myr and $\Delta t \sim 0.4$ Myr for starburst galaxies.

3.1 Spiral Galaxies

The spiral galaxies are simulated in a box of $666h^{-1}$ kpc with periodic boundary conditions from $z = 0.2$ to $z = 0$. The size of the parent grid is 128^3 and we proceed down to additional 7 sub-grids of refinement reaching a resolution of $\sim$ 40pc, which is a reasonable resolution to resolve the interaction between star formation, stellar feedback and the ISM (Ceverino & Klypin 2009).

Galaxy simulations are modelled as a four-component system which includes gas, stars particles, a stellar potential and dark matter. In the case of gas we model it using grids, while the stellar potential and DM are represented by external potentials which are fixed in time. Star particles form from the gas cells and are not added at the beginning of the simulations. The parameters for the star formation recipe are: a density threshold of $n_{\rm thres} = 7.5 \times 10^3 {\rm cm}^{-3}$, an efficiency $\epsilon = 0.01$ and a fractional ejected mass of $f_{\rm ej} = 0.4$.

3.1.1 Gas

The gas is a rotationally supported disk, initially described by an exponential profile in the radial direction R combined with a sech^2 profile in the vertical direction z, with R and z in cylindrical coordinates:

$$\rho_{\rm gas}(R,z) = \rho_0 \exp\left(-R/R_0\right) \operatorname{sech}^2\left(\frac{z}{2z_0}\right), \tag{3.1}$$

where R_0 is the disk scale-length, z_0 is the disk scale-height and ρ_0 is the central density. Integrating equation (3.1) we obtain

$$\rho_0 = \frac{M_{\rm gas}}{8\pi z_0 R_0^2} \tag{3.2}$$

Therefore the distribution of gas is determined fully by R_0, z_0 and the total gas mass $M_{\rm gas}$. For the spiral galaxy set of simulations we will use $R_0 = 35$ kpc, $z_0 = 0.4$ kpc and $M_{\rm gas} = 10^{10}{\rm M}_\odot$.

3.1.2 Stars

To model the stellar component of the external potential we use a Miyamoto-Nagai profile(Miyamoto & Nagai 1975), which allow us to model the stellar disk and bulge of the galaxy, where the potential is given by:

$$\Phi_{\rm star}(R,z) = -\frac{GM_{\rm star}}{\sqrt{R^2 + (a + \sqrt{z^2+b^2})^2}} \tag{3.3}$$

When $a = 0$, this potential reduces to the Plummer's spherical potential (Plummer 1911) and when $b = 0$ it corresponds to the Kuzmin's potential of a razor thin disk (Kuzmin 1956). This component is implemented as a acceleration field given by $-\nabla\Phi_{\rm star}$

$$\frac{\partial\Phi}{\partial R} = -\frac{GM_{\rm star}R}{(R^2 + (a + \sqrt{z^2+b^2})^2)^{3/2}} \tag{3.4a}$$

$$\frac{\partial\Phi}{\partial z} = -\frac{GM_{\rm star}z}{(R^2 + (a + \sqrt{z^2+b^2})^2)^{3/2}} \frac{a + \sqrt{z^2+b^2}}{\sqrt{z^2+b^2}} \tag{3.4b}$$

We adopt the fixed values $a = 35$ kpc and b =0.2kpc. For the total mass in stars $M_{\rm star}$ we take two different values, $10^{10}{\rm M}_\odot$ and $10^{11}{\rm M}_\odot$ which would derive in different contributions to the total rotation.

3.1.3 Dark Matter

We consider DM as an external gravitational field given by a Navarro-Frenk-White profile (Navarro et al. 1997) which changes slightly through the evolution of the galaxies due to its dependence with the Hubble parameter H, given by

$$H^2(z) = H_0^2(\Omega_\Lambda + \Omega_m(1+z)^3) \tag{3.5}$$

This approach allow us to focus only on the gas dynamics. The potential for this distribution of DM is given analytically by

$$\Phi_{\rm DM}(r) = \frac{\rho_{\rm crit}\delta_c}{(r/r_s)(1+r/r_s)^2} \tag{3.6}$$

where $r_s = r_{200}/c$ is a characteristic radius, $\rho_{\rm crit} = 3H^2/8\pi G$ is the critical density, c is the concentration parameter, and δ_c is given by:

$$\delta_c = \frac{200}{3}\frac{c^3}{[\ln(1+c) - c(1+c)]} \tag{3.7}$$

The characteristic radius r_{200} corresponds to the volume at which the mean density is 200 times the critical density

$$M_{200} = 200\rho_{\rm crit}\frac{4\pi}{3}r_{200}^3 \tag{3.8}$$

We will adopt a value $c = 12$ for the concentration parameter while M_{200} will take the values $10^{10}{\rm M}_\odot$ and $10^{11}{\rm M}\odot$ for the simulations with $M_{\rm star} = 10^{10}{\rm M}_\odot$ and $10^{11}{\rm M}_\odot$ respectively.

3.2 Starburst galaxies

For starburst galaxies we only simulate the central nuclear disks which are initialized within a box of physical size 4 kpc with isolated boundary conditions. The size of the parent grid is 32^3, and we proceed down to additional six levels of refinement, reaching a resolution of ~ 2 pc. Our initial model consists in a massive gaseous disk embedded in a stellar spheroid, which is modeled by a time-independent external potential. The initial gas and stellar components are in the next subsections. The parameters for the star formation recipe are: a density threshold of $n_{\rm thres} = 7.5 \times 10^5{\rm cm}^{-3}$, an efficiency $\epsilon = 0.01$ and a fractional ejected mass of $f_{\rm ej} = 0.4$.

3.2.1 Gas

We initialize the gas as a rotationally supported disk with an R^{-1} power law for the cylindrical radius and a sech^2 function for the vertical component:

$$\rho_{\rm gas}(R,z) = \rho_0\left(\frac{R_0}{R}\right){\rm sech}^2\left(\frac{z}{2z_0(R)}\right), \tag{3.9}$$

where R_0 is the radial scale-length, $z_0(R)$ is the height scale-length as a function of radius, and ρ_0 is the central volumetric density. We choose z_0 to be a function of radius so the initial configuration is close to vertical equilibrium. For an isothermal disk this is given by

$$z_0(R) = \sqrt{\frac{c_{\rm s}^2}{8\pi G\rho(R,0)}} = c_{\rm s}\sqrt{\frac{R}{8\pi G\rho_0 R_0}} \tag{3.10}$$

where $\rho(R,0)$ is the density at the midplane and c_s is the sound speed which is initially constant. Integrating equation (3.9) along the z-axis we obtain the surface density

$$\Sigma(R) = \int_{-\infty}^{\infty}\rho_{\rm gas}(R,z)dz = 4\rho_0\left(\frac{R_0}{R}\right)z_0(R) = c_{\rm s}\sqrt{\frac{2R_0\rho_0}{\pi GR}} \tag{3.11}$$

which leads to a total mass $M_{\rm gas}$ as a function of $c_{\rm s}$, R_0, ρ_0 and G

$$M_{\rm gas} = 2\pi \int_0^{R_0} \Sigma(R') R' dR' = \frac{4\pi c_{\rm s}}{3}\sqrt{\frac{2\rho_0 R_0^4}{\pi G}} \Rightarrow \rho_0 = \frac{9GM_{\rm gas}}{32\pi c_{\rm s}^2 R_0^4} \tag{3.12}$$

Replacing (3.12) in (3.10) we obtain $z_0(R)$ as a function of the user defined parameters $M_{\rm gas}$, R_0 and $c_{\rm s}$ (the defined parameter is the temperature)

$$z_0(R) = \frac{2}{3}\frac{c_{\rm s}^2}{GM_{\rm gas}}\sqrt{RR_0^3} \tag{3.13}$$

The values adopted for this set are $R_0 = 300\,{\rm pc}$ for the disk scale-length and $M_{\rm gas} = 4{\times}10^8 {\rm M}_\odot$ for the total gas mass. Finally, the initial gaseous disk is truncated at R_0, and we add random density and temperature fluctuations of less than 10%.

3.2.2 Stars

The stellar spheroid is modeled by an analytical approximation of the non-singular isothermal sphere which does not have an analytical expression. This is accomplished by the merge of two analytical density functions such that the resulting expression shares some properties with an isothermal sphere. For $r < r_0$ we use a fourth order polynomial, while the asymptotic solution for $r > r_0$ is given by the singular isothermal sphere

$$\rho_{\rm star}(r) = \rho_0 \begin{cases} \sum_{n=0}^{4} a_n \left(\frac{r}{r_0}\right)^n & \text{if } r < r_0 \\ \frac{2}{9}\left(\frac{r}{r_0}\right)^2 & \text{if } r \geq r_0 \end{cases} \tag{3.14}$$

being $r_0 = \sqrt{9\sigma^2/(4\pi G\rho_0)}$ the King radius (Binney & Tremaine 2008), where σ is the velocity dispersion and ρ_0 the stellar density at the center of the disk. In the case of the polynomial, we impose four constraints to determine the coefficients: the function and its first derivative (i,ii) have the same value of an isothermal sphere at the center, and (iii,iv) are continuous at $r = r_0$. The first two conditions lead to $a_0 = 1$ and $a_1 = 0$ while the last two result in the equations

$$1 + a_2 + a_3 + a_4 = \frac{2}{9} \qquad \& \qquad 2a_2 + 3a_3 + 4a_4 = -\frac{4}{9} \tag{3.15}$$

This can be reduced to one variable with $a_2 = a_4 - 17/9$ and $a_3 = 10/9 - 2a_4$. The value of a_4 which minimizes the sum of the squared differences, of this function and the actual value of the non-singular isothermal sphere, is $a_4 = 1.09$. For simplification we adopt $a_4 = 1$ which produces a difference of less than 1% on the residual sum of squares (with respect to $a_4 = 1$). Finally the stellar density is given by:

$$\rho_{\rm star}(r) = \rho_0 \begin{cases} \left[1 - \frac{8}{9}\left(\frac{r}{r_0}\right)^2 - \frac{8}{9}\left(\frac{r}{r_0}\right)^3 + \left(\frac{r}{r_0}\right)^4\right] & \text{if } r < r_0 \\ \frac{2}{9}\left(\frac{r}{r_0}\right)^2 & \text{if } r \geq r_0 \end{cases} \tag{3.16}$$

We choose the fixed value $r_0 = 100$ pc for the set of starburst galaxy simulations.

3.3 Model Parameters

We have performed a total of six simulations, two spiral galaxies and four nuclear disks of starbursts galaxies. The initial configuration of each galaxy is set by several length scales and characteristic masses of gas, stars and/or DM, which will translate on different density distributions, vertical accelerations and rotational velocity curves. Due to the fast settling of gas on the mid-plane, different amounts of initial gas would change significantly not only the needed rotation against self-gravity but also the vertical acceleration on the disk, and thus the free-fall times of the gas cells. On the other hand, different external potentials whose masses are distributed on larger vertical scale-lengths, like spherically symmetric potentials, will not change the vertical free-fall times significantly and would allow us to nearly isolate the effects of rotation. Then, we focus our study on the effects of rotation by fixing the total gas mass and the length scales of the different models, to constant values whereas the mass that correspond to the external potentials (stars and/or dark matter) is a free parameter.

The simulated spiral galaxies both have a gas mass of $10^{10}\mathrm{M}_\odot$ and the corresponding length scales $R_0 = 35$ kpc and $z_0 = 0.4$ kpc, previously introduced for the exponential disk. For the Miyamoto-Nagai stellar component we adopt the fixed values $a = 35$ kpc and $b = 0.2$ kpc whereas for the total mass in stars $M_{\rm star}$ we take two different values, $10^{10}\mathrm{M}_\odot$ and $10^{11}\mathrm{M}_\odot$. In the case of the NFW DM halo, we adopt $c = 12$ for the concentration parameter while M_{200} will take the values $10^{10}\mathrm{M}_\odot$ and $10^{11}\mathrm{M}_\odot$. The initial temperature is set to 10^4 K for the whole simulation box.

For starburst galaxies, the total mass of gas is set to $4\times10^8 M_\odot$ and a radial scale length of $R_0 = 300$ pc, while the mass of the stellar spheroid in such a way that the velocity dispersion σ is 100, 130, 190 and 220 km/s. The initial temperature is uniform and is chosen such that the Toomre parameter $Q \equiv \kappa c_s/\pi G\rho$ is below 1 within 300 pc. We let each simulation evolve adiabatically for $1.5t_{\rm orb}$, after which radiate cooling is turned on. We do this to allow the initial perturbations to propagate through the disk and to remove any artifice produced by the initial conditions. Table 3.1 summarizes the parameters used in these runs. For starburst galaxies, Table 3.1 indicates the value of stellar mass within 300 pc ($M_\star$) and period for a circular orbit, $t_{\rm orb}$, at the same radius with its corresponding angular velocity Ω. For spiral galaxies, Table 3.1 shows the value of $t_{\rm orb}$ and Ω measured at 10 kpc.

3.4 Initial profiles

The computation of the star formation laws at global scales involves averages over a large cylindrical region of the space which will be characterized by their radial profiles for the angular velocity and density. In order to maximize the effects of rotation and to minimize the effects of the mass distribution, the angular profiles should only differ in amplitude and the distribution of gas must be initially the same. Figures 3.1 and 3.2 show the surface density profiles for our set of simulations, where starburst disks are shown after a time $1.5t_{\rm orb}$ at which radiative cooling is turned on. Since spiral galaxies are allowed to cool from the beginning of the simulations, both simulations start with the same surface density profiles. On the other

Spiral Galaxies						
Run	$M_{gas}[M_\odot]$	$M_{star}[M_\odot]$	$M_{DM}[M_\odot]$	t_{orb} [Myr]	Ω [Myr^{-1}]	Δx [pc]
GD1	1×10^{10}	1×10^{10}	1×10^{10}	639.9	0.982×10^{-2}	37.957
GD2	1×10^{10}	1×10^{11}	1×10^{11}	275.5	2.281×10^{-2}	37.957
Starburst Galaxies						
Run	$M_{gas}[M_\odot]$	$M_{star}[M_\odot]$	σ [km/s]	t_{orb} [Myr]	Ω [Myr^{-1}]	Δx [pc]
SD1	4×10^8	1.24×10^9	100	11.5	0.546	1.949
SD2	4×10^8	2.10×10^9	130	9.3	0.675	1.949
SD3	4×10^8	4.49×10^9	190	6.6	0.952	1.949
SD4	4×10^8	6.02×10^9	220	5.8	1.083	1.949

Table 3.1: Simulation parameters

hand, starburst disks show developed variations at different radii but a global similar profile. Figures 3.3 and 3.4 show the radial profiles of the angular velocity. As expected from our choice of the model parameters, the shape of the angular velocity profiles is similar within each subset, being the amplitude of the function the main difference.

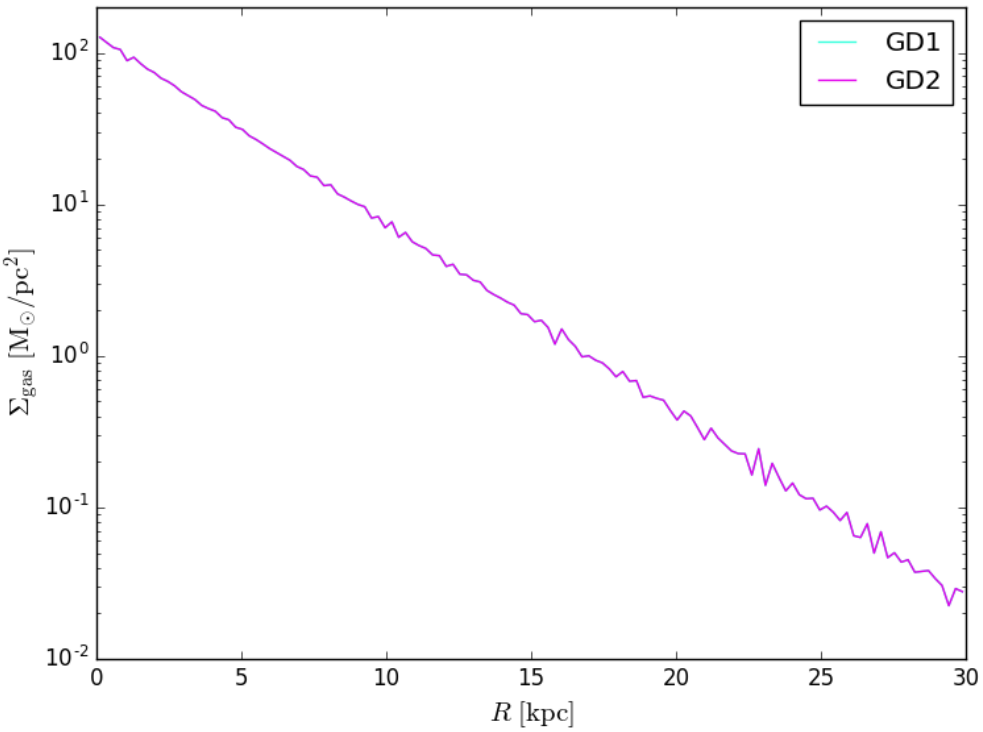

Figure 3.1: Surface density profile for spiral galaxies.

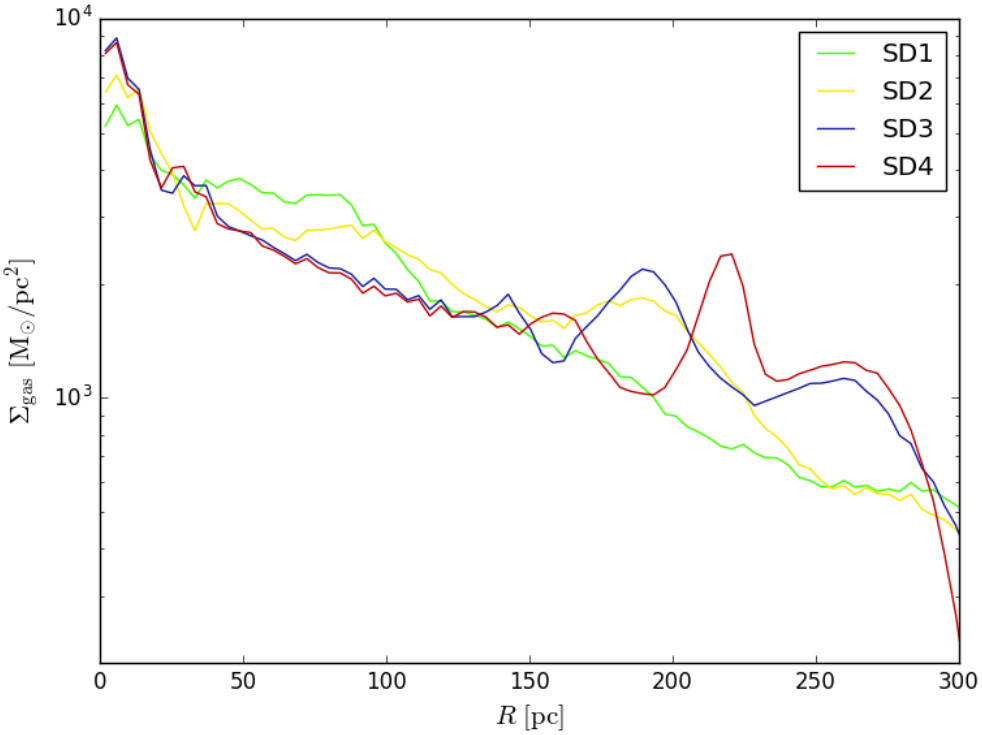

Figure 3.2: Surface density profile for starburst galaxies.

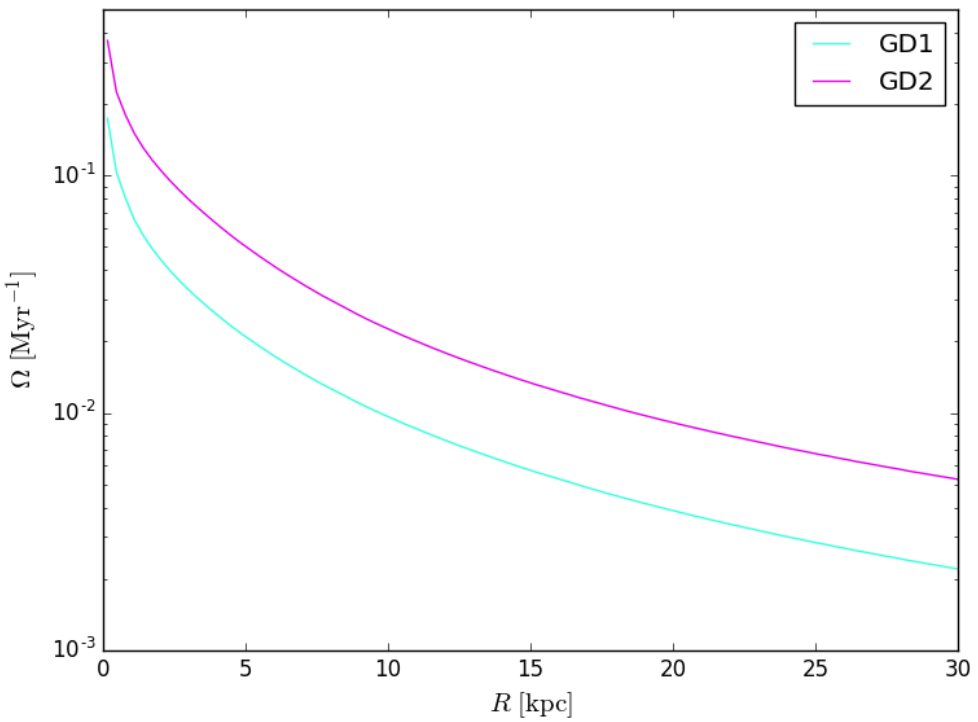

Figure 3.3: Angular velocity profile for spiral galaxies.

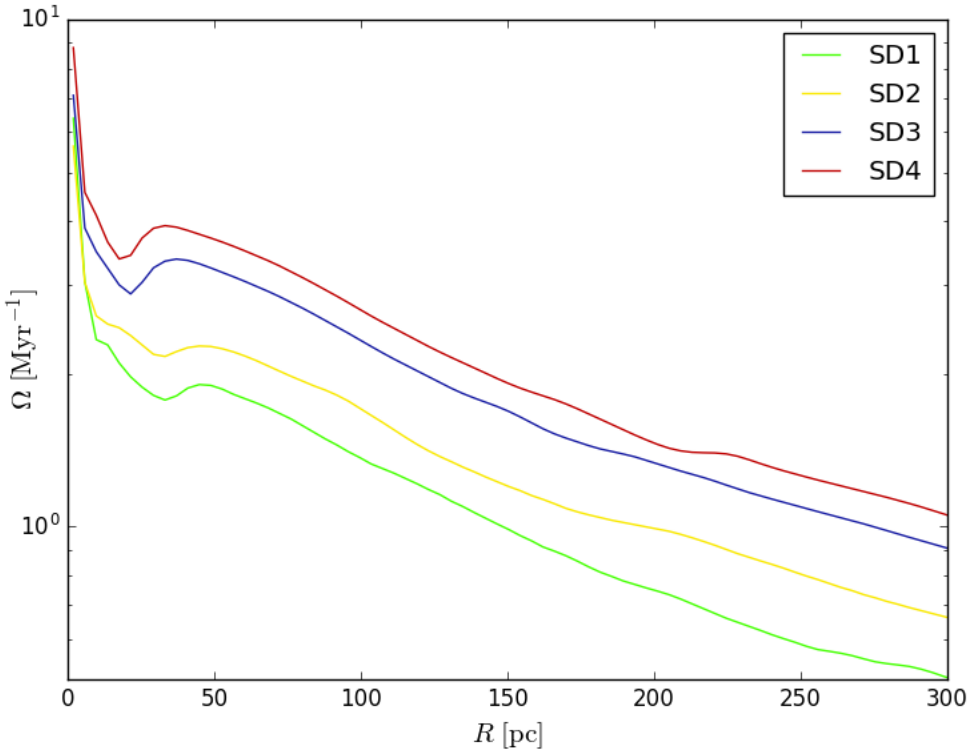

Figure 3.4: Angular velocity profile for starburst galaxies.

Chapter 4

Results and Analysis

Before analysing the star formation laws we look at the structure evolution each galaxy which is going to be affected mainly by rotation, turbulence and self-gravity. Figures 4.1-4.6 show the time evolution of spiral and starburst galaxies respectively. Snapshots represent density-weighted projections ($\langle f \rangle = \int \rho(x) f(x) dx / \int \rho(x) dx$) of gas density, temperature and the projections of stellar density along the z-axis at 0, 1, 2 and 4 Gyr for spirals and at 0, 10, 20 and 40 Myr for starbursts. The projections show filamentary structures and high density cold blobs indicating small scale instabilities growing in each disk, more evident in the starburst galaxies which show a highly turbulent medium compared to the spiral galaxies where the density distribution is softer. In addition, these density maps reveal an anti-correlation between the growth of instabilities and the magnitude of the external potential manifested in the angular velocity Ω. For the same absolute time the low-rotation disks, SD1 and GD1, appear to be more dynamically evolved, showing a more turbulent structure and a fast departure from the initial axisymmetry. For instance, the evolution in SD1 is so violent that the stellar feedback drags gas away from the disks, which is demonstrated by the low-density tails of the high-density blobs which are being pushed outwards. Then, from the notorious differences between simulations produced by different rotational profiles, we expect to see an imprint of this behaviour on the star formation rates. If we compare the evolutionary states at the same number of orbits at a given radius the contrast will get even bigger; this would be contradictory with the SE law which states that he evolution of the star formation at an equal number of orbits should be similar. Looking at the star distribution, all the simulations show a high fraction of stars are located in large clusters which would disturb their initial axisymmetry. The size of this star clusters shows to be anti-correlated with the angular velocity of the disks which is expected since the largest unstable wavelength is given by $\lambda_{\rm rot} = 4\pi^2 G\Sigma/\kappa^2$ following Toomre (1964). It also evident by looking at the second snapshot of every simulation that stars are formed faster for the runs with smaller rotational velocities.

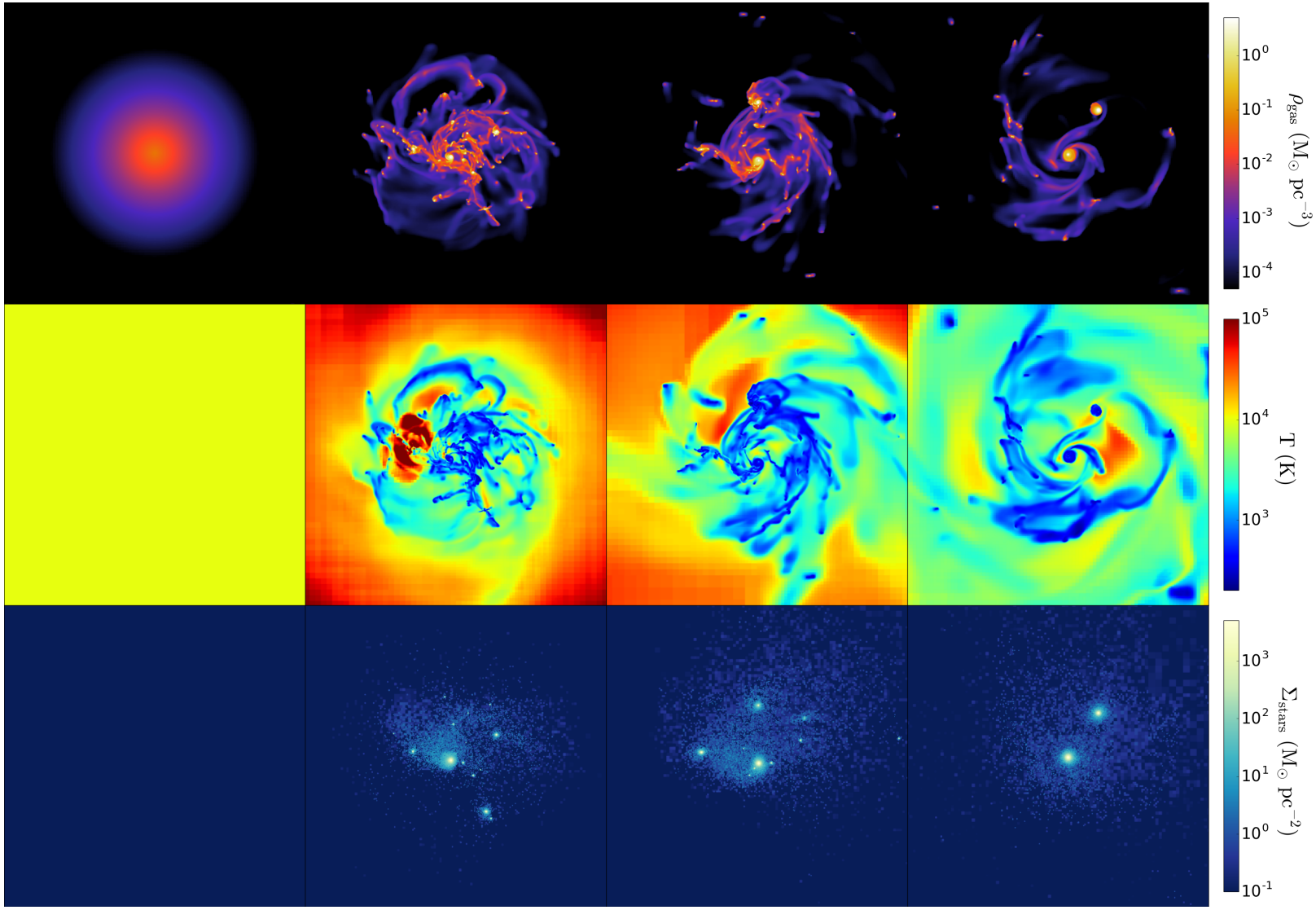

Figure 4.1: Time evolution of run GD1. From left to right the columns represent snapshots of 70kpc wide at times 0, 1, 2 and 4 Gyr. *Top*: Density-weighted projections of gas density. *Middle*: Density-weighted projections of temperature. *Bottom*: Projections of stars.

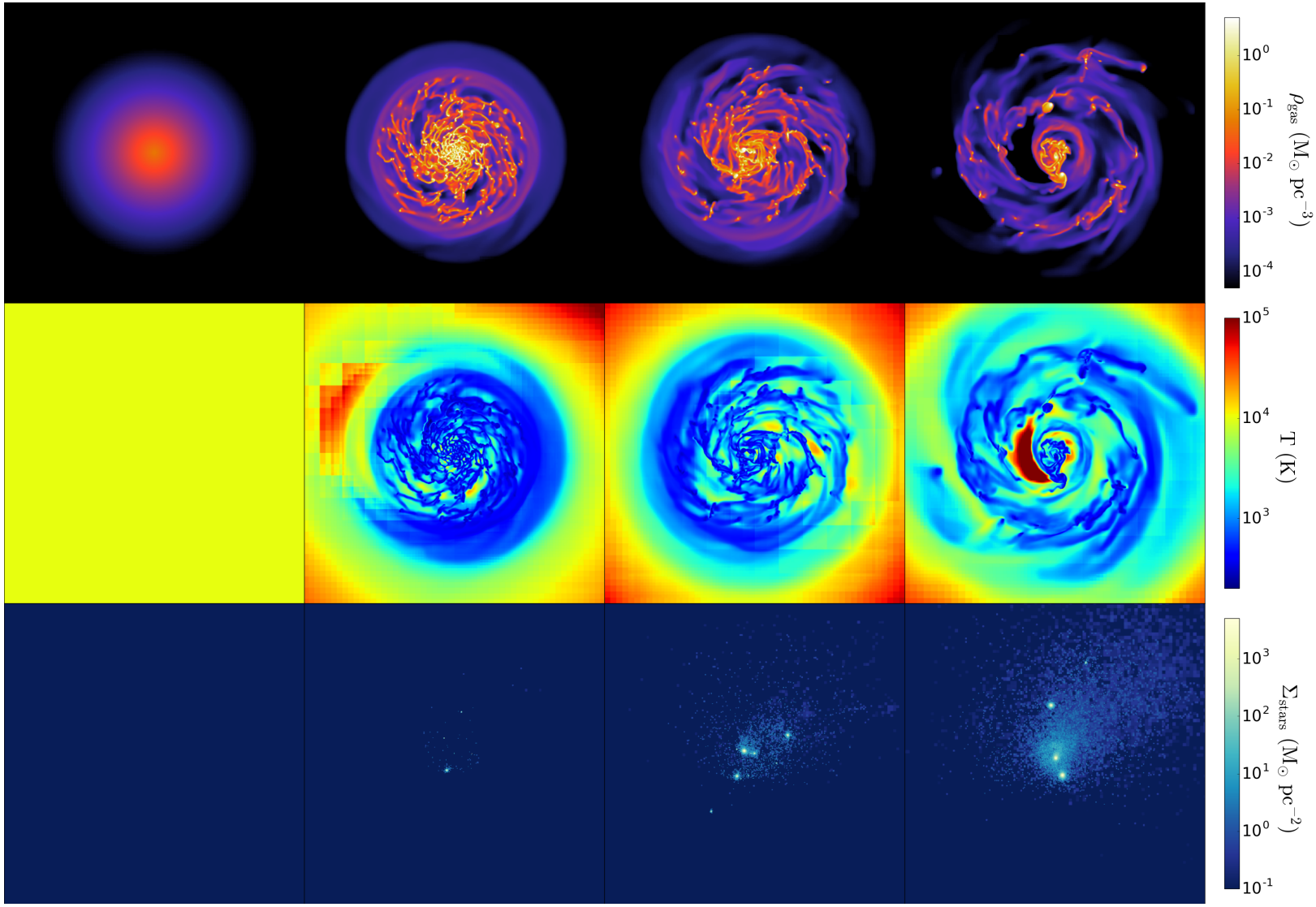

Figure 4.2: Time evolution of run GD2. From left to right the columns represent snapshots of 70kpc wide at times 0, 1, 2 and 4 Gyr. *Top*: Density-weighted projections of gas density. *Middle*: Density-weighted projections of temperature. *Bottom*: Projections of stars.

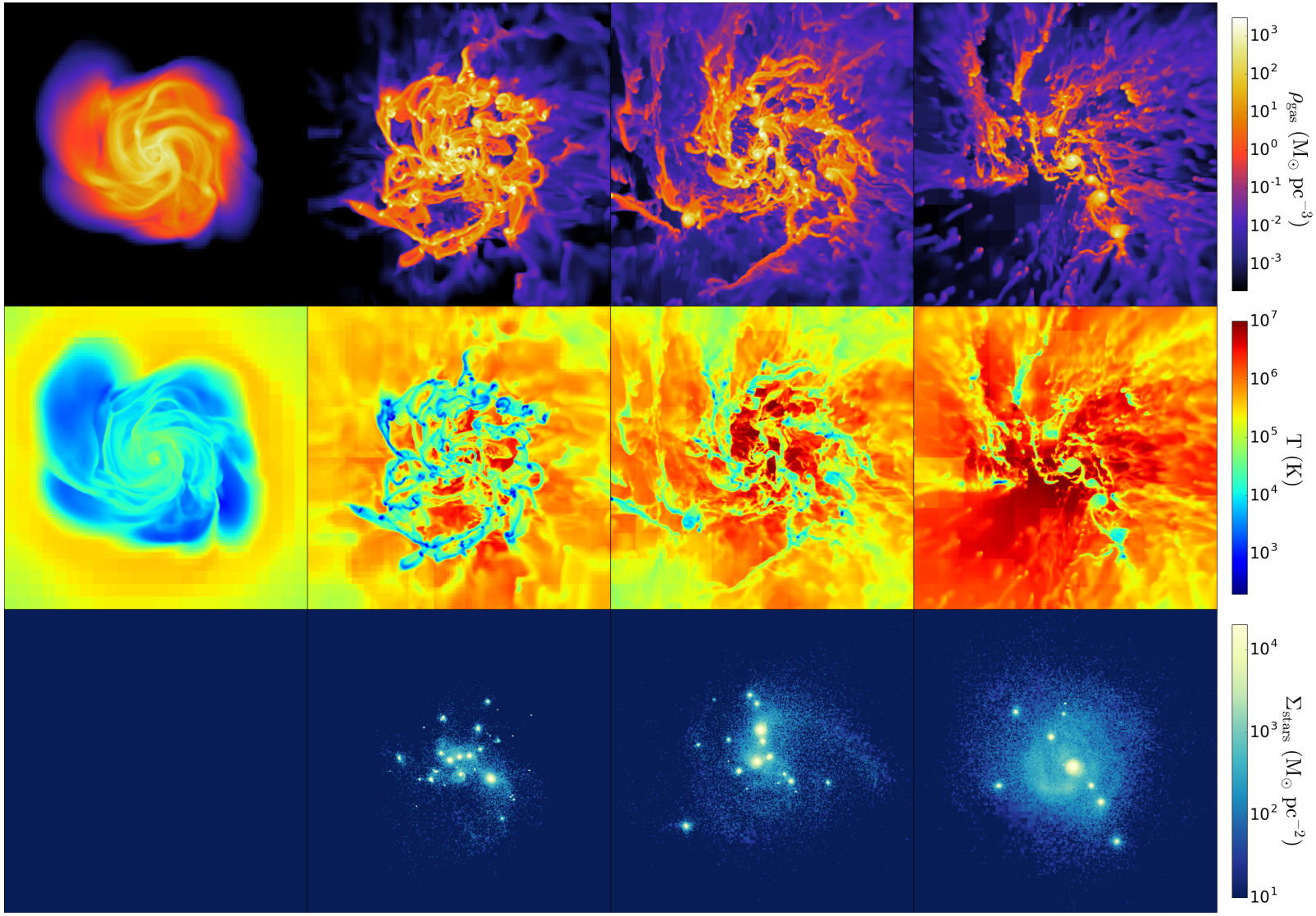

Figure 4.3: Time evolution of run SD1. From left to right the columns represent snapshots of 750pc wide at times 0, 10, 20 and 40 Myr. *Top*: Density-weighted projections of gas density. *Middle*: Density-weighted projections of temperature. *Bottom*: Projections of stars.

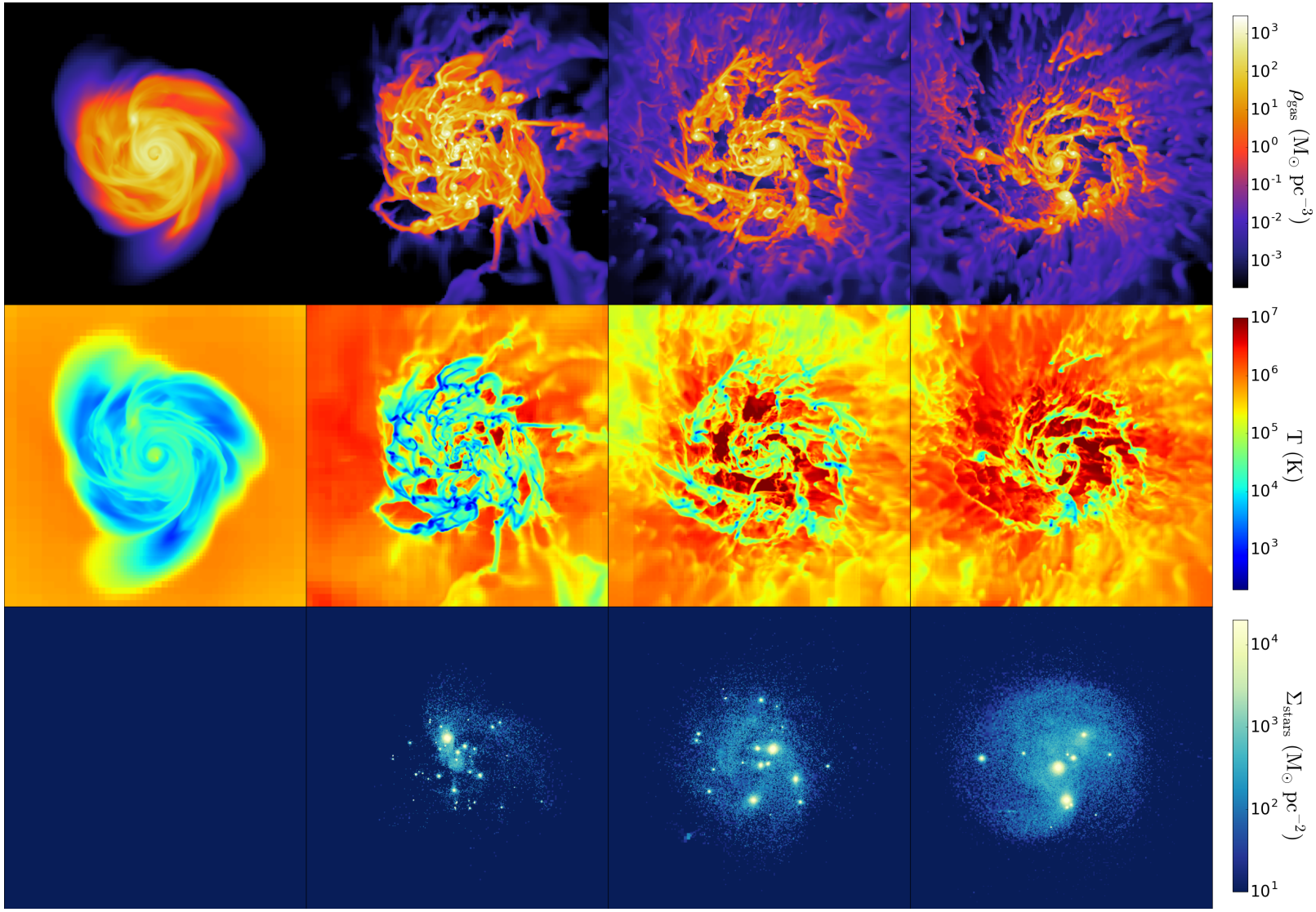

Figure 4.4: Time evolution of run SD2. From left to right the columns represent snapshots of 750pc wide at times 0, 10, 20 and 40 Myr. *Top*: Density-weighted projections of gas density. *Middle*: Density-weighted projections of temperature. *Bottom*: Projections of stars.

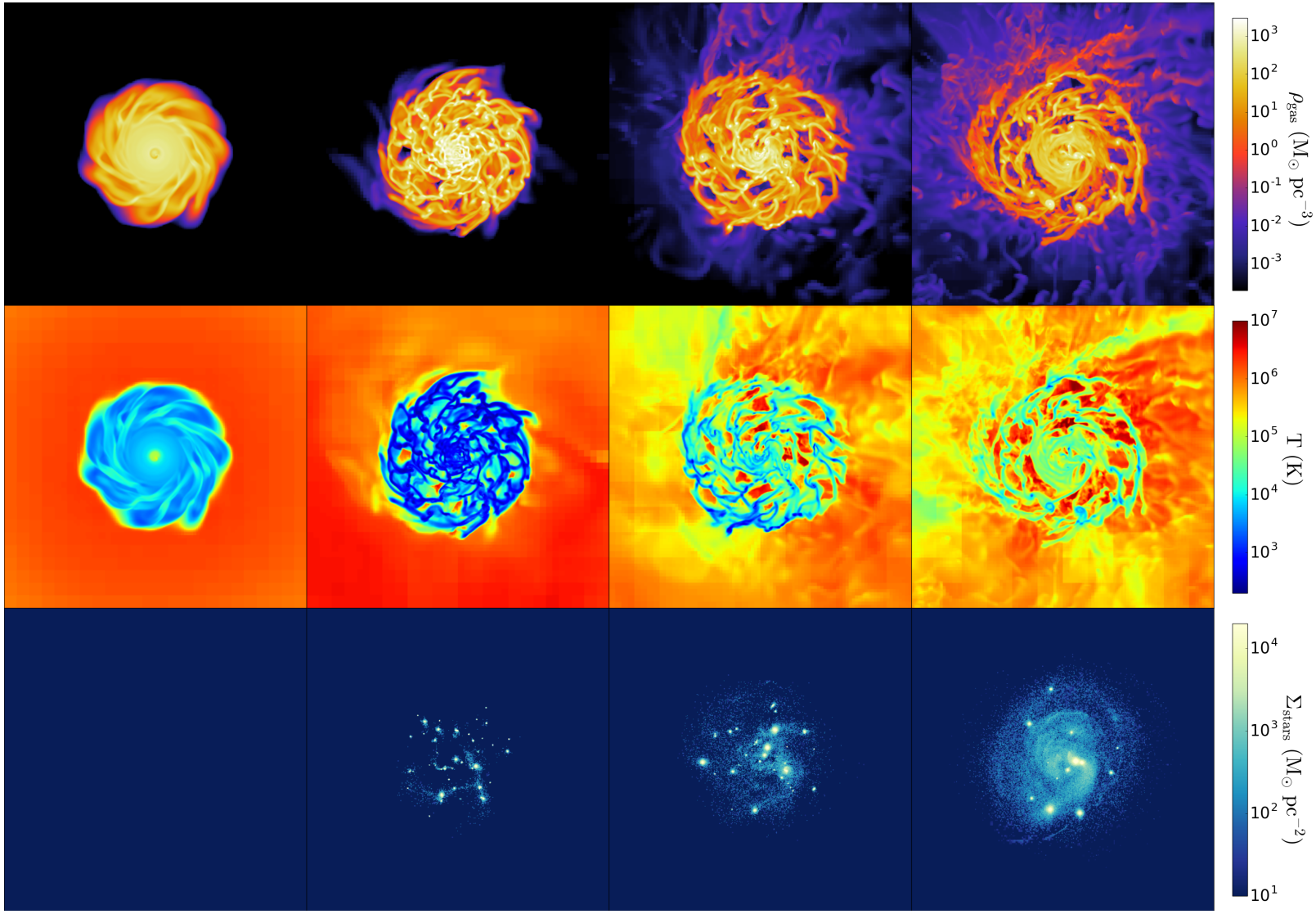

Figure 4.5: Time evolution of run SD3. From left to right the columns represent snapshots of 750pc wide at times 0, 10, 20 and 40 Myr. *Top*: Density-weighted projections of gas density. *Middle*: Density-weighted projections of temperature. *Bottom*: Projections of stars.

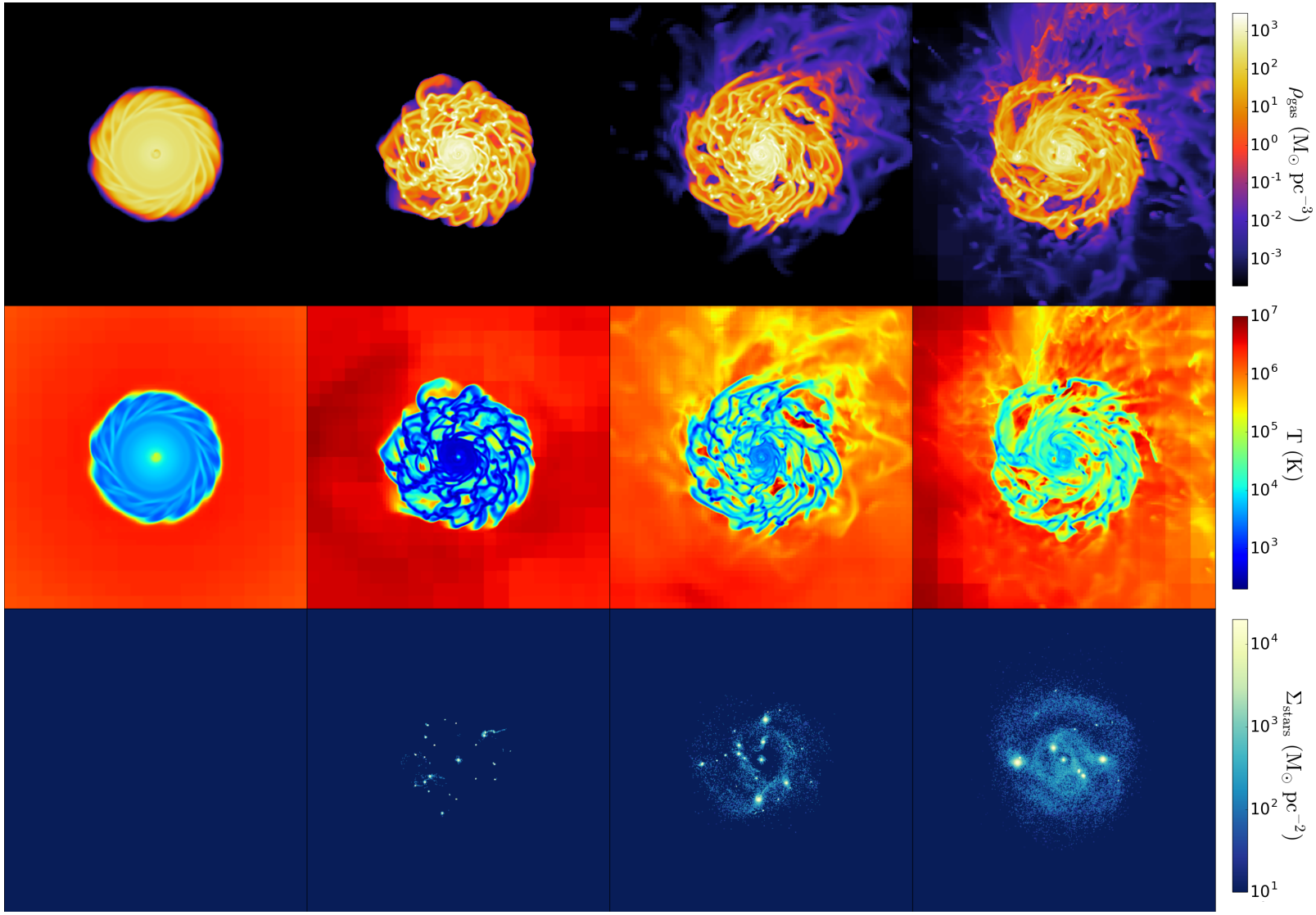

Figure 4.6: Time evolution of run SD4. From left to right the columns represent snapshots of 750pc wide at times 0, 10, 20 and 40 Myr. *Top*: Density-weighted projections of gas density. *Middle*: Density-weighted projections of temperature. *Bottom*: Projections of stars.

4.1 Disk Structure

In this section we examine the evolution of the mass distribution and angular velocity across the disks. In the following section we will compute the star formation laws averaging through the whole galactic disks. Then the mass distributions, which control the free-fall times, must remain similar within a subset through most of the time of the simulations. In a similar way, the rotational velocities across the disks should have a small variation during the evolution of the galaxies.

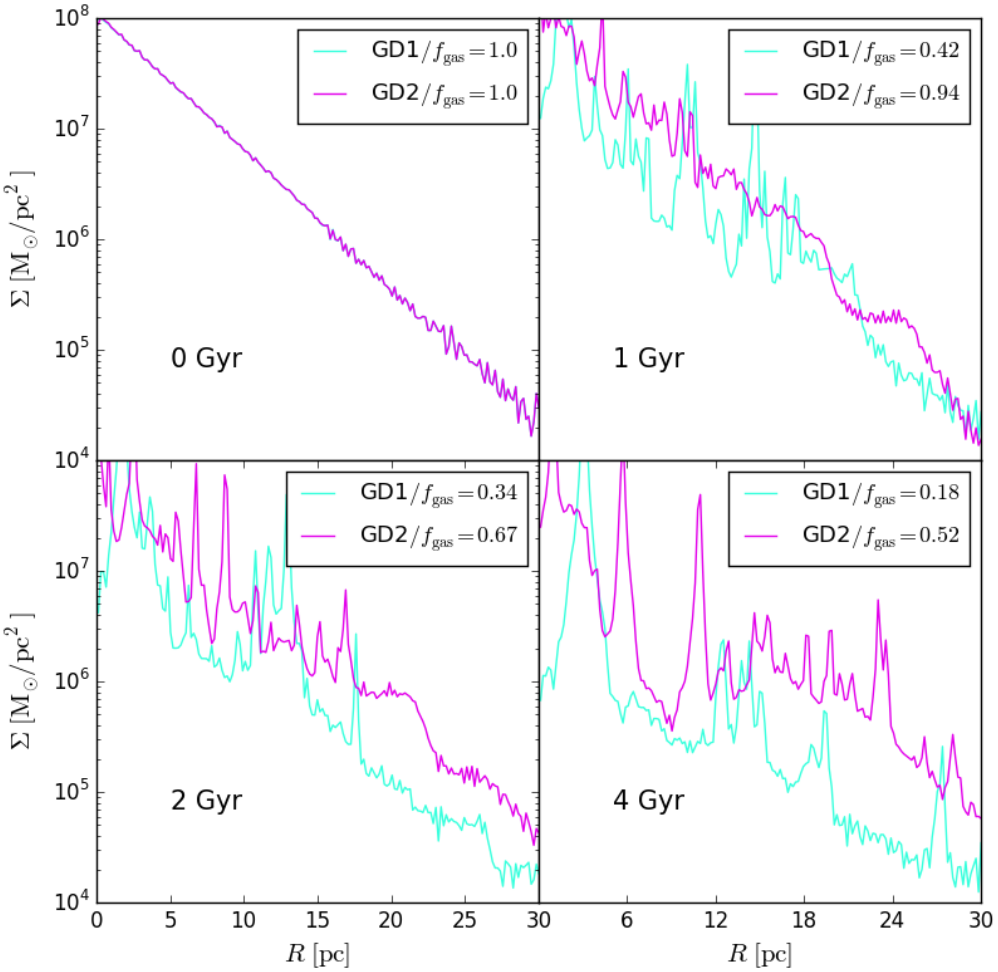

Figure 4.7: Evolution of the surface density profile for spiral galaxy simulations at times 0, 1, 2 and 4 Gyr. Cian corresponds to GD1 and magenta corresponds to GD2. The parameter f_{gas} shows the fractional mass in gas

Figures 4.7 and 4.8 show the surface density profiles, which accounts for gas and stars, at times 0, 1, 2 and 4 Gyr for spiral galaxies and 0, 10, 20 and 40 Myr for starburst galaxies. These profiles where computed by integrating along the z-axis between $z = -1$ kpc and $z = 1$ kpc for GD1 and GD2, and between $z = -25$ pc and $z = 25$ pc for SD1, SD2, SD3 and SD4, where the origin corresponds to the center of the simulation. The plots also show

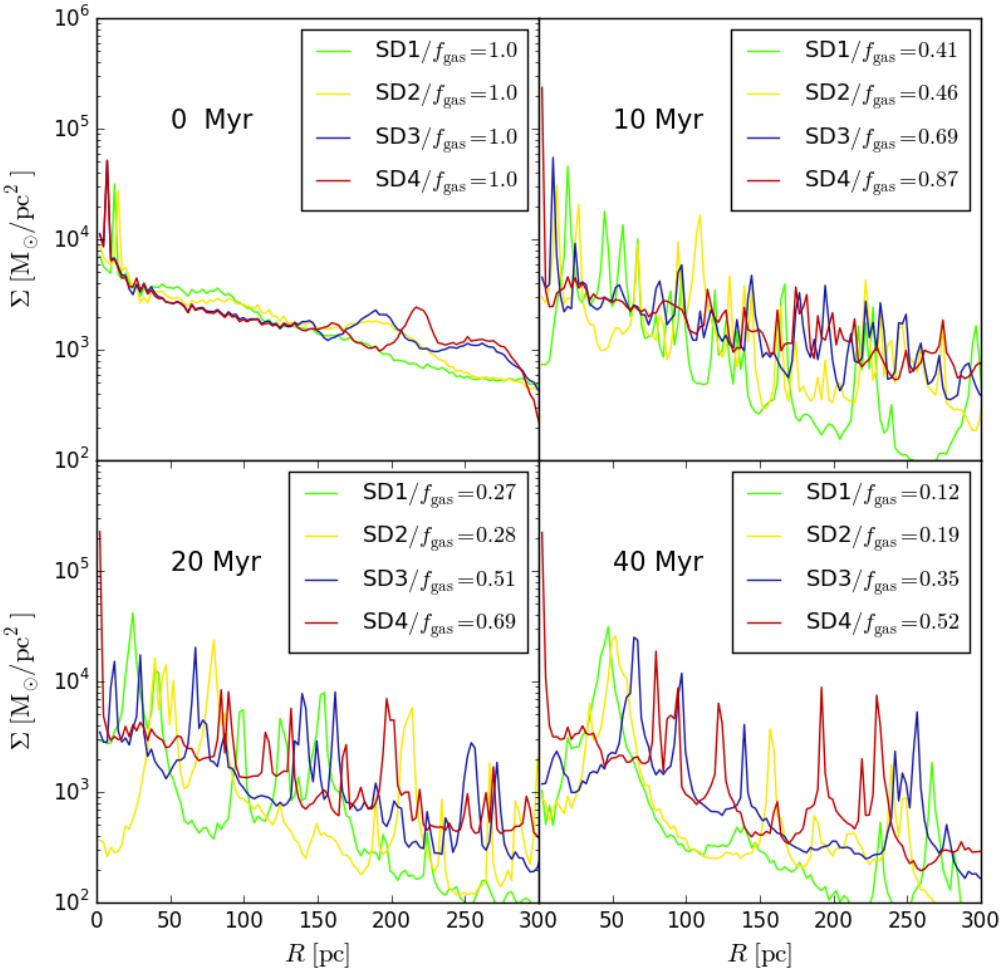

Figure 4.8: Evolution of the surface density profile for spiral galaxy simulations at times 0, 10, 20 and 40 Myr. Green, yellow, green and red colors correspond to SD1, SD2, SD3 and SD4 respectively. The parameter $f_{\rm gas}$ shows the fractional mass in gas

the fractional mass in gas at their corresponding times. As seen in figures 4.1-4.6 galaxies start to develop non-axisymmetric features and gas starts to cool and collapse which would introduce variations of the strength of the gravitational force. Each subset shows a similar profile until a critical value of $f_{\rm gas} \sim 0.4$ is reached. After this value the surface density decreases considerably and deviates from the rest of the simulations. Spiral galaxies show major differences from 2 Gyr at radii larger than 15 kpc. However, most of the stars are formed within 10 kpc.

We also show the radial profiles of the angular velocity at the same times, in Figures 4.9 and 4.10 in order to test the changes of Ω. As shown previously, for most part of the disk, Ω has similar functional forms in each set of simulations with the main difference of the amplitude as we intended. After the disks stars to fragment and the process of star formation begins Ω starts to deviate from its initial value. As in the surface density profiles, this variation shows to be related with gas consumption due to star formation. When the gas

fraction reaches values below 0.4 the disks show large variations in Ω. This complicates the definition of a characteristic value of Ω which is needed for further comparison. However, at this point most of the gas has already formed stars and the remaining gas is hotter and has a lower density, taking longer time-scales to fragment. Additionally, $f_{\rm gas}$ is calculated over a region which is larger than the volume at which star formation occurs, i.e. the actual value of $f_{\rm gas}$ in the star-forming disk is actually lower. In summary, for most of the evolution of these galaxies, taking a single characteristic value of Ω for a disk at a given time is a good approximation to test the effects of rotation.

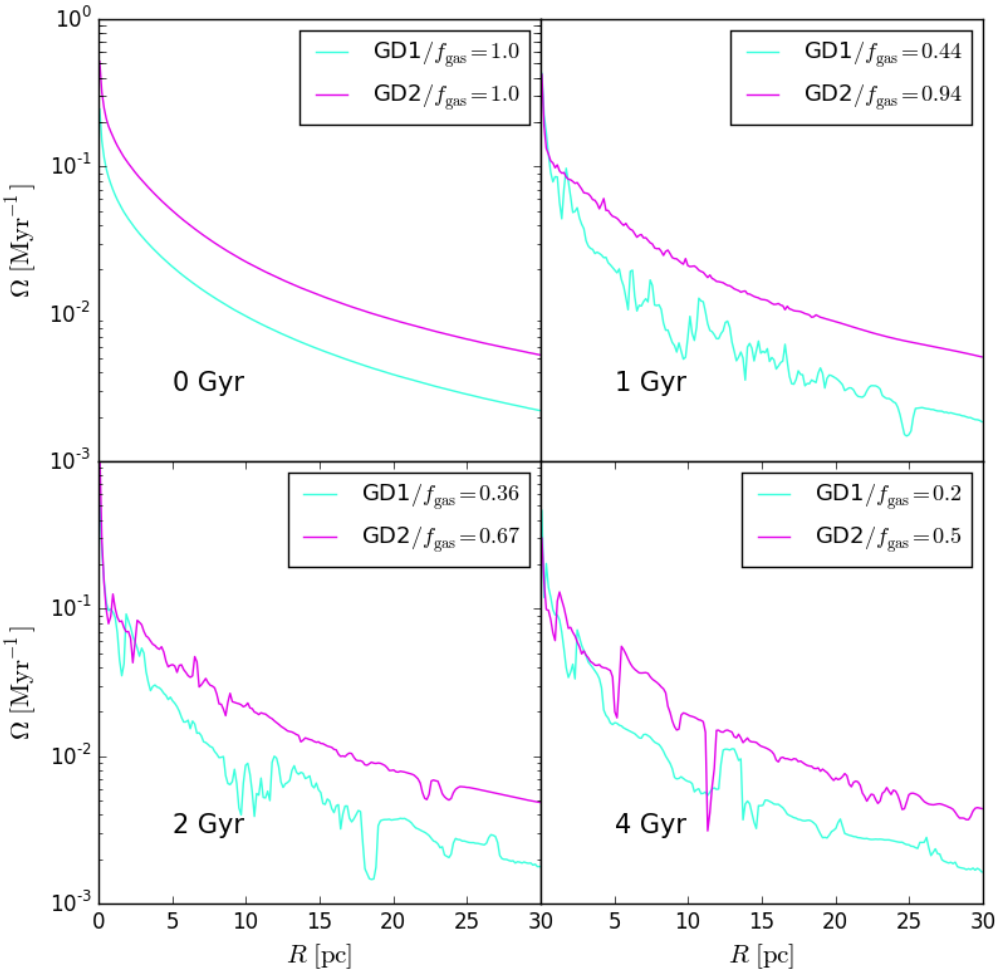

Figure 4.9: Evolution of the angular velocity density profile for spiral galaxy simulations at times 0, 1, 2 and 4 Gyr. Cian corresponds to GD1 and magenta corresponds to GD2. The parameter $f_{\rm gas}$ shows the fractional mass in gas

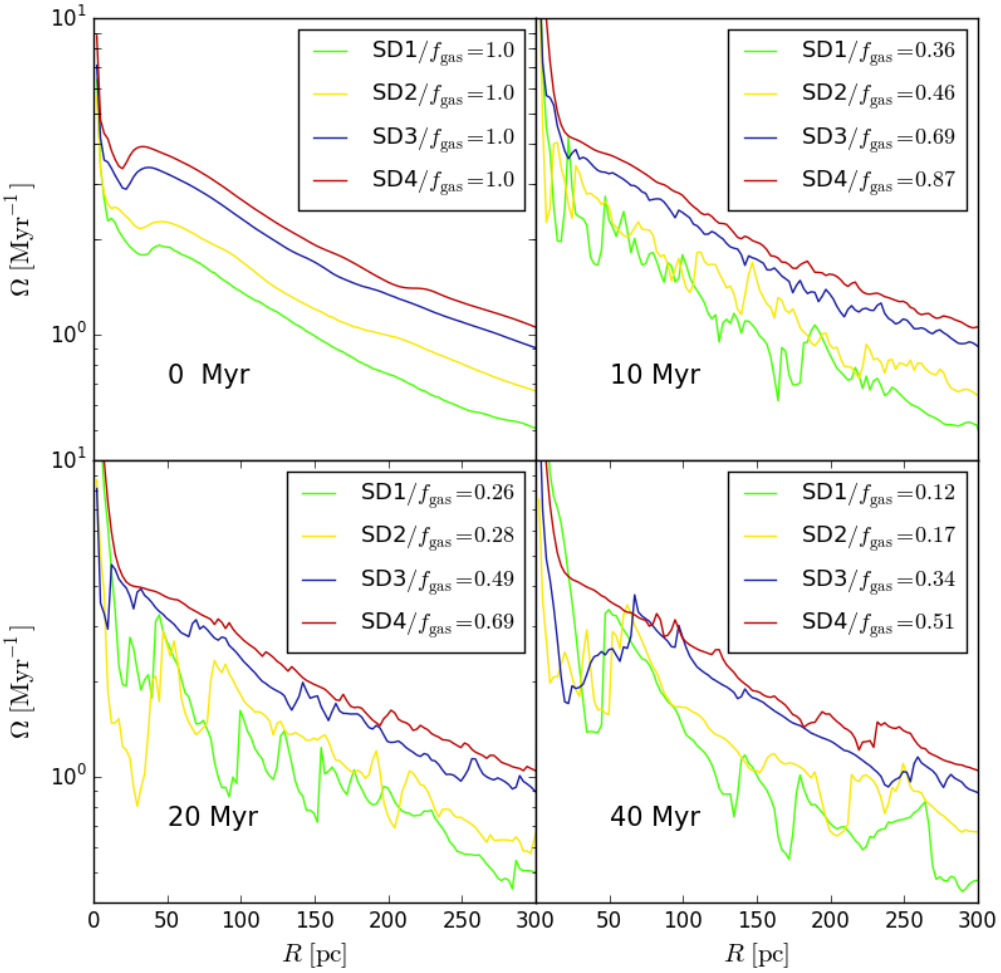

Figure 4.10: Evolution of the angular velocity profile for spiral galaxy simulations at times 0, 10, 20 and 40 Myr. Green, yellow, green and red colors correspond to SD1, SD2, SD3 and SD4 respectively. The parameter $f_{\rm gas}$ shows the fractional mass in gas

4.2 Star Formation

Now we focus on the evolution of star formation ant its empirical global laws. First, we show the evolution of star formation Figure 4.11. Here we compute the SFR as the total mass in stars $\Delta m_{\rm stars}$ formed within the time interval $[t-\Delta t, t+\Delta t]$, where Δt is 5 Myr for spiral galaxies and 50 kyr for starburst galaxies. Then, to reduce the fluctuations produced by the temporal resolution of our simulations and the Poisson's noise (since one particle created at time $t_{\rm cr}$ actually represents a population created on a time interval), we apply a Gaussian kernel smoother

$$\overline{\rm SFR}(t) = \int {\rm SFR}(t')W(t-t')dt' \quad ; \quad W(t-t') = \frac{1}{\sqrt{2\pi\sigma_t^2}} e^{-\frac{1}{2}\left(\frac{t-t'}{\sigma_t}\right)^2} \tag{4.1}$$

with $\sigma_t = 100$ Myr for the spiral galaxy simulations and 1 Myr for starburst. One of the motivations for using this method is to find the correct global maximum of star formation.

This time difference is due to the different time resolution for both sets of galaxies and their depletion times are nearly two order of magnitude different.

Both spiral and starburst galaxies show the same behaviour: stars are formed faster for simulations with lower rotation. In addition, simulations SD1 and GD1 which correspond to the galaxies with low angular velocity reach higher SFRs than the other members of their respective groups. For later times the SFR is higher for high rotating objects but this is due to the slow depletion of gas in this galaxies i.e. they still are able to form stars, which is consistent with observations (Berta et al. 2008) . We notice that the initial evolution of star formation is non-linear and leads to an exponential increment of the SFR until a maximum is reached. After this maximum the SFR shows a steady state, where it starts to decline as an exponentially function of time. As we can see from the evolution of the SFR the time to reach the exponential evolution depends strongly on the amount of rotation of the object. This shows that the connection between the amount of rotation and the speed at which instabilities grows in disks (Toomre 1964) is also connected with the process of star formation. As we shall see in the next section there is a clear connection between the star formation efficiency and the rotation of galaxies.

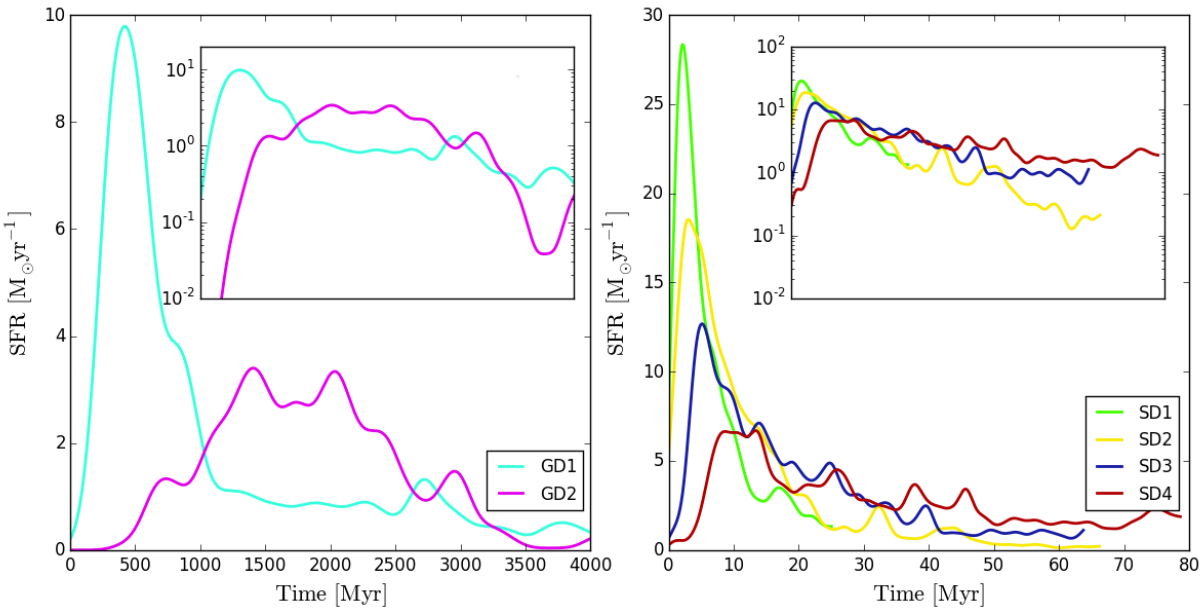

Figure 4.11: SFR vs Time. *Left*: SFR for spiral galaxies against time where the cian color corresponds to GD1 and the magenta color to GD2. GD1 reaches higher SFR rates than GD2 and at earlier times. *Right*: SFR for starburst galaxies against time where the green, yellow, blue and red colors correspond to SD1, SD2, SD3 and SD4 respectively.

4.2.1 KS and SE Laws

For now on we only analyse the evolution of star formation in the exponential decaying state. In order to only pick the steady evolution of the star formation, we locate the time t_0 at which the global maximum of the SFR is reached. To compare our results with observations

we have to calculate the star formation rate and the gas content over a projected surface, to find a law of the form $\Sigma_{\rm SFR} \propto \Sigma_{\rm gas}^{N}$, the KS law

$$\Sigma_{\rm SFR} \propto \Sigma_{\rm gas}^{N} \tag{4.2}$$

Kennicutt (1998) found empirically an index of $N \sim 1.4$ that has been proposed to be related with the reservoir of gas and the local free-fall time in the form:

$$\rho_{\rm SFR} \propto \frac{\rho_{\rm gas}}{t_{\rm ff}} \propto \frac{\rho_{\rm gas}}{(G\rho_{\rm gas})^{-\frac{1}{2}}} \propto \rho_{\rm gas}^{1.5} \tag{4.3}$$

where the free-fall time is given by $t_{\rm ff} = \sqrt{3\pi/32G\rho_{\rm gas}}$. To compute the projected quantities for the star formation laws, we need to define the integration region. We choose a cylinder which radius encircles 90% (hereafter R_{90}) of the mass in star particles created within the characteristic time of star formation $t_{\rm SFR} = M_{\rm gas}/{\rm SFR}$, where $M_{\rm gas}$ and SFR are the total quantities of gas and SFR for a simulation at a given time. In the same way, we calculate the height H_{90} that encloses 90% of the stars ($H = 2 \times z_{90}$). In order to avoid errors introduced by changes of the integration regions, we choose the center of the simulations as the center of the cylinders. At later times, when the SFR has decreased a few orders of magnitude the distribution of the newly formed stars will not be axisymmetric and some regions will change from passive to active within a few snapshots. Then by keeping the center of the region fixed we ensure that quantities, as Ω and $\Sigma_{\rm gas}$, do not change drastically from one snapshot to the next. Within the cylinders, the SFR is computed by $\Delta m_\star/\Delta t$, where $\Delta m_\star$ is the mass in stars created within Δt which are set to 100 Myr for spirals and 1 Myr for starburst disks, corresponding to roughly 10% of the average depletion time-scale at each subset of simulations. For the computation of the angular velocity parameter Ω for the SE law, we measured Ω at radius R_{90}.

Due to the resolution limit of our simulations and the numerical threshold density criterion $n_{\rm thres}$ of the star formation recipe, there is a critical surface density $\Sigma_{\rm crit}$ where for lower surface densities the time-scales at which the cells fulfil the criteria required for star formation become larger than the free-fall times and hence the SFR declines abruptly, giving rise to a steeper power law. In order to remove the data corresponding to $\Sigma_{\rm gas} < \Sigma_{\rm crit}$ from our analysis, we perform an orthogonal distance regression with a piecewise linear function defined by

$$\Sigma_{\rm SFR} = \begin{cases} \Sigma_{\rm gas}^{N} & \text{if } \Sigma_{\rm gas} < \Sigma_{\rm crit} \\ \Sigma_{\rm gas}^{1.5} & \text{if } \Sigma_{\rm gas} \geq \Sigma_{\rm crit} \end{cases} \tag{4.4}$$

on the KS logarithmic-plane ($\Sigma_{\rm gas}$, $\Sigma_{\rm SFR}$). We test this function against a unique power-law and we perform an F-test with $\alpha = 0.05$; if the null hypothesis is not rejected we consider all the data from a simulation. Figures 4.12 shows the change of star formation regime, where the data points correspond to the run GD2. Blue points have a numerical threshold density of $n = 7.5 \times 10^3 {\rm cm}^{-3}$ and a numerical efficiency of $\epsilon = 1 \times 10^{-2}$, whereas the red points have $n = 2 \times 10^3 {\rm cm}^{-3}$ and $\epsilon = 3 \times 10^{-2}$. Squares represent the regime where $\Sigma_{\rm SFR} \propto \Sigma_{\rm gas}^{1.5}$ and triangles correspond to data below the critical $\Sigma_{\rm gas}$ imposed by the resolution and numerical parameters. Vertical dashed lines indicate the critical $\Sigma_{\rm gas}$.

Figure 4.13, shows the Kennicutt-Schmidt plot for our simulations during their exponen-

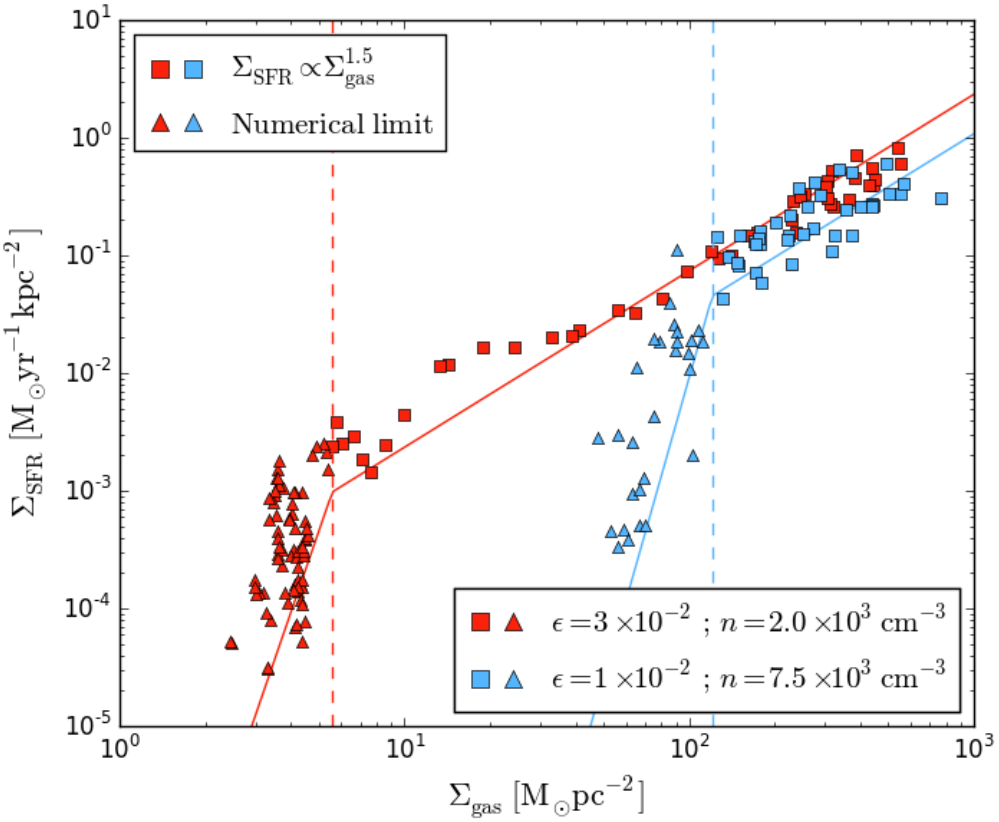

Figure 4.12: Estimation of the critical $\Sigma_{\mathbf{gas}}$

Run	Index N $\Sigma_{SFR} \propto \Sigma_{gas}^{N}$	Zero Point $\Sigma_{SFR}/\Sigma_{gas}^{1.4}$	Scatter $\Sigma_{SFR} \propto \Sigma_{gas}^{1.4}$
Face-on		dex	dex
SD1	1.996 ± 0.076	-2.283 ± 0.181	0.181
SD2	1.819 ± 0.054	-2.434 ± 0.200	0.201
SD3	1.947 ± 0.096	-2.684 ± 0.120	0.155
SD4	1.516 ± 0.088	-2.835 ± 0.156	0.147
GD1	1.807 ± 0.094	-3.448 ± 0.232	0.233
GD2	2.990 ± 0.714	-3.964 ± 0.616	0.196

Table 4.1: Kennicutt-Schmidt Law parameters: Table showing the index of the best fit in the KS plane, the zero point and scatter of the KS law with an index of 1.4. Higher rotation shows lower zero points.

tial decaying phase on star formation. Green, yellow, blue and red circles correspond to starburst while cian and magenta circles represent the spiral galaxies. For comparison with observations we have drawn the fit to the observations by Kennicutt (1998) (black solid line) and the Daddi et al. (2010) fits for normal and starburst galaxies (in gray and red dashed lines respectively). Both sets of simulations lie close to their respective observational laws. A brief description of Figure 4.13 is shown in Table 4.1. Without considering the scatter, for most simulations the individual evolution of the SFR is well described by a KS law, with an

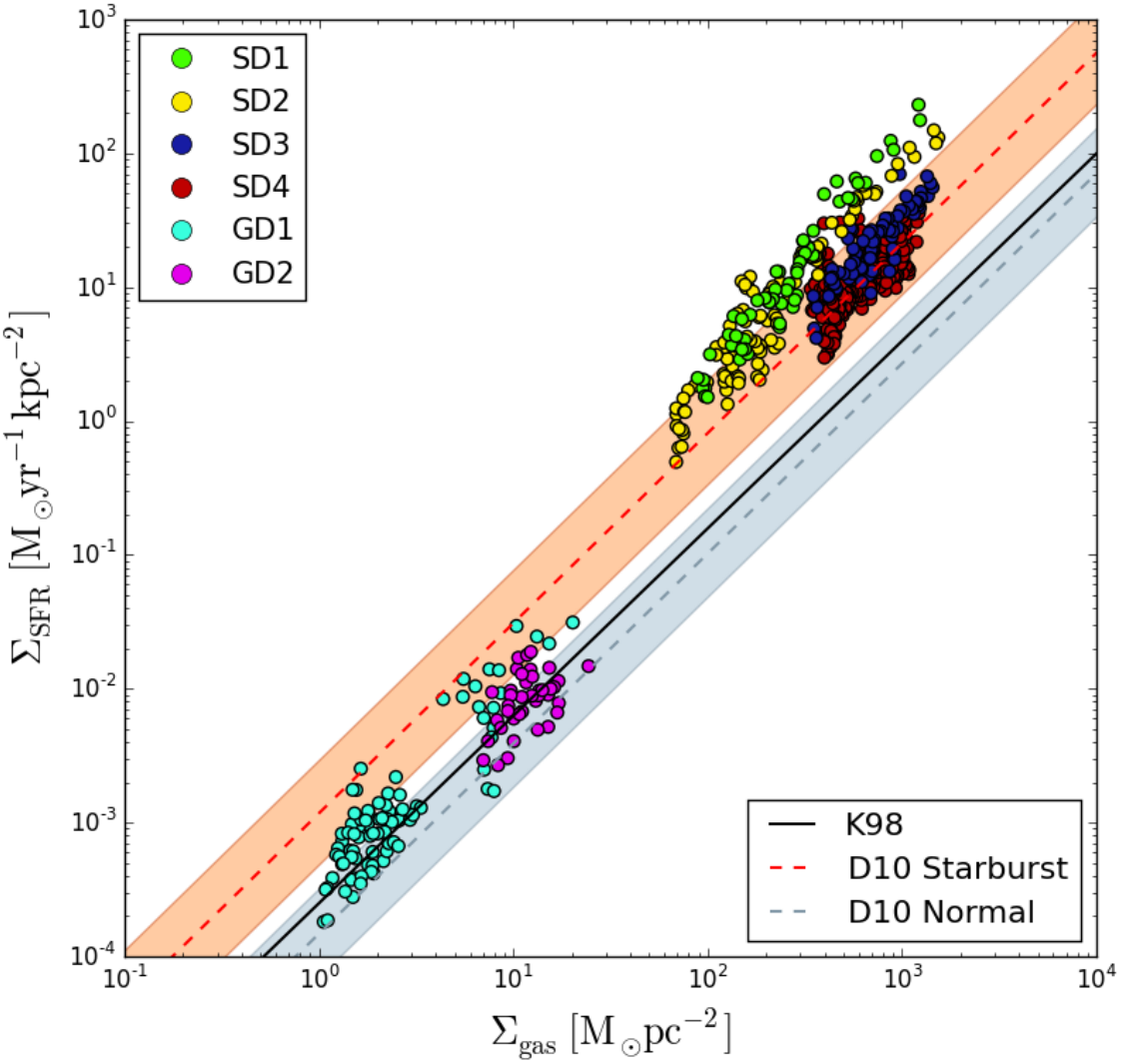

Figure 4.13: Face-on $\Sigma_{\rm SFR}$ vs $\Sigma_{\rm gas}$ for each simulation.

index N between 1.5 and 2.0. Simulation GD2 shows the larger index of the sample which might be due to the small range in $\Sigma_{\rm gas}$.

We see nearly parallel evolution curves for all the simulations in the ($\Sigma_{\rm gas}$,$\Sigma_{\rm SFR}$) plane, which is remarkable taking into account the different and complex structures showed in Figures 4.1-4.6. As found observationally by Daddi et al. (2010) we recover the bimodal behaviour in the evolution of the surface SFR in our set of simulations. Spiral disks show star formation rate consistent with normal galaxies while starbursts show higher star formation rates, more compatible with the regime of the same name.

The most striking feature shown in Figure 4.13, and also shown by the zero point in Table 4.1, is the anti-correlation between the depletion times and the amount of rotation support of the disk: disks with higher rotational velocities show lower SFR. Starburst galaxies show a clear trend between their depletion times and angular velocity. From the stability point of view this is an expected result; for high values of κ the Toomre parameter tell us that the disk will be more stable. When axisymmetric systems are perturbed the perturbations will locally rotate with the epicyclic frequency and then the value of κ can be understood as an estimation of the local rotational support. Consequently, it is desirable to analyse how rotation affects star formation.

For that we compute the most known equation that relates $\Sigma_{\rm SFR}$, $\Sigma_{\rm gas}$ and Ω which is the Silk-Elmegreen law (Silk 1997,Elmegreen 1997)

$$\Sigma_{\rm SFR} \propto \Sigma_{\rm gas}\Omega \tag{4.5}$$

tested in observations by Kennicutt (1998), taking Ω as the angular velocity at the optical radius.

Run	Index N $\Sigma_{\rm SFR} \propto (\Sigma_{\rm gas}\Omega)^{\rm N}$	Zero point $\Sigma_{\rm SFR}/\Sigma_{\rm gas}\Omega$	Scatter $\Sigma_{\rm SFR} \propto \Sigma_{\rm gas}\Omega$
Face-on		dex	dex
SD1	1.431 ± 0.065	-1.055 ± 0.214	0.216
SD2	1.460 ± 0.046	-1.320 ± 0.252	0.253
SD3	1.284 ± 0.074	-1.562 ± 0.129	0.130
SD4	0.909 ± 0.060	-1.846 ± 0.139	0.133
GD1	1.240 ± 0.080	-1.135 ± 0.271	0.273
GD2	0.800 ± 0.180	-1.529 ± 0.172	0.174

Table 4.2: Silk-Elmegreen Law parameters: Table showing the index of the best fit in the SE plane, and the zero point and scatter of the SE law with an index of 1.0. Higher rotation shows lower zero points.

Figure 4.14 shows $\Sigma_{\rm SFR}$ against $\Sigma_{\rm gas}\Omega$ for our simulations. Green, yellow, blue and red circles correspond to starburst while cian and magenta circles represent the spiral galaxies. The Kennicutt (1998) fit is represented by the black solid line and the Daddi et al. (2010) fit by the red dashed line. Table 4.2 shows the best fits of power-law functions and the scatter with respect to the SE law. The global behaviour of our simulations, i.e. considering all the data points, appears to follow the SE law. However, equation (4.5) would suggest that

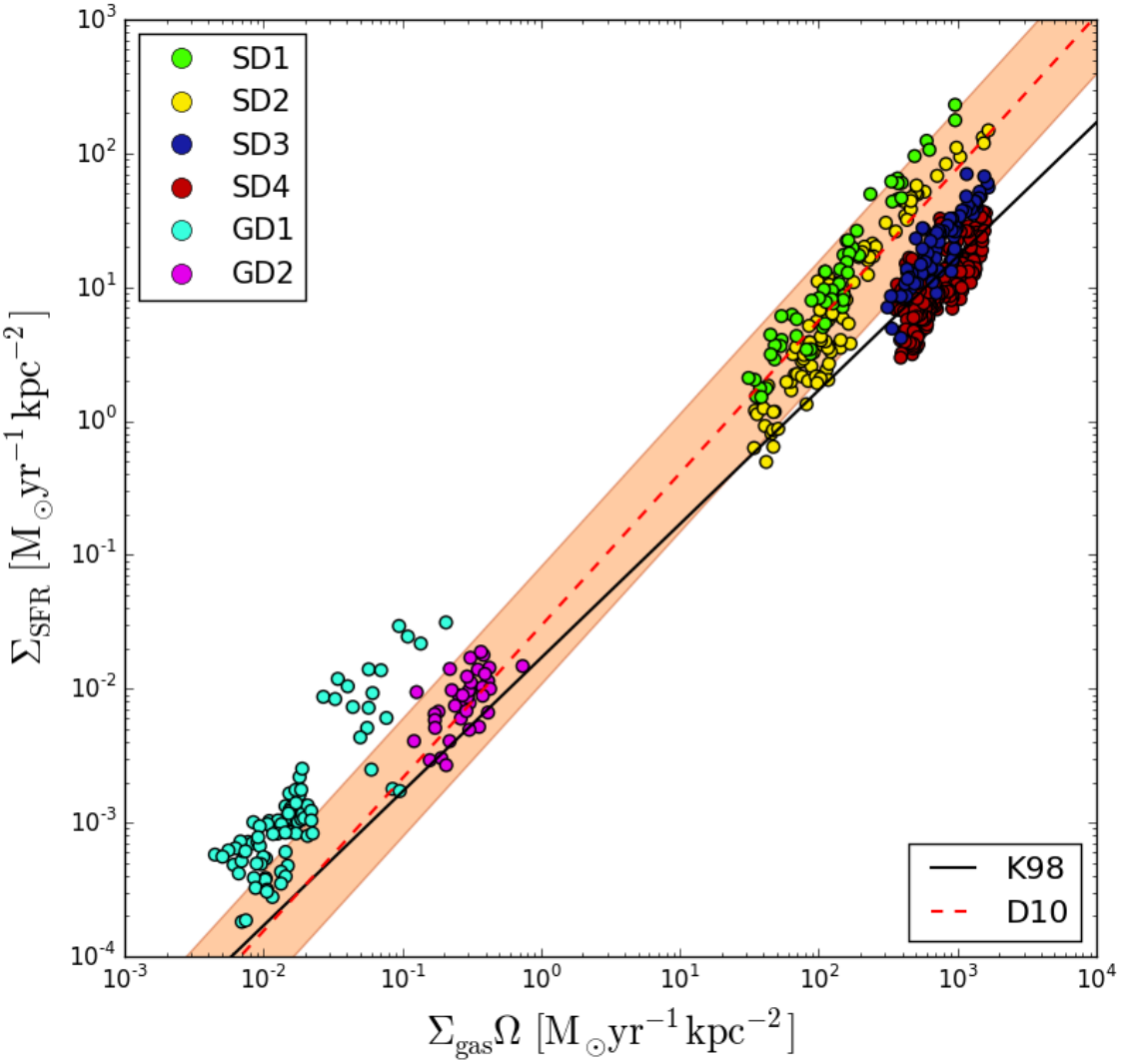

Figure 4.14: Face on $\Sigma_{\rm SFR}$ vs $\Sigma_{\rm gas}/\Omega$ for each simulation.

for a constant value of $\Sigma_{\rm gas}$ objects with higher rotational velocities would form stars more rapidly and this is not shown by Figure 4.14. Although it is evident that the star formation is a function of Ω and that each individual simulation may be described by a SE law, the behaviour among different simulations goes against the direct linear relation between star formation rate and angular velocity in disks, as suggested by the law itself. Instead, there is a consistent anti-correlation between the star formation efficiency of the SE relation and the rotational speed; towards higher rotational support the gas depletion time becomes larger. Even though the SE relation includes the rotational speed as an effective parameter, our simulations evince that the actual effect of rotation is not encapsulated in it. Then, the SE relation is still incomplete and the equation (4.5) works just as an estimation of the SFR for different types of galaxies but doesn't necessarily represent their evolution.

The major difference with figure 4.13 is that there is a unique regime for spiral and starburst galaxies, which is easily seen in Table 4.2 where the zero points of the SE law for galaxies lie within the values for starburst. This behaviour is also shown in observations (Daddi et al. 2010). The slope of each fit is slightly steeper with the exception of SD4 and GD2 which have a small sample of points and then the lower index might be produced by their scatter. One of the possible causes of this behaviour is the fact that the SE equation has the correct physical dimensions while the KS law does not. This will be discussed in section 4.2.3.

4.2.2 The integration problem

An arising problem with the KS and SE laws is the inclination of galactic disks i with respect to the line of sight, i.e. the integration axis. The physics that work in the process of star formation act in a three-dimensional space, while the KS and SE laws involves the distribution of gas in a two-dimensional space. Even further the KS law assumes that the relation between $\rho_{\rm SFR}$ and $\rho_{\rm gas}$ (quantities that involve three dimensions) is preserved after the projection. At first order

$$\rho_{\rm gas} = \frac{\Sigma_{\rm gas}}{H} \tag{4.6}$$

As mentioned before, the free-fall time is related with the volumetric gas density, $t_{\rm ff} = \sqrt{3\pi/32G\rho_{\rm gas}}$. Just by integrating along an arbitrary axis we loose information about the compactness of the object, H^{-1}, which is directly related with the strength of the gravitational potential that triggers the collapse. Then we expect to find objects with similar volumetric densities and SFR's but with projected quantities that do not lie in the same evolution curve.

For this reason we perform edge-on integrations as an experiment to test the effects of the concentration along the line-of-sight. Although in real observations edge-on galaxies are highly obscured, making difficult to measure the total SFR and gas mass, we still think is a question worth asking in order to test how fundamental are these laws. To compare with the same stars we choose the same cylinder volume as previously done but now the integration is carried along the x axis. Figure 4.15 shows the KS and SE relations for face-on and edge-on configurations.

Table 4.3 shows a brief description of Figure 4.15, displaying the parameters for the best fits of the empirical relations. The exponents of the KS law for edge-on integrations are more consistent with a 1.4 KS law than the face-on integrations. This might be a consequence

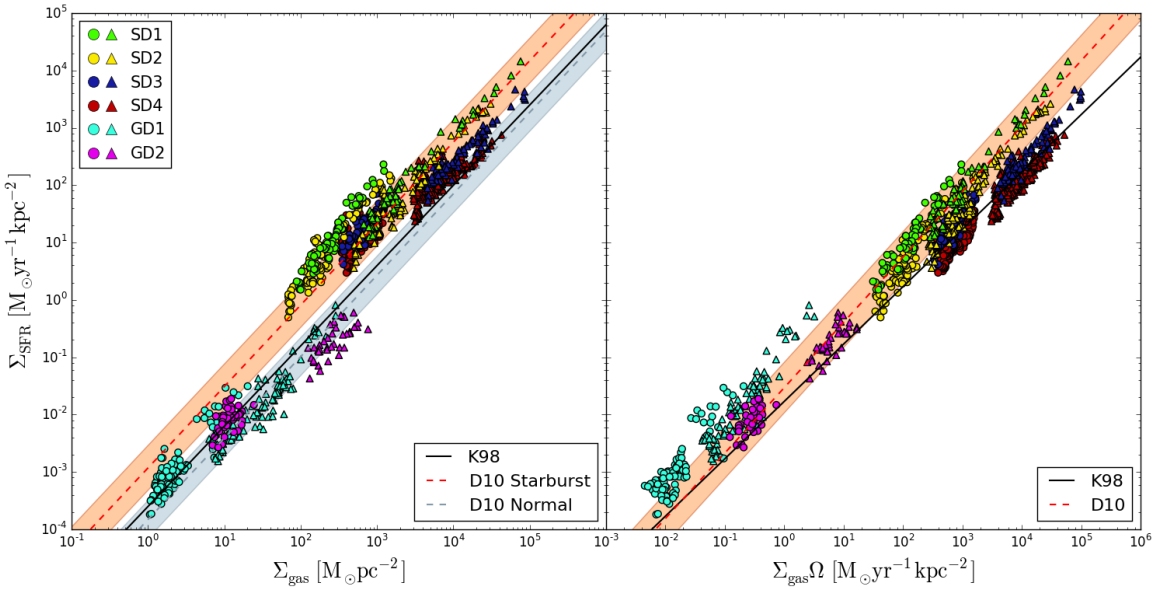

Figure 4.15: Face-on and Edge-on integrations of the KS and SE laws for each simulation. Circles and triangles correspond to projections along the z-axis and x-axis respectively. Green, yellow, blue and red colors correspond to starburst while cian and magenta colors represent the spiral galaxies. *Left*: KS relation. The black solid line corresponds the to Kennicutt (1998) fit while the dashed gray and red lines correspond to the Daddi et al. (2010) fits for normal and starburst galaxies respectively, with their corresponding scatter. Different integrations produce different depletion time-scales.*Right*: SE relation. The black line corresponds to the Kennicutt (1998) fit while the red line corresponds to the Daddi et al. (2010) fit for normal and starburst galaxies, with its corresponding scatter. Different integrations produce displacements along the law.

Run	Index N $\Sigma_{SFR} \propto \Sigma_{gas}^{N}$	Zero Point $\Sigma_{SFR}/\Sigma_{gas}^{1.4}$	Scatter $\Sigma_{SFR} \propto \Sigma_{gas}^{1.4}$
KS-Law		dex	dex
SD1	1.448 ± 0.032	-2.685 ± 0.122	0.122
SD2	1.514 ± 0.036	-2.855 ± 0.183	0.183
SD3	1.373 ± 0.044	-3.191 ± 0.138	0.160
SD4	1.160 ± 0.046	-3.263 ± 0.179	0.165
GD1	1.541 ± 0.055	-3.892 ± 0.210	0.210
GD2	1.502 ± 0.199	-4.473 ± 0.605	0.205
	$\Sigma_{SFR} \propto (\Sigma_{gas}\Omega)^{N}$	$\Sigma_{SFR}/\Sigma_{gas}\Omega$	$\Sigma_{SFR} \propto \Sigma_{gas}\Omega$
SE-law		dex	dex
SD1	1.251 ± 0.032	-1.055 ± 0.214	0.216
SD2	1.337 ± 0.031	-1.320 ± 0.252	0.253
SD3	1.143 ± 0.037	-1.562 ± 0.129	0.130
SD4	0.953 ± 0.041	-1.846 ± 0.139	0.133
GD1	1.349 ± 0.054	-1.135 ± 0.271	0.273
GD2	0.988 ± 0.137	-1.529 ± 0.172	0.174

Table 4.3: KS and SE laws parameters (Edge-on integration): *Top*: Table showing the index of the best fit in the KS plane, the zero point and the scatter of the KS law with an index of 1.4. *Bottom*: Table showing the index of the best fit in the SE plane, the zero point and scatter of the SE law with an index of 1.0.

of the different projected areas: in the edge-on configuration most of the projected area is populated by new stars whereas in the face-on case there are regions devoid of star formation. In addition, the edge-on data points cover a larger range of Σ_{gas}. Both effects minimize the errors in the determination of the slope of the power-law. In the left panel of Figure 4.15 we see that the edge-on integrations have shifted the points in the KS law toward higher values of Σ_{gas} and Σ_{SFR} but also these points have been shifted toward lower efficiencies for both types of galaxies. On the other hand in the right panel showing the SE law, the data points have been displaced along the empirical laws. The reason for this behaviour is the same in both cases: the change introduced here is the projected surface which is the same for Σ_{SFR} and Σ_{gas} then, by changing the integration axis, we are only multiplying both areas by the same number shifting each point along a vector of slope 1.0; this translates in a shift below and along the empirical laws for the KS law and the SE law respectively. An important point to take from here is that similar objects of the same age but with different inclinations respect to the line of sight lie on a line with a slope ~ 1.0 for both relations.

4.2.3 A dimensionally homogeneous law

In order to build a function able to describe a physical process, it is desirable some knowledge of the parameters involved in the process and how they would be related in an equation beforehand. The tentative functional forms of such relations can be found by using dimensional analysis tools. According to dimensional analysis any physically meaningful equation must be dimensionally homogeneous: only commensurable quantities (quantities with the same dimensions) may be compared, equated, added, or subtracted. Therefore if we want to find a law for Σ_{SFR} and its fundamental dimensions (G, Σ_{gas}, Ω, R, etc.) dimensionally homogene-

ity needs to be fulfilled. An important theorem to find such equations is the Buckingham Π theorem of dimensional analysis which was applied by Escala (2015). The star formation equation found by Escala (2015) reads:

$$\Sigma_{\rm SFR} = \epsilon \sqrt{\frac{G}{L}} \Sigma_{\rm gas}^{3/2} \tag{4.7}$$

(hereafter E15) where L represents a characteristic length scale of the system. Escala (2015) tested two characteristic scales for a disk system; the radial and vertical length scales in cylindrical coordinates showing that the later results in a unique law that represents the star formation rate for different types of galaxies. Furthermore, Escala (2015) showed that depending on the physics involved in the parameter L, such as the characteristic size of the instabilities, he is able to recover different star formation laws found in the literature, e.g. replacing L by the largest scale not stabilized by rotation derives in the SE law. In addition, the star formation efficiency ϵ is likely to be related with the dynamics inside molecular clouds through dimensionless quantities, which has been found and tested in simulations (Padoan et al. 2012,Semenov et al. 2015).

As in the KS and SE laws, we compute the E15 relation integrating over the z and x axes. For each integration we choose L as the gas mass-weighted dispersion $L = \sqrt{\langle s^2 \rangle - \langle s \rangle^2}$, where s is the position along the line of sight and $\langle f \rangle$ is defined by

$$\langle f \rangle = \frac{\int_V \rho(\vec{x}) f dx^3}{\int_V \rho(\vec{x}) dx^3} \tag{4.8}$$

The volume of integration V corresponds to the cylinder defined by R_{90} and z_{90}.

Figure 4.16 shows the E15 equation for the whole set of simulations. A description of Figure 4.16 is shown in Table 4.4. The slopes displayed in Table 4.4 show that the evolution of the SFR is well depicted by the E15 relation. In addition, the slopes are more consistent compared to the KS plot, agreeing with a dimensionally homogeneous equation. Although the functional form of the E15 relation is similar to the KS relation there is a major difference: the E15 relation suppresses the bi-modal behaviour shown by the KS law and demonstrates that the global behaviour of the SFR is well represented by a single regime. This shows that the gas distribution along the line of sight should be considered if we want to compare objects with different three-dimensional geometries. Most remarkably, this relation shows that for both lines of sight the evolution of each galaxy follows a unique curve, and hence a unique observed efficiency, suggesting that this homogeneous relation is taking into account the concentration along the line of sight in the correct form. One interpretation is that with the inclusion of the extra parameter L we are actually fitting a law of the form $\rho_{\rm SFR} \propto \frac{\rho_{\rm gas}}{t_{\rm ff}} \propto \sqrt{G} \rho_{\rm gas}^{1.5}$ which we can express in terms of the integrated densities along different axes like x and z:

$$\frac{\Sigma_{{\rm SFR},i}}{L_i} \propto \sqrt{G} \left(\frac{\Sigma_{{\rm gas},i}}{L_i} \right)^{1.5} \tag{4.9}$$

where i is the integration axis. Then if the length scale L is chosen properly, the observed exponent and star formation efficiency have the same values for any observer.

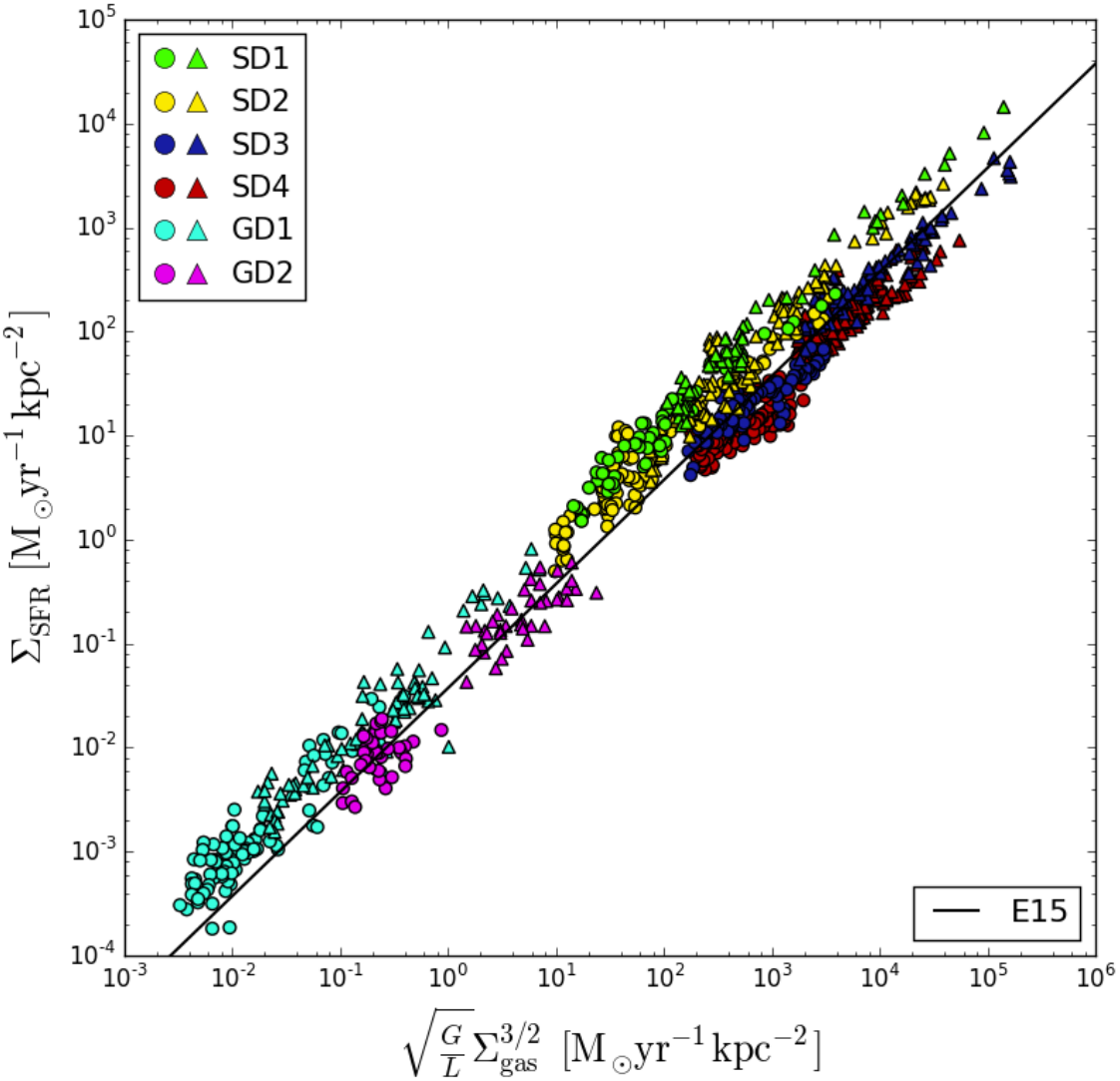

Figure 4.16: E15 relation: Circles and triangles correspond to projections along the z-axis and x-axis respectively. Green, yellow, blue and red colors correspond to starburst while cian and magenta colors represent the spiral galaxies. The black solid line shows the observational best fit for the E15 relation. Different integrations result in displacement along this relation.

Run	Index N	Zero point	Scatter
	$\Sigma_{\rm SFR} \propto \left(\sqrt{\frac{G}{L}}\Sigma_{\rm gas}^{3/2}\right)^{\rm N}$	$\Sigma_{\rm SFR}/\sqrt{\frac{G}{L}}\Sigma_{\rm gas}^{3/2}$	$\Sigma_{\rm SFR} \propto \sqrt{\frac{G}{L}}\Sigma_{\rm gas}^{3/2}$
Face-on		dex	dex
SD1	0.898 ± 0.032	-0.909 ± 0.143	0.143
SD2	0.976 ± 0.029	-1.053 ± 0.182	0.182
SD3	0.699 ± 0.039	-1.499 ± 0.193	0.178
SD4	0.692 ± 0.038	-1.538 ± 0.190	0.204
GD1	1.069 ± 0.047	-1.056 ± 0.202	0.202
GD2	1.227 ± 0.244	-1.436 ± 0.210	0.210
Edge-on			
SD1	0.950 ± 0.021	-0.852 ± 0.129	0.129
SD2	0.999 ± 0.024	-1.012 ± 0.183	0.183
SD3	0.826 ± 0.026	-1.397 ± 0.178	0.159
SD4	0.812 ± 0.028	-1.488 ± 0.172	0.185
GD1	0.974 ± 0.038	-1.067 ± 0.233	0.233
GD2	0.836 ± 0.101	-1.466 ± 0.247	0.206

Table 4.4: E15 relation parameters (Both integrations): Table showing the index of the best fit in the E15 plane, the zero point and scatter of the E15 relation. Different integrations show similar zero points.

However, as seen in the previous section, Figure 4.16 also shows that simulations with different rotational velocities lie on parallel distinctive curves, manifesting that this formulation does not incorporate the net effect of galactic rotation in the star formation process. Knowing that the E15 relation incorporates the effects of concentration, we proceed to study the efficiency of star formation an its dependence with Ω.

As mentioned in 4.2.2 the inclination of the plane of simulated galaxies produces a vector displacement, in the KS and SE plots, which has a linear slope. Figure 4.17 shows the displacement for data points of SD2 in the KS, SE and E15 plots. From this figure we see clearly that a KS law with a ~ 1.5 index is a good model for the evolution of the SFR for a single object but its efficiency depends on the observer; on the contrary the $\Sigma\Omega$ law does not represent individual evolution but its efficiency is independent on the observer. For the latter we emphasize that this behaviour is only due to that a change in the projected area is also linear. Then is clear that similar objects whose concentration is unknown will show slopes lower than 1.5 in the KS relation. On the other hand, for the E15 relation this displacement occurs parallel to the law despite not being linear. The requirement of homogeneity leads us directly to a law that is both, a good model for the individual evolution of the SFR and an equation independent of the observer. The orders of magnitude for this shift, considering inclinations from $i = 0°$ to $i = 90°$, are proportional to R/H where R is the radius of the object and H the scale height. For starburst disks R/H varies from 10 to 100 while for spirals this value is always ~ 10.

4.2.4 Efficiency

The first evidence of a connection between rotation and star formation efficiency was shown in Figure 4.11.First, the time needed to reach an equilibrium state of star formation (exponential

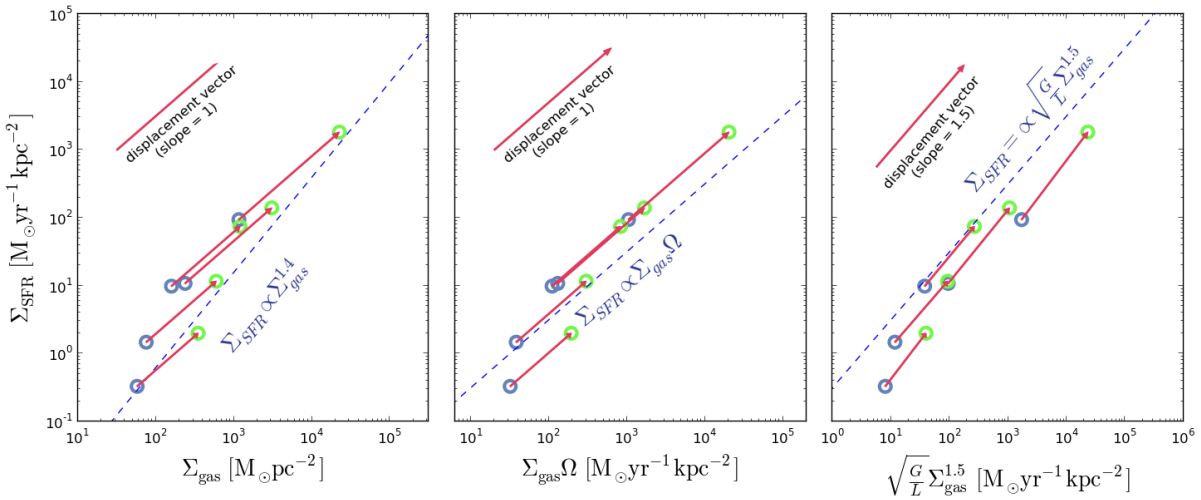

Figure 4.17: Effects of the line-of-sight : Data points corresponding to the simulation SD2. Green and blue circles correspond to integrations along the x and z axis respectively. *Left*: Displacements in the KS plot. The blue dashed line has a slope of 1.4. *Middle*: Displacements in the SE plot. The blue dashed line has a slope of 1. *Right*: Displacements in the E15 plot. The blue dashed line has a slope of 1.

decay) is anti-correlated with galactic rotation. This stage of evolution corresponds to the fragmentation and growth of the first over-densities formed in the disks. For a thin-razor disk, the growth rate of the instabilities is given by

$$\gamma = \kappa\sqrt{\frac{1}{Q} - 1} \tag{4.10}$$

where Q is the Toomre parameter (Toomre 1964). The second evidence comes from the star formation laws shown in Figures 4.15 and 4.16.
In order to construct a more robust star formation law that includes the observed effect of rotation in our simulations, we compare the efficiency of the E15 relation

$$\epsilon = \frac{\Sigma_{\rm SFR}}{\sqrt{\frac{G}{L}}\Sigma_{\rm gas}^{3/2}} \tag{4.11}$$

with the characteristic angular velocity of the galactic disks. In this case, we choose the representative value of Ω in a disk as the one associated with the total angular momentum of the gas defined by J_z/I_z, where J_z and Iz are the z-components of the angular momentum and the moment of inertia respectively. By doing this we reduce the variations in Ω produced by changes in R_{90}.

Figure 4.18 shows the star formation efficiencies of the E15 relation for face-on (circles) and edge-on (triangles) integrations against Ω. Starburst and spiral galaxies lie on different ranges of Ω then displaying different efficiencies as function of Ω. The functional form of the efficiency can be approximated by two separated exponentially decreasing, one for spirals and another for starbursts galaxies. In mathematical terms, the star formation relation is approximately

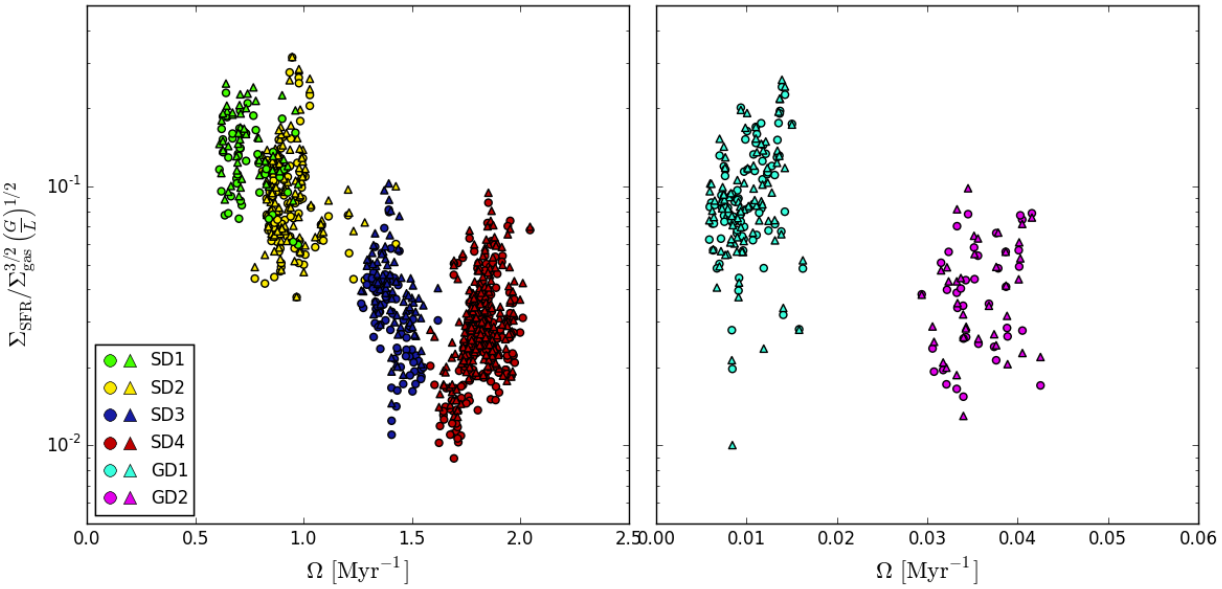

Figure 4.18: Efficiency vs Ω: Efficiency of the E15 relation against the characteristic value of Ω. Circles and triangles correspond to projections along the z-axis and x-axis respectively. *Left*: Starburst galaxies where green, yellow, blue and red colors correspond to SD1, SD2, SD3 and SD4 respectively. *Right*: Spiral galaxies where cian and magenta colors correspond to GD1 and GD2.

given by $\Sigma_{\rm SFR} = \exp(-B\Omega)\sqrt{G/L}\Sigma_{\rm gas}^{3/2}$, where the value of the time-like constant B depends, in principle, on whether this is a spiral or starburst disk. The requirement of dimensional homogeneity demands an efficiency that is only function of dimensionless quantities. This implies the existence of another time-scale $t^* \sim B$ that should normalize this function, i.e. represent the efficiency for any kind of object. For a body that lacks rotational support, the free-fall time-scale controls the rate of gravitational collapse, thus $t_{\rm ff}$ is a natural candidate of this second time-scale. Since the current density of the collapsing structures is directly affected by the rotational support, i.e. at later time the density distribution depends on Ω, the simplest approach is to take the initial free-fall time of the simulation, as done in previous works (Padoan et al. 2012), as a proxy for this characteristic time-scale related to a system with no rotation. To remove the effects of initial conditions we measure the free-fall time after one vertical collapse. For this we the following: First we define the average free-fall time as $\bar{t}_{\rm ff} = (G\bar{\rho})^{1/2}$, here $\bar{\rho}$ is the volume-weighted average of the density field. While the disk starts to cool down, the disk will experiment vertical collapse with a characteristic time $\bar{t}_{\rm ff,0}$, where $\bar{t}_{\rm ff,0}$ is the average free-fall time. For times $t > \bar{t}_{\rm ff,0}$ the vertical density distribution is less affected by the initial conditions. For this reason we measure $\bar{t}_{\rm ff}$ at a time $t = \bar{t}_{\rm ff,0}$, where the disk height reaches a steady value. We refer to this time-scale as $t_{\rm ff}^{\rm ini}$.

We plot the efficiency against $\Omega t_{\rm ff}^{\rm ini}$ for all the simulations, which is shown in the left panel of Figure 4.19. The time-scale $t_{\rm ff}^{\rm ini}$ shows to do a great work normalizing the effects of rotation. Now spiral galaxies and starburst disks lie in the same two-dimensional parameter space. This allow us to find a unique function relating the star formation efficiency and the dimensionless

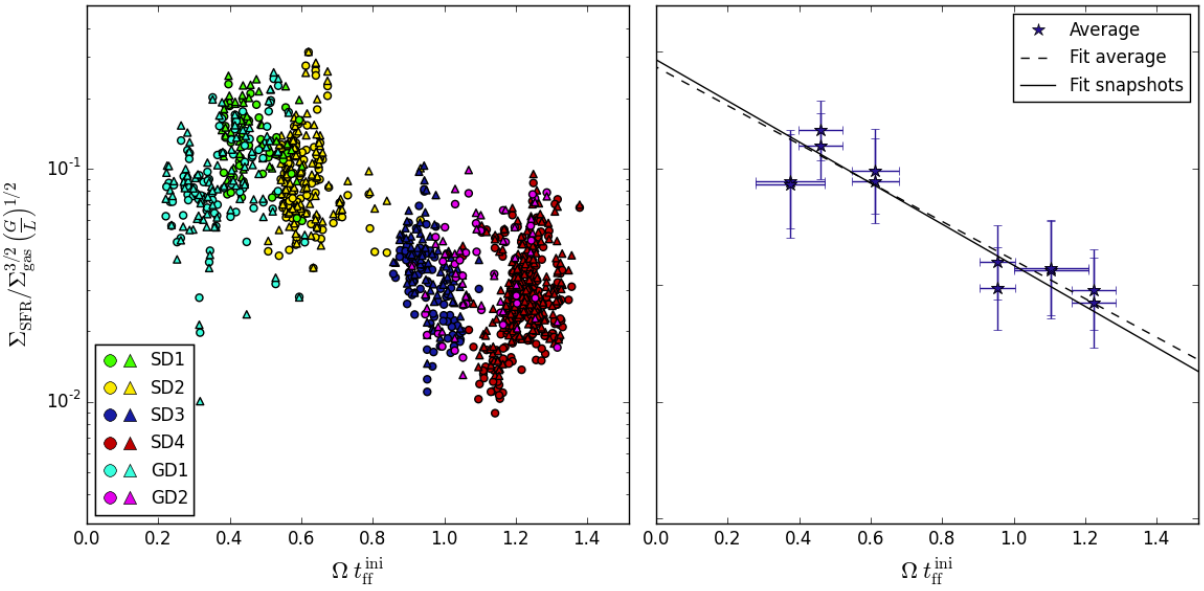

Figure 4.19: Efficiency vs $\Omega t_{\rm ff}^{\rm ini}$: *Left*: Circles and triangles correspond to projections along the z-axis and x-axis respectively. Green, yellow, blue and red colors correspond to SD1, SD2, SD3 and SD4 respectively while cian and magenta colors correspond to GD1 and GD2. *Right*: stars corresponds to the mean values for every run and inclination. The dashed line corresponds to the fit to the mean values, which is approximately $0.27\exp(-1.91\Omega t_{\rm ff}^{\rm ini})$. The solid line corresponds to the fit to all the points in the left panel, given by $0.29\exp(-2.03\Omega t_{\rm ff}^{\rm ini})$

Star formation Law	KS	Bimodal KS	SE	HR	This work
Scatter [dex]	0.490	0.360	0.362	0.316	0.206

Table 4.5: Scatter of star formation laws : Table showing the scatter in the star formation rate for the different laws analysed in this work and our formulation.

quantity $\Omega t_{\rm ff}^{\rm ini}$. The efficiency appears to be represented by an exponential profile as found by Padoan et al. (2012) with $\epsilon \propto \exp(-\beta t_{\rm ff}/t_{\rm dyn})$ where $t_{\rm ff} \propto (G\rho)^{-1/2}$. Motivated by this previous work we fit an exponential curve to the data an find the functions:

$$\epsilon = 0.27^{0.05}_{0.04} e^{(-1.91\pm0.22)\Omega t_{\rm ff}^{\rm ini}} \tag{4.12a}$$

$$\epsilon = 0.29^{0.01}_{0.01} e^{(-2.03\pm0.05)\Omega t_{\rm ff}^{\rm ini}} \tag{4.12b}$$

shown in the right panel of Figure 4.19. Equation 4.12a is the best fit to the blue stars which corresponds to the average ϵ and $\Omega t_{\rm ff}^{\rm ini}$ per run per line-pf-sight. Equation 4.12b is the best fit to all the points in the left panel of Figure 4.19. To compute these fits we performed an orthogonal distance regression in orden to consider uncertainties in both parameters. These fits are shown in the right panel of Figure 4.19. With these expressions now we are able to formulate a star formation law. We choose equation 4.12a since it does not consider the different sampling among different runs. We show in Figure 4.20 that the global behaviour

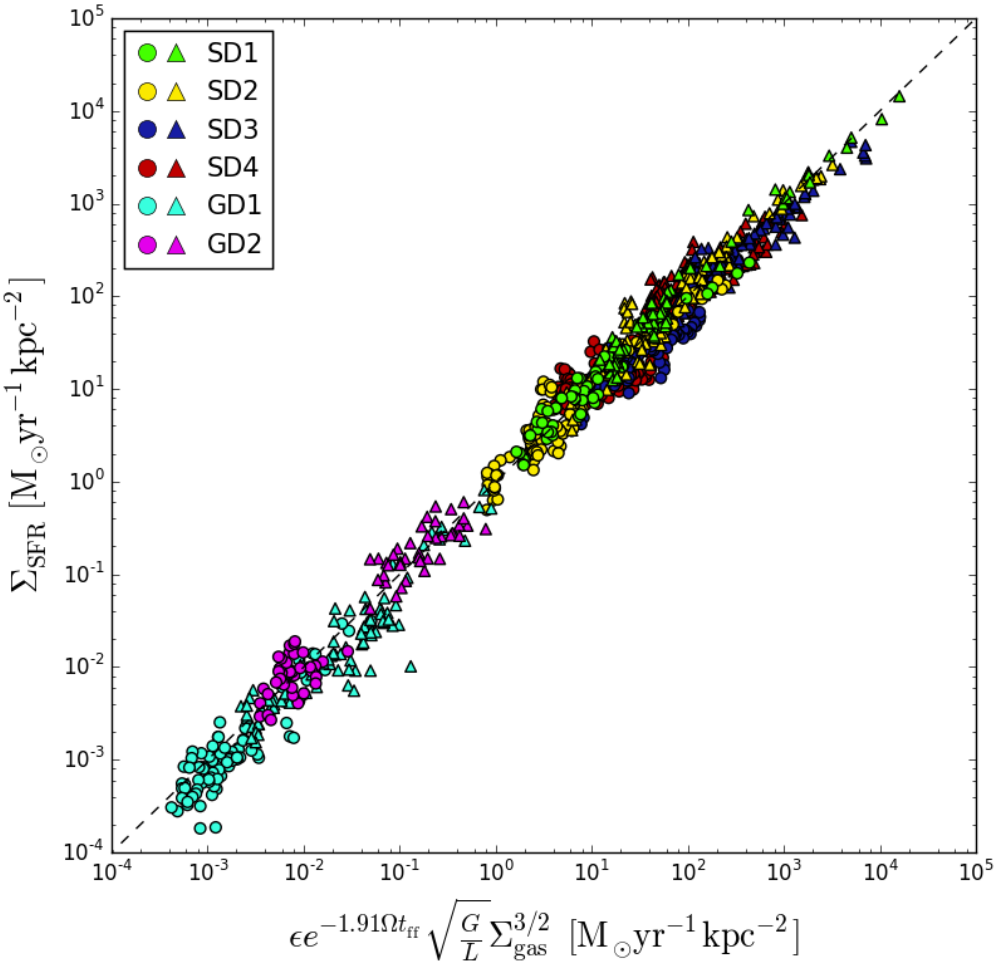

Figure 4.20: $\Sigma_{\rm SFR}$ as a function of $0.27\exp(-1.91\Omega t_{\rm ff}^{\rm ini})$: Circles and triangles correspond to projections along the z-axis and x-axis respectively. Green, yellow, blue and red colors correspond to SD1, SD2, SD3 and SD4 respectively while cian and magenta colors correspond to GD1 and GD2. The black dashed line represents the equality.

of the star formation in our simulations can be represented by a unique law given by

$$\Sigma_{\rm SFR} = 0.27 e^{-1.91\Omega t_{\rm ff}^{\rm ini}} \sqrt{\frac{G}{L}} \Sigma_{\rm gas}^{3/2} \tag{4.13}$$

which is independent of galaxy type, line of sight and incorporates the effect of galactic rotation. For comparison of the different star formation laws analysed in this work, we shown in Table 4.2.4 the vertical scatter of the laws in question. Our proposed star formation relation reduces the scatter of the classical KS law by 58% and that of the bi-modal KS law by 42%.

The proposed star formation law in Equation 5.1 arises to the same functional form discussed in Escala (2015) where the efficiency is efficiency given by $\epsilon \propto \exp(-1.6 t_{\rm ff}/t_{\rm dyn})$ as proposed by Padoan et al. (2012) where the dynamical time $t_{\rm dyn}$ corresponded to the turbulent crossing time $t_{\rm cr}$. This efficiency has already been tested and has shown good results

(Semenov et al. 2015). In the simulations presented here $t_{\rm cr}$ is replaced by the inverse of Ω ($\propto t_{\rm orb}$). This change is expected since we are modelling global dynamics of rotating disks, where Ω^{-1} arises as a natural time-scale. In simulations of isolated boxes subject to supersonic turbulent forcing (Padoan et al. 2012), which are modelling individual giant molecular clouds, $t_{\rm cr}$ is the only possible choice for $t_{\rm dyn}$. In other words, we have linked global disk dynamics to the local dynamics of giant molecular clouds. Moreover, the constant factors 1.61 and 1.91 are of the same order despite coming from completely different numerical experiments.

4.2.5 Normalizing time-scale

Due to the uncertainties about the physical nature of the normalizing time-scale, the election of the time-scale that normalizes the effects of rotation 4.19 is somewhat arbitrary. For that reason we explore other possible choices for this normalizing time-scale, which have been measured within the cylinder defined by R_{90} and z_{90}. These additional normalizing time-scales studied are shown in Figure 4.21. In the left panel we compare the mass-weighted averages of Ω and free-fall time $t_{\rm ff}^{\rm mid}$ at the mid-plane for different radii in the same disk, where $t_{\rm ff}$ is defined by $(G\rho_{s,g})^{-1/2}$ and the mid-plane is defined by the cell which have the maximum density along the z-axis. To compute this time-scale we consider the contribution of both gas and stars for the matter density $\rho_{s,g}$, resulting in the function:

$$\epsilon = 0.18^{0.01}_{0.01} e^{(-1.22\pm0.03)\Omega t_{\rm ff}^{\rm mid}} \tag{4.14}$$

Although it seems to do a good work normalizing the effects of rotation, there are still some theoretical issues with this physical parameter which question its nature. First, this time-scale represents the collapse of a spherical region of constant density which does not correspond to this case. Second, although stars contribute to the stability of a gaseous disk (Rafikov 2001), they do not collapse with the gas, which is assumed to derive $t_{\rm ff} \propto (G\rho_{s,g})^{-1/2}$.

A second time-scale can be found by considering our numerical limitations. In order to form a star, a given gas cell must be collapsing due to self-gravity. We approach this problem by invoking the 3-dimensional Jeans instability, where any perturbation greater than the Jeans length $\lambda_J = c_s\sqrt{\frac{\pi}{G\rho}}$ will be gravitationally unstable and will trigger collapse. In the case of our simulations there is a critical length that corresponds to the resolution of the simulation Δx. Then by imposing $\Delta x = \lambda_J$ we find a second time-scale $(G\rho)^{-1/2} = \Delta x/\sqrt{\pi}c_s$. It should be mentioned that for a fixed c_s this time-scale is an effective time delay imposed by our numerical recipes which depend on Δx. The effects of this time-scale are shown in the right panel of Figure 4.21 and the best fit is given by:

$$\epsilon = 0.23^{0.01}_{0.01} e^{(-2.43\pm0.05)\Omega\Delta x/\sqrt{\pi}c_s} \tag{4.15}$$

Although it is a natural time-scale of the simulations, its numerical nature and the non-sphericity of our systems put this time as a normalizing time-scale into doubt, requiring additional more simulations of identical objects to depict its effects.

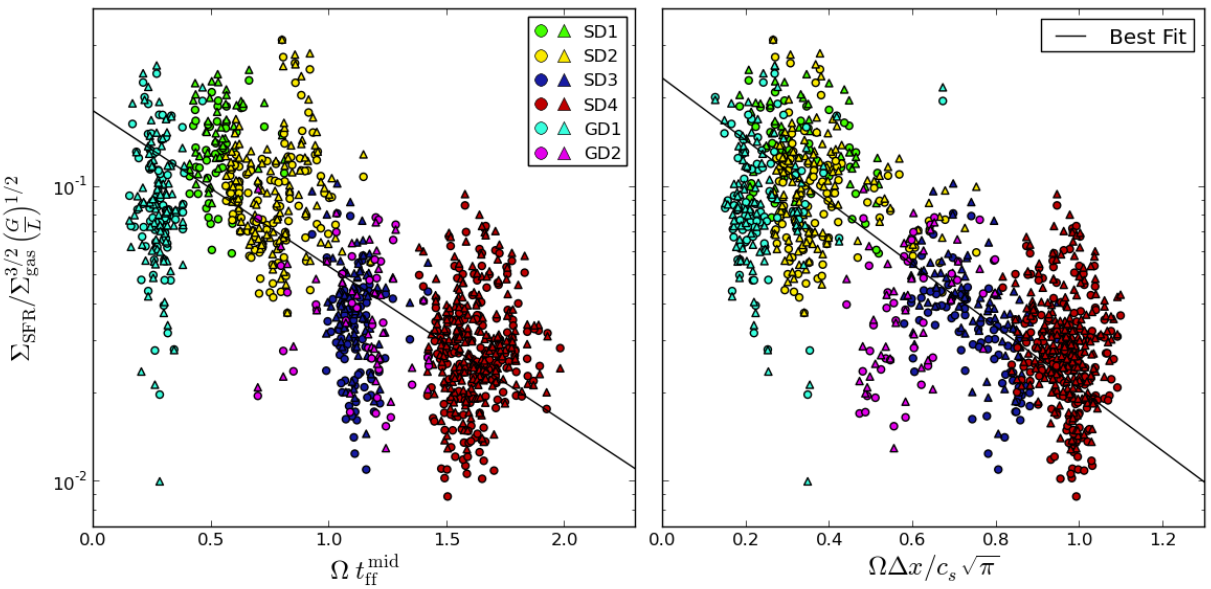

Figure 4.21: Alternative normalizing time-scales: *Left*: Plot showing the efficiency of the E15 equation as a function of $\Omega t_{\rm ff}^{\rm mid}$ where $t_{\rm ff}^{\rm mid}$ is the mass-weighted average of the free-fall time at the midplane. Triangles and circles correspond to integrations along the x and z axis respectively. The solid line represent the best fit with a slope of -1.22. *Right*: Plot showing the efficiency of the E15 equation as a function of $\Omega\Delta x/c_s\sqrt{\pi}$ where Δx is the size of the smallest cell and c_s is the mass-weighted average of the sound speed. The solid line represent the best fit with a slope of -2.43.

Chapter 5

Conclusions and Outlook

Using simulations of spiral galaxies and the nuclear disks of starburst galaxies, we study the galactic laws for star formation found in the literature and the role of galactic rotation. The simulations were performed using the adaptive mesh refinement code Enzo, employing the ZEUS hydro-code to solve the Euler equations for the gas fluid. We apply radiative cooling via cooling curves down to T =300K. Gas cells are allowed to form stars if a few criteria are fulfilled, which later inject energy to their surrounding medium through stellar feedback. The simulations are evolved in co-moving coordinates in a ΛCDM universe using isolated boundary conditions. The criteria used for refinement consists on baryon mass resolution and refinement by Jeans length, ensuring that it is at least resolved by 4 cells to prevent artificial fragmentation. The spiral galaxies are simulated in a box of $666h^{-1}$ kpc with a maximum a resolution of $\sim$ 40pc. Starburst are simulated in a box of 4 kpc with a maximum a resolution of $\sim$ 2pc.

The initial conditions for each galaxy are chosen in order to maximize the effects of rotation in the process of star formation with respect to other parameters, such as the free-fall time and the mass distribution.

Spirals. Spiral galaxies consist of two rotationally supported gaseous disks, with an exponential radial profile of length scale 35 kpc and a sech^2 profile for the vertical direction with a length scale of 0.4 kpc. The disks are embedded in a potential generated by stars and dark matter. Stars are modelled by a Miyamoto-Nagai profile with radial and vertical length scales of 35 kpc and 0.2 kpc. Dark matter is decribed by an Navarro-Frenk-White profile. The total mass of the external potentials is $(M_{\mathrm{star}}, M_{\mathrm{DM}}) \in \{(10^{10}\mathrm{M}_\odot, 10^{10}\mathrm{M}_\odot), (10^{11}\mathrm{M}_\odot, 10^{11}\mathrm{M}_\odot)\}$.

Starburst. We simulate four rotationally supported nuclear disks of starburst galaxies, with an R^{-1} profile with 300 pc of extension and a sech^2 profile for the vertical direction where the length scale is a function of radius for vertical equilibrium. The disks are embedded in an isothermal sphere with a dispersion velocity of σ =100, 130, 190 and 220 km/s with a core radius (King radius) of 100 pc.

The whole set of simulations show to be well described by a Kennicutt-Schmidt law with a 1.4 index which is consistent with observations and exhibits two regimes of star formation as found empirically by Daddi, where the starburst galaxies lie in the starburst-like objects and the spiral galaxies lie in the normal star formation regime. The simulations show an overall

agreement with Silk-Elmegreen law. However, the Silk-Elmegreen relation does not represent the major effect of rotation on the simulations, which is the anti-correlation with efficiency. This shows that the Silk.Elmegreen relation works only as a rough statistical estimate of the SFR among different types of galaxies. By introducing the effects of the inclination respect to the line of sight we find that each point is shifted by a vector with a slope ~ 1 in the Kennicutt-Schmidt and Silk-Elmegreen relations, that translates into different efficiencies in the former and similar efficiencies in the latter. We test the dimensionally homogeneous equation $\Sigma_{\rm SFR} = \epsilon\sqrt{G/L}\Sigma_{\rm gas}^{3/2}$, proposed by Escala (2015), where L is the characteristic length scale along the line of sight. The evolution of each simulation shows to be in agreement with this equation and we found that the efficiency under this prescription shows to be inclination-invariant, which means that a single object will always lie on the same star-formation curve independently of the observer. This star formation law shows a smaller scatter compared with the Kennicutt-Schmidt and Silk-Elmegreen laws but its efficiency still anti-correlates with the angular velocity of the disk.

The time at which the star formation rate reaches an equilibrium state in our simulations occurs at later times for high values of angular speed. Studying each galaxy during the steady phase, we find that the remaining scatter of the E15 relation is parametrized by galactic rotation. Concretely the star formation efficiency is exponentially diminished by increasing Ω. By requiring the efficiency to be a function of dimensionless parameters, we found that the star formation efficiency is well represented by an exponential decreasing function of the quantity $\Omega t_{\rm ff}^{\rm ini}$ where Ω is the characteristic angular velocity and $t_{\rm ff}^{\rm ini}$ is the initial free-fall time, leading to a unique galactic star formation law:

$$\Sigma_{\rm SFR} = 0.27 e^{-1.91\Omega t_{\rm ff}^{\rm ini}} \sqrt{\frac{G}{L}} \Sigma_{\rm gas}^{3/2} \tag{5.1}$$

Notably, the functional form of the efficiency has already been found in simulations of molecular clouds Padoan et al. (2012), where the dimensionless parameter corresponded to $t_{\rm ff}^{\rm ini}/t_{\rm cr}$, where $t_{\rm cr}$ is the turbulent crossing time. Our findings suggest that rotationally supported galaxies, embedded in potential with different strengths should display slightly different star formation efficiencies. However, it is necessary to study the effects of rotation in simulations at sub-galactic scales in order to easily compare the results with simulations. The star formation law found in this work can be used in cosmological simulations subject to resolution limits. However, since the angular velocity is measured from an origin, the implementation of this law is not straightforward and its validity in extreme environments, such as mergers, still has to be tested. From these preliminary results we can design different sets of simulations to characterize the effects of physical parameters not tested in this work, or if simulations with a constant $\Omega t_{\rm ff}^{\rm ini}$ show similar efficiencies.

Bibliography

Agertz, O. Fundamental differences between SPH and grid methods. *Mon. Not. R. Astron. Soc.* **380**, 963-978 (2007)

Berger, M. J., Colella, P., May 1989. Local adaptive mesh refinement for shock hydrodynamics. *J. Comput. Phys.* **82**, 64-84 (1989)

Berta, Z. K., Jimenez, R., Heavens, A. F. & Panter, B. The role of spin in the formation and evolution of galaxies. *Mon. Not. R. Astron. Soc.* **391**, 197-204 (2008)

Bigiel, F. et al. The star formation law in nearby galaxies on sub-kpc scales. *Astron. J.* **136**, 2846-2871 (2008)

Binney, J. & Tremaine, S. *Galactic Dynamics* Princeton University Press, ed. 2, (2008)

Bolatto, A. D., Wolfire, M. & Leroy, A. K. The CO-to-H_2 Conversion Factor. *Annu. Rev. Astron. Astrophys.* **51**, 207-268 (2013)

Bryan, G. L. *et al.* A piecewise parabolic method for cosmological hydrodynamics. *Comput. Phys. Commun.* **89**, 149-168 (1995)

Bryan, G. L. *et al.* ENZO: An adaptive mesh refinement code for astrophysics. *Astrophys. J.* **211**, 19 (2014)

Cen, R. & Ostriker, J. P. Galaxy formation and physical bias. *Astrophys. J.* **399**, 113–116 (1992)

Ceverino, D. & Klypin, A. The role of stellar feedback in the formation of galaxies. *Astrophys. J.* **695**, 292-309 (2009).

Creasey, P., Theuns, T., Bower, R. G. & Lacey, C.G. Numerical overcooling in shocks *Mon. Not. R. Astron. Soc.* **415**, 3706-3720 (2011)

Colella, P. & Woodward, P. R. The Piecewise Parabolic Method (PPM) for Gas-Dynamical Simulations. *J. Comput. Phys.* **54**, 174–201 (1984)

Daddi, E. et al. Different star formation laws for disks versus starbursts at low and high 5redshifts. *Astrophys. J.* **714**, 118-122 (2010)

Davis, T. A. *et al.* The ATLAS^{3D} project - XXVIII. Dynamically driven star formation suppression in early-type galaxies. *Mon. Not. R. Astron. Soc.* **444**, 3427-3445 (2014).

Dobbs, C. L., Pringle, J. E. & Duarte-Cabral, A. The frequency and nature of "cloud-cloud collisions" in galaxies. *Mon. Not. R. Astron. Soc.* **446**, 3608-3620 (2015).

Downes, D. & Solomon, P. M. Rotating nuclear rings and extreme starbursts in ultraluminous galaxies. *Astrophys. J.* **507**, 615-654 (1998)

Elmegreen, B. G. Theory of starbursts in nuclear rings. *Rev. Mex. Astron. Astrofis.* **27**, 165-171 (1997)

Escala, A. On the functional form of the universal star-formation law. *Astrophys. J.* **804**, 54 (2015).

Gingold, R. A. & Monaghan, J. J. Smoothed particle hydrodynamics - Theory and application to non-spherical stars. *Mon. Not. R. Astron. Soc.* **181**, 375–389 (1977)

Hockney, R. W. & Eastwood J. W. *Computer simulation using particles*, CRC Press (1988)

James, R. A. The Solution of Poisson's Equation for Isolated Source Distributions. *J. Comput. Phys.* **25**, 71-93 (1977)

Kennicutt, R. C., Jr. The global schmidt law in star-forming galaxies. *Astrophys. J.* **498**, 541-552 (1998)

Kim, J., Wise, J. H., Alvarez, M. A. & Abel, T. Galaxy Formation with Self-consistently modeled stars and massive black holes. I. Feedback-regulated star formation and black hole growth. *Astrophys. J.* **738**, 54 (2011)

Krumholz, M. R., Dekel, A. & McKee, C. F. A universal, local star formation law in galactic clouds, nearby galaxies, high-redshift disks, and starbursts. *Astropys. J.* **745**, 69 (2012)

Kuzmin, G. G. *Astron. Zh.* **33** 27 (1956)

Lada, C. J., Lombardi, M. & Alves, J. F. On the star formation rates in molecular clouds. *Astrophys. J.* **724**, 687-693 (2010).

Leroy, A. K. et al. The star formation efficiency in nearby galaxies: Measuring where gas forms stars effectively. *Astron. J.* **136**, 2782-2845 (2008)

Lucy, L. B., A numerical approach to the testing of the fission hypothesis. *Astron. J.* **82**, 1013–1024 (1977)

Madore, B. F. Numerical simulations of the rate of star formation in external galaxies. *Mon. Not. R. Astron. Soc.* **178**, 1-9 (1977).

Martin, C. L. & Kennicutt, R. C., Jr. Star formation thresholds in galactic disks. *Astrophys.* J. **555**, 301-321 (2001)

McKee, C. F. & Ostriker, E. C. Theory of star formation. *Annu. Rev. Astron. Astrophys.* **45**, 565-687 (2007)

Miyamoto, M. & Nagai, R. Three-dimensional models for the distribution of mass in galaxies. *Publ. Astron. Soc. Jpn.* **27**, 533–543 (1975)

Narayanan, D. Star formation in high-redshift starburst galaxies. *ArXiv e-prints*, (2013).

Navarro, J. F., Frenk, C.S. & White, S. D. M. A universal density profile from hierarchical clustering. *Astrophys. J.* **490**, 493 (1997).

Obreschkow, D. *et al.* Low angular momentum in clumpy, turbulent disk galaxies. *Astrophys. J.* **815**, 97 (2015).

Padoan, P. et al. The star formation rate of molecular clouds. *Protostars and Planets VI* 77-100 (2014)

Padoan, P., Haugbolle, T. & Nordlund, A. A simple law of star formation. *Astrophys. J.* **759**, 27 (2012)

Plummer, H. C. On the problem of distribution in globular star clusters. *Mon. Not. R. Astron. Soc.* **71**, 460–470 (1911)

Rafikov, R. R. The local axisymmetric instability criterion in a thin, rotating, multicomponent disc. *Mon. Not. R. Astron. Soc.* **323**, 445-452 (2001).

Rosen, A. & Bregman J. N., Global models of the interstellar medium in disk galaxies. *Astrophys. J.* **440**, 634 (1995).

Roychowdhury, S., Huang, M. L., Kauffmann, G., Wang, J. & Chengalur, J. N. The spatially resolved Kennicutt-Schmidt relation in the H I-dominated regions of spiral and dwarf irregular galaxies. *Mon. Not. R. Astron. Soc.* **449**, 3700-3709 (2015)

Sarazin, C. L. & White, R. E. III. Steady state cooling flow models for normal elliptical galaxies. *Astrophys. J.* **320**, 32-48 (1987).

Schmidt, M. The rate of star formation. *Astrophys. J.* **129**, 243-258 (1959)

Seigar, M. S. The connection between shear and star formation in spiral galaxies. *Mon. Not. R. Astron. Soc.* **361**, 20–24 (2005)

Semenov, V., Kravtsov, A. & Gnedin, N. Non-universal star formation efficiency in turbulent ISM. *ArXiv e-prints*, (2015).

Silk, J. Feedback, Disk self-regulation, and galaxy formation. *Astrophys. J.* **481**, 703-709 (1997)

Stone, J. M. & Norman, M. L. ZEUS-2D: A radiation magnetohydrodynamics code for astrophysical flows in two space dimensions. I - The hydrodynamic algorithms and tests. *Astrophys. J.* **80**, 753-790 (1992).

Szűcs1, L., Glover, S. & Klessen, R. How well does CO emission measure the H_2 mass of MCs. *Mon. Not. R. Astron. Soc.* (2016)

Tan, J. C. Star formation rates in disk galaxies and circumnuclear starbursts from cloud collisions. *Astrophys. J.* **536**, 173–184 (2000)

Tasker, E. J. & Tan, J. C. Star formation in disk galaxies. I. Formation and evolution of giant molecular clouds via gravitational instability and cloud collisions. *Astrophys. J.* **700**, 358-375 (2009).

Toomre, A. On the gravitational stability of a disk of stars. *Astrophys. J.* **139**, 1217-1238 (1964)

Truelove, J. K. *et al.* The Jeans condition: A new constraint on spatial resolution in simulations of isothermal self-gravitational hydrodynamics. *Astrophys. J.* **489**, 179 (1997).

Truelove, J. K. *et al.* Self-gravitational hydrodynamics with three-dimensional adaptive mesh refinement: Methodology and applications to molecular cloud collapse and fragmentation. *Astrophys. J.* **495**, 821-852 (1998).

van Leer, B. Towards the ultimate conservative difference scheme. IV. A new approach to numerical convection. *J. Comput. Phys.* **23**, 276 (1977)

Wang, P. & Abel, T. Magnetohydrodynamic simulations of disk galaxy formation: The magnetization of the cold and warm medium. *Astrophys. J.* **696**, 96-109 (2009)

Wang, P., Abel, T. & Zhang, W. Relativistic hydrodynamic flows using spatial and temporal adaptive structured mesh refinement. *Astrophys. J. Suppl. Ser.* **176** 467-483 (2008)